GIANT RESONANCES IN ^{44}CA, ^{54}FE, ^{64}ZN, ^{68}ZN, AND ^{94}MO

A Dissertation

by

JONATHAN THOMAS BUTTON

Submitted to the Office of Graduate and Professional Studies of
Texas A&M University
in partial fulfillment of the requirements for the degree of

DOCTOR OF PHILOSOPHY

Chair of Committee,	Dave H. Youngblood
Committee Members,	Sherry J. Yennello
	Shalom Shlomo
	Che Ming Ko
Head of Department,	George Welch

May 2016

Major Subject: Physics

ABSTRACT

The centroids of the Giant Monopole Resonance (GMR) exhibit significant scattering about an expected $A^{-1/3}$ mass dependence. Also, the GMR strength distribution had been observed to transition in shape from symmetric (Gaussian-like) in heavier nuclei to asymmetric over the $40<A<90$ region. The origin of this is not clear and may be the result of nuclear structure or some other effect. This suggested a study of the GMR in ^{44}Ca, ^{54}Fe, ^{64}Zn, and ^{68}Zn. In the A~90 region for Zr and Mo, a second unexplained peak can be seen in the strength distribution for the GMR. Analysis of the GMR in ^{94}Mo may help to explain this characteristic.

Isoscalar giant resonances in ^{44}Ca, ^{54}Fe, ^{64}Zn, ^{68}Zn, and ^{94}Mo have been studied with inelastic scattering of 240 MeV α particles at small angles including 0°. In ^{44}Ca, a majority of the Energy Weighted Sum Rule (EWSR) was identified for E0 and E2 (≈70%), and nearly half was identified for E1. Between 70 and 105% of the expected isoscalar E0 strength has been identified below E_x = 40 MeV for ^{54}Fe, ^{64}Zn, and ^{68}Zn. Between 70 and 104% of the E1 strength has been identified while 60% of E2 strength in ^{54}Fe and ^{68}Zn and 120% of the strength in ^{64}Zn has been identified. For ^{94}Mo all of the expected EWSR for the isoscalar E0 resonance was found (104%). A significant portion of the EWSR was found for the isoscalar E1 (75%), E2 (61%), and the high energy octupole E3 (46%) resonances.

DEDICATION

This is dedicated to my wife Elisabeth, son Luke, my parents Marc and Lita, my brother Scott, and to all my family and friends.

ACKNOWLEDGEMENTS

This work would not be possible without the guidance of Dr. Dave Youngblood and Dr. Yiu-Wing Liu. Special thanks to Dr. Krischichayan, Robert Polis, and the Faculty and Staff of the Texas A&M Cyclotron Institute.

TABLE OF CONTENTS

Page

ABSTRACT ii

DEDICATION iii

ACKNOWLEDGEMENTS iv

TABLE OF CONTENTS v

LIST OF FIGURES viii

LIST OF TABLES xiv

1 INTRODUCTION 1

1.1 Giant Resonances 1
1.2 Incompressibility of Nuclear Matter 2
1.3 Nuclei to Study 5
1.3.1 A=40-48 6
1.3.2 ^{54}Fe, ^{64}Zn, and ^{68}Zn 8
1.3.3 ^{94}Mo 10
1.4 Dissertation Outline 13

2 EXPERIMENTAL PROCEDURE 15

2.1 Overview 15
2.2 MDM Spectrometer 18
2.3 Focal Plane Detector 18
2.3.1 Gas Ionization Chamber 19
2.3.2 Resistive Wire Proportional Counters 21
2.3.3 Plastic Scintillator 22
2.4 Experiment Details 22
2.5 Electronics and Data Acquisition 23
2.6 Detector Calibration 26
2.6.1 Position Calibration 26
2.6.2 Angle Calibration 27
2.6.3 Energy Calibration 29
2.6.4 Data Processing 29

3 DATA ANALYSIS 31

3.1 Overview 31

3.2 Transition Densities....33
3.3 Transition Potentials....35
3.4 Effective Interaction....38
3.5 Fit to Experimental Data....40

4 ISOSCALAR E0, E1, AND E2 STRENGTH IN ^{44}CA....44

4.1 Overview....44
4.2 Introduction....44
4.3 Experimental Procedure....46
4.4 Multipole Analysis....47
4.5 Description of Microscopic Calculations....50
4.6 Discussion....52
4.6.1 E0 Strength....55
4.6.2 E1 Strength....58
4.6.3 E2 Strength....59
4.7 Summary....59

5 ISOSCALAR GIANT RESONANCES IN ^{54}FE, ^{64}ZN, AND ^{68}ZN....61

5.1 Overview....61
5.2 Introduction....61
5.3 Experimental Procedure....66
5.4 Multipole Analysis....69
5.5 Description of Microscopic Calculations....73
5.6 Discussion....75
5.6.1 E0 Strength....83
5.6.2 E1 Strength....87
5.6.3 E2 Strength....89
5.7 Summary....90

6 ISOSCALAR E0, E1, E2, AND E3 STRENGTH IN ^{94}MO....92

6.1 Overview....92
6.2 Introduction....92
6.3 Experimental Procedure....94
6.4 Multipole Analysis....96
6.5 Description of Microscopic Calculations....99
6.6 Discussion....101
6.6.1 E0 Strength....104
6.6.2 E1 Strength....106
6.6.3 E2 Strength....109
6.6.4 E3 Strength....110
6.7 Summary....111

7 CONCLUSIONS 112

REFERENCES 115

LIST OF FIGURES

Page

Figure 1. Centroid energies (m_1/m_0) for the ISGMR are plotted as a function of A. Lines representing $36/A^{1/6}$ and $40/A^{1/5}$ are shown for reference. 5

Figure 2. Centroid energies (E_{CEN}) for ^{40}Ca and ^{48}Ca and the energy difference (ΔE_{CEN}) obtained with HF-RPA calculations are plotted for different Skyrme interactions having different values of K_{NM}. (a) and (b) compare the calculated and experimental values for the centroid energy in ^{40}Ca and ^{48}Ca, respectively. The dashed lines represent the experimental value and its error. (c) and (d) compare the calculated with the experimental difference in centroid energy. In (d), the RPA calculations are done without the Coulomb and spin-orbit interactions. From Ref. [28]. 7

Figure 3. Centroid energies (m_1/m_0) for the ISGMR are plotted as a function of A. Lines representing $36/A^{1/6}$ and $40/A^{1/5}$ show the approximate systematic trend. The nuclei shown are ^{40,48}Ca [28]; ^{46,48}Ti [31]; ^{56}Fe and ^{58,60}Ni [26]. The values from this work for ^{54}Fe and ^{68}Zn are included as well. 10

Figure 4. The black histograms show the fraction of the r^2Y_{00} sum rule obtained for Mo and Zr isotopes plotted as a function of excitation energy. Superimposed are Guassian fits to the two components of the distributions as well as the sum of the fits. From Ref. [27]. 11

Figure 5. The scaling model K_A values obtained from measured scaling energies $(m_3/m_1)^{1/2}$ are shown for Zr and Mo isotopes by squares and triangles respectively and plotted versus A. The lines indicate the HF-based RPA values of K_A calculated within HF-RPA using the KDE0v1 interaction for Zr (green dashed line) and Mo (black solid line) isotopes. From Ref. [17].....13

Figure 6. Diagram of the beam line for the MDM experiments is illustrated. The α particle beam begins at the ECR ion sources, is injected into the K500 Cyclotron for acceleration to 240 MeV, is passed through the Beam Analysis System, and then is transported to the MDM Spectrometer. 16

Figure 7. Diagram of the Experiment Layout is illustrated. The α particle beam bombards the target in the target chamber, goes through a 4°x4° slit in the slit box (not pictured, between target chamber and multipole magnet) and the MDM spectrometer, and is analyzed in the Focal Plane Detector.....17

Figure 8. A cross-section view of the focal plane detector is shown. The beam enters the front window from the left and loses energy to the isobutane gas. Electrons from the beam path are measured by the position sensitive wires (W1-W4), and energy loss by the beam particle in the gas is measured by the 3 ΔE plates. The beam goes through the exit window on the right side and is stopped in the plastic scintillator. 19

Figure 9. Schematic drawing of the Gas System is shown. Gas flow through the system is indicated by the lines with arrows. Valves are indicated by circles with diagonal arrows. Gas is mixed with alcohol from the refrigerator in the Gas Mixer before flowing through the ionization chamber (detector). The constant gas flow is maintained by 2 MKS controllers. Gas is pumped from the detector by the Roughing Pump. 20

Figure 10. Schematic of the electronic components used for processing signals from the Focal Plane Detector is shown. 26

Figure 11. The five narrow opening slit used at the entrance of the spectrometer for position and angle calibration is illustrated.....27

Figure 12. A ray (light blue solid line) in the detector is illustrated. The horizontal positions of the ray are measured from wire 1 and wire 4 in order to calculate the angle of the ray in the detector. 28

Figure 13. The Giant Resonance peak is "sliced" into 300 keV bins for identifying strength of the multipole excitations by comparison with PTOLEMY DWBA calculation of the multipole cross-sections. 41

Figure 14. Example inelastic α spectra for ^{54}Fe are shown. The lines are examples of continua chosen for analyses. 42

Figure 15. Inelastic α spectra obtained for ^{44}Ca are shown. The lines are examples of continua chosen for analyses. 47

Figure 16. The angular distributions of the ^{44}Ca cross sections for three excitation ranges of the GR peak and the continuum are plotted vs. center-of-mass scattering angle. Each bin is 480 keV wide and the average energies for each bin are shown. The lines through the data points indicate the multipole fits. The contributions of each multipole are shown. The statistical errors are smaller than the data points. 49

Figure 17. Strength distributions obtained for ^{44}Ca are shown by the histograms. Error bars represent the uncertainty based on the fitting of the angular distributions and different choices for the continuum, as described in the text. Gaussian fits to the E1 distributions for the individual peaks

(blue and purple) and their sum (red) are shown. The green lines are the strength distributions obtained with the HF-RPA calculations using the KDE0v1 interaction, smeared to more closely represent the data as discussed in the text. 53

Figure 18. Experimental results for ISGMR energies in ^{40}Ca [36], ^{44}Ca (present work), and ^{48}Ca [28] (blue diamonds) are compared with theoretical predictions. The results of fully self-consistent HF-RPA calculations [29] with KDE0v1 [72] are shown using the experimental excitation energy range (E=9.5-40 MeV) (red squares). 57

Figure 19. Centroid energies (m_1/m_0) for the ISGMR are plotted as a function of A. Lines representing $36/A^{1/6}$ and $40/A^{1/5}$ show the approximate systematic trend. The nuclei studied are ^{40,48}Ca [28]; ^{46,48}Ti [31]; ^{56}Fe and ^{58,60}Ni [26]. 64

Figure 20. GMR strength distributions for ^{46,48}Ti, ^{48}Ca, ^{56}Fe, ^{58}Ni, and ^{60}Ni are shown by the histograms. Each shows an asymmetric distribution, with a tail on the high side of the excitation energy, compared to a Gaussian shape (smooth, solid line in each except for the case of ^{48}Ca) [28]. In the ^{58}Ni E0 strength distribution, the open circles indicate the strength distribution from Ref. [76] and dark blue histogram indicates the strength distribution from Ref. [26] 65

Figure 21. Inelastic α spectra obtained for ^{54}Fe are plotted vs. excitation energy. The lines are examples of continua chosen for analyses. 67

Figure 22. Inelastic α spectra obtained for ^{64}Zn are plotted vs. excitation energy. The lines are examples of continua chosen for analyses. 68

Figure 23. Inelastic α spectra obtained for ^{68}Zn are plotted vs. excitation energies. The lines are examples of continua chosen for analyses. 68

Figure 24. The Giant Resonance peak is “sliced” into 300 keV bins for multipole decomposition analysis. 70

Figure 25. The angular distributions of the ^{54}Fe cross sections for three excitation ranges of the GR peak and the continuum are plotted vs. center-of-mass scattering angle. Each bin is 472 keV wide and the average energies for each bin are shown. The lines through the data points indicate the multipole fits. The contributions of each multipole are shown. The statistical errors are smaller than the data points. 71

Figure 26. The angular distributions of the ^{68}Zn cross sections for three excitation ranges of the GR peak and the continuum are plotted vs. center-of-mass

scattering angle. Each bin is 316 keV wide and the average energies for each bin are shown. The lines through the data points indicate the multipole fits. The contributions of each multipole are shown. The statistical errors are smaller than the data points. 72

Figure 27. Strength distributions obtained for ^{54}Fe are shown by the histograms. Error bars represent the uncertainty based on the fitting of the angular distributions and different choices for the continuum, as described in the text. Parameters for moments of the strength distributions are in Table IX. For E1, two Gaussian fits for the low component (purple, smooth line) and high component (blue line) are shown as a sum (red line). A single Gaussian fit is shown for E2. The green lines are the strength distributions obtained with the HF-RPA calculations using the KDE0v1 interaction, smeared to more closely represent the data as discussed in the text. The Gaussian fit parameters and moments obtained from the calculations are shown in Table X. 76

Figure 28. Strength distributions obtained for ^{64}Zn are shown by the histograms. Error bars represent the uncertainty based on the fitting of the angular distributions and different choices for the continuum, as described in the text. The green lines are the strength distributions obtained with the HF-RPA calculations using the KDE0v1 interaction, smeared to more closely represent the data as discussed in the text. The smooth red lines show Gaussian fits, the parameters of which are in Table XIII..... 78

Figure 29. Strength distributions obtained for ^{68}Zn are shown by the histograms. Error bars represent the uncertainty based on the fitting of the angular distributions and different choices for the continuum, as described in the text. The smooth lines show Gaussian fits, the parameters of which are in Table XV. The green lines are the strength distributions obtained with the HF-RPA calculations using the KDE0v1 interaction, smeared to more closely represent the data as discussed in the text. 81

Figure 30. Experimental GMR energies (represented by solid circles) are compared with values calculated by RMF parameterizations [75] (red squares and green triangles) and Skyrme non-relativistic parameterization [14] (blue diamonds). The error bars on the data include systematic errors. The light blue squares are the values obtained from the KDE0v1 interaction. The experimental energies for ^{40}Ca from Ref. [49]; ^{56}Fe, ^{58}Ni, and ^{60}Ni from Ref. [26]; and ^{90}Zr from Ref. [74] are included. 86

Figure 31. The centroid of the Gaussian fit (blue diamonds) to the low and high energy peak in the ISGDR distributions for ^{54}Fe, ^{64}Zn, and ^{68}Zn are

plotted vs. A. The error bars indicate the uncertainty obtained using the errors shown in Tables X, XIII, and XVI. The red squares show m_1/m_0 in the range $9 \leq E_x \leq 20$ MeV for the low peak and the range $20 \leq E_x \leq 36$ MeV for the high peak calculated with HF-RPA using the KDE0v1 interaction. 89

Figure 32. Inelastic α spectra obtained for ^{94}Mo are plotted vs. excitation energy. The lines are examples of continua chosen for analyses. 95

Figure 33. The angular distributions of the ^{94}Mo cross sections for three excitation ranges of the GR peak and the continuum are plotted vs. center-of-mass scattering angle. Each bin is 480 keV wide and the average energies for each bin are shown. The lines through the data points indicate the multipole fits. The contributions of each multipole are shown. The statistical errors are smaller than the data points. 98

Figure 34. Strength distributions obtained for ^{94}Mo are shown by the histograms. Error bars represent the uncertainty based on the fitting of the angular distributions and different choices for the continuum, as described in the text. Gaussian fits to the E0 and E1 distributions for the individual peaks (blue and purple) and their sum (red) are shown. The green lines are the strength distributions obtained with the HF-RPA calculations using the KDE0v1 interaction, smeared to more closely represent the data as discussed in the text. 102

Figure 35. The centroids of the Gaussians obtained from the fits to the E0 distributions for the Mo isotopes are plotted vs. A. The (red) lines show $74A^{-1/3}$ and $109A^{-1/3}$ in the upper and lower plots respectively. The error bars represent the uncertainty in energy for ^{94}Mo, but Ref. [67] did not report the uncertainties for the other isotopes. 105

Figure 36. The centroids of the Gaussian fits to the low and high energy peaks in the ISGDR distributions for each of the Mo isotopes from Ref. [67] and ^{94}Mo from this work are plotted vs. A in the top panels. The strength in the low and high peak is plotted in the lower panels. The error bars indicate the uncertainty obtained using the errors shown in Table XX. The squares (red) show m_1/m_0 and the strength in the range $9 \leq E_x \leq 20$ MeV for the low peak and the range $20 \leq E_x \leq 36$ MeV for the high peak calculated with HF-RPA using the KDE0v1 interaction. 108

Figure 37. The m_1/m_0 energy of the E2 strength in each of the Mo isotopes from Ref. [67] (blue diamonds) and ^{94}Mo from this work (light blue circle) is plotted vs. A. The error bars indicate the uncertainty obtained using the errors shown in Table XX. Also shown with error bars are centroids reported in Ref. [80] (green triangles) and a measurement for ^{92}Mo

[81] (purple X). The red squares show the centroid of the E2 strength obtained from HF-RPA calculations with the KDE0v1 interaction. 110

Figure 38. Values of K_A from the scaling energy $\sqrt{(m_3/m_1)}$ for the Ca isotopes are plotted against A. A fit to the data (red line) using the Leptodermous expansion with the parameters indicated is shown. The green line is shown as a reference and is also from the Leptodermous expansion but with a large, negative value for K_τ.....114

LIST OF TABLES

Page

Table I. The voltages and currents used for a typical giant resonance experiment are listed. 24

Table II. Optical Model and Fermi parameters used in DWBA calculations are listed, r_{c0} is the Coulomb radius parameter. 47

Table III. Smearing widths for the calculated distributions are shown. 52

Table IV. Parameters for energy moments obtained for isoscalar multipoles in ^{44}Ca are listed. The moments from the KDE0v1 calculation results are over the experimental energy range 9≤Ex≤40 MeV. 54

Table V. Parameters obtained for Gaussian fits for isoscalar multipoles in ^{44}Ca are listed. 54

Table VI. Parameters obtained for energy moments from the KDE0v1 calculation are listed. The results are over the experimental energy ranges (E1 low range: 9≤Ex≤20 MeV, E1 high range: 20≤Ex≤40 MeV, and E2: 9≤Ex≤40 MeV) 55

Table VII. Optical parameters used in the DWBA calculations are shown. r_p and r_t are the Coulomb radius parameters for the projectile and target, respectively. 69

Table VIII. Smearing widths for the calculated distributions are shown for ^{54}Fe, ^{64}Zn, and ^{68}Zn. 75

Table IX. Parameters obtained for the moments of isoscalar multipoles in ^{54}Fe are shown. The KDE0v1 results are over the experimental energy range (9≤Ex≤40 MeV). 77

Table X. Parameters obtained for Gaussian fits for isoscalar multipoles in ^{54}Fe are shown. 77

Table XI. Parameters obtained for energy moments of ^{54}Fe from the KDE0v1 calculation are shown. The results are over the experimental energy ranges (E1 low range: 9≤Ex≤20 MeV, E1 high range: 20≤Ex≤40 MeV, and E2: 9≤Ex≤40 MeV). 78

Table XII. Parameters obtained for the moments of the isoscalar multipoles in ^{64}Zn are shown. The KDE0v1 results are over the experimental energy range ($9 \leq E_x \leq 40$ MeV) 79

Table XIII. Parameters obtained for Gaussian fits for isoscalar multipoles in ^{64}Zn are shown. 79

Table XIV. Parameters obtained for energy moments of ^{64}Zn from the KDE0v1 calculation are shown. The results are over the experimental energy ranges (E1 low range: $9 \leq E_x \leq 20$ MeV, E1 high range: $20 \leq E_x \leq 40$ MeV, and E2: $9 \leq E_x \leq 40$ MeV). 80

Table XV. Parameters obtained for isoscalar multipoles in ^{68}Zn are shown. The KDE0v1 results are over the experimental energy range ($9 \leq Ex \leq 40$ MeV). 82

Table XVI. Parameters obtained for Gaussian fits for isoscalar multipoles in ^{68}Zn are shown. 82

Table XVII. Parameters obtained for energy moments of ^{68}Zn from the KDE0v1 calculation are shown. The results are over the experimental energy ranges (E1 low range: $9 \leq Ex \leq 20$ MeV, E1 high range: $20 \leq Ex \leq 40$ MeV, and E2: $9 \leq Ex \leq 40$ MeV) 83

Table XVIII. Optical Model and Fermi parameters used in DWBA calculations for ^{94}Mo are shown, r_{c0} is the Coulomb radius parameter. 96

Table XIX. Smearing widths for the calculated distributions are shown. 101

Table XX. Parameters for energy moments obtained for isoscalar multipoles in 94Mo are shown. The moments from the KDE0v1 calculation results are over the experimental energy range $9 \leq Ex \leq 40$ MeV. 103

Table XXI. Parameters obtained for Gaussian fits for isoscalar multipoles in ^{94}Mo are shown. 103

Table XXII. Parameters obtained for energy moments from the KDE0v1 calculation are shown. The results are over the experimental energy ranges (E1 low range: $9 \leq Ex \leq 20$ MeV, E1 high range: $20 \leq Ex \leq 40$ MeV, E2: $9 \leq Ex \leq 40$ MeV, and E3: $14 \leq Ex \leq 40$ MeV) 104

1 INTRODUCTION

1.1 Giant Resonances

Giant Resonances are the broad resonances that occur at excitation energies between 10 and 30 MeV. The first Giant Resonance was discovered by Baldwin and Klaiber [1] in 1947 when they observed a strong resonance behavior in photon-induced reactions. This strong resonance was later identified to be a collective vibration by Goldhaber and Teller [2] and was named the Giant Dipole Resonance, now referred to as the electric Isovector Giant Dipole Resonance [3]. The Isovector Giant Quadrupole Resonance (IVGQR) was first reported in 1972 and was excited by inelastic electron scattering in ^{90}Zr. The Isoscalar Giant Quadrupole Resonance (ISGQR) was first observed in electron scattering [4] and in proton inelastic scattering [5] in spherical nuclei. It was then confirmed by α inelastic scattering which was then used to investigate ISGQR in the heavy to light nuclei [6--9]. In 1977, Youngblood *et al.* reported the discovery of the Isoscalar Giant Monopole Resonance (ISGMR) in ^{144}Sm and ^{208}Pb with α inelastic scattering [10]. The Isoscalar Giant Dipole Resonance (ISGDR) was observed in ^{208}Pb in 1980 with 172 MeV α inelastic scattering [11].

In a macroscopic description, the giant resonances can be understood to be caused by the collective motion of nucleons within the nucleus, induced by static or dynamic deformations of the nuclear density. The resonances are classified by spin as electric oscillations (ΔS=0) or magnetic oscillations (ΔS=1). They are also classified by isospin,

where $\Delta T=0$ is the isoscalar mode and $\Delta T=1$ is the isovector mode. In the isoscalar mode the protons and neutrons move in phase, while in the isovector mode the protons and neutrons move out of phase. The multipolarity is determined by the angular momentum L.

In a microscopic description, the giant resonance modes are due to collective particle-hole excitations and are characterized by their parity, angular momentum, spin, and isospin. Here the resonances are the result of a coherent superposition of the particle-hole excitations caused by the action of an electromagnetic operator on the ground state of the nucleus.

Alpha inelastic scattering is a useful tool for studying isoscalar giant resonances because it is a strong isoscalar (N=Z) selective probe. The IVGDR is very near the ISGMR in excitation energy, thus a probe that excites both isoscalar and isovector modes (such as electron inelastic scattering) would make separating the strengths of the two excitations very difficult.

1.2 Incompressibility of Nuclear Matter

Nuclear matter is defined as an infinite system of nucleons with a fixed ratio of neutrons to protons and no Coulomb interaction. The main goal of the study of nuclear matter is to determine the Equation of State (EOS) $E=E(\rho)$. The EOS is characterized by the

saturation density ρ_0, the binding energy $E(\rho_0)$, and the nuclear matter incompressibility K_{NM}. The incompressibility of nuclear matter can be related to the curvature of the nuclear matter EOS by the relation [12]

$$K_{NM} = k_f^2 \frac{d^2\left(\frac{E}{A}\right)}{dk_f^2}\bigg|_{k_{f0}} = 9\rho_0^2 \frac{d^2\left(\frac{E}{A}\right)}{d\rho^2}\bigg|_{\rho_0} \quad (1)$$

Where E/A is the binding energy per nucleon of nuclear matter and k_{f0} is the Fermi momentum.

The ISGMR is interesting because its excitation energy is directly related to the incompressibility of the nucleus K_A,

$$E_{GMR} = \sqrt{\left(\frac{\hbar^2 K_A}{m\langle r^2\rangle}\right)} \quad (2)$$

where $\langle r^2\rangle$ is the mean square radius and m is the mass of the nucleon [13,14].

The ISGDR can be related to K_A by

$$E_{GDR} = \sqrt{\frac{\frac{7}{3}\hbar^2\left(K_A + \frac{27}{25}\epsilon_F\right)}{m\langle r^2\rangle}}, \quad (3)$$

where $\epsilon_F = \frac{k_{f0}^2}{2m}$, is the Fermi energy.

K_A can be used to obtain the incompressibility of nuclear matter K_{NM}, but this extrapolation from the data for real nuclei is not straightforward due to contributions from surface, Coulomb and asymmetry effects.

K_{nm} can be obtained by extrapolating from K_A obtained for many nuclei with an $A^{-\frac{1}{3}}$ Leptodermous expansion [14,15],

$$K_A = K_{NM} + K_S A^{-\frac{1}{3}} + K_\tau \delta^2 + \frac{K_{Coul} Z^2}{A^{\frac{4}{3}}} + \cdots \quad (4)$$

which is a parameterization similar to that of the nuclear mass formula; with volume (K_{NM}), surface (K_S), symmetry (K_τ, δ = (N-Z)/A) and Coulomb (K_{Coul}) terms. This macroscopic approach is straightforward, but it has been shown that these parameters, when obtained by fitting to the ISGMR data, are unreliable [16,17].

E_{GMR} can also be related to K_{nm} by calculations using mean fields. These include the fluid dynamics approach [18], the Hartree-Fock – Random Phase Approximation (HF-RPA) with effective interactions [19], the RPA based on separable Hamiltonians [20], linear response within a stochastic one-body transport theory which incorporates coherent and collisional damping [21], the relativistic transport approach [22], and the relativistic RPA [23]. In the RPA approach, non-relativistic (Skyrme, Gogny) or relativistic (NL1, NL3) effective interactions are used [24], and the values of K_{NM} and the density dependence of E_{sym} are deduced from the interaction that best reproduces the experimental data on the strength functions of the giant resonance [12,25]. At present, the best value for K_{nm} is 220-240 MeV [24].

1.3 Nuclei to Study

The centroids of the GMR as a function of atomic number A are plotted in Figure 1 and show a lot of variation, and the behavior is not fit very well with the $A^{-1/5}$ or $A^{-1/6}$ lines which are shown for reference [26]. Some examples of local deviations include E_{GMR} for ^{48}Ca, which is higher than for ^{40}Ca. Also, E_{GMR} for ^{58}Ni is higher than would be expected from the systematics and the Mo and Zr isotopes show large deviations from the general trend.

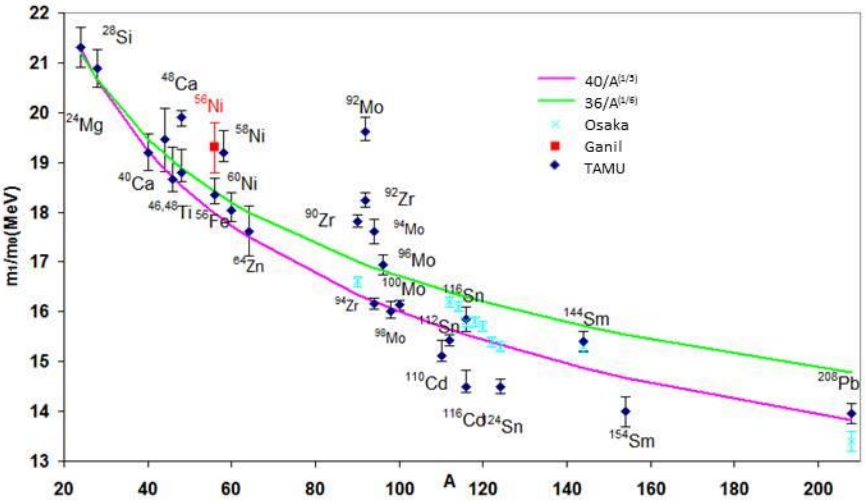

Figure 1. Centroid energies (m_1/m_0) for the ISGMR are plotted as a function of A. Lines representing $36/A^{1/6}$ and $40/A^{1/5}$ are shown for reference.

The GMR strength distribution had been observed to transition in shape from symmetric (Gaussian-like) in heavier nuclei to asymmetric over the 40<A<90 region [27]. The origin of this is not clear and may be the result of nuclear structure or some other effect. This suggested a study of the GMR in ^{44}Ca, ^{54}Fe, ^{64}Zn, and ^{68}Zn. In the A~90 region for

Zr and Mo, a second unexplained peak can be seen in the strength distribution for the GMR [28]. Analysis of the GMR in ^{94}Mo may help to explain this characteristic. Each mass region is discussed separately below.

1.3.1 A=40-48

The isoscalar E0-E3 giant resonances for ^{40}Ca and ^{48}Ca were investigated by Lui *et al.* [29]. Figure 2 shows from a plot from Ref. [29] of ^{40}Ca and ^{48}Ca ISGMR energies from various calculations compared to experimental energies as well as the energy difference between ^{48}Ca – ^{40}Ca. By studying ^{44}Ca we may be able to learn more about this issue. From the plot of the systematics of GMR energy with mass number A in Figure 1. ^{48}Ca is a little high, yet ^{40}Ca is in general agreement.

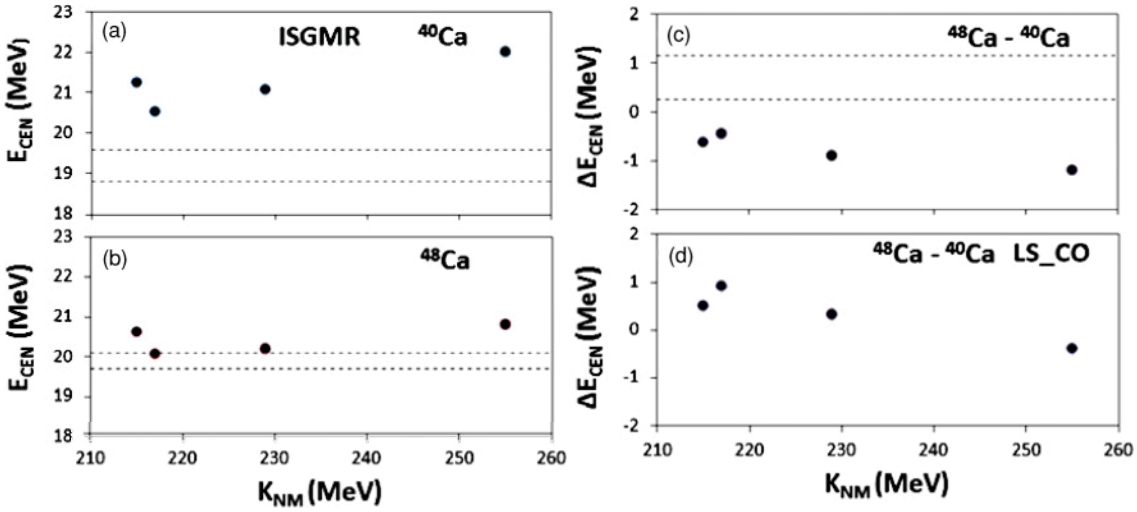

Figure 2. Centroid energies (E_{CEN}) for ^{40}Ca and ^{48}Ca and the energy difference (ΔE_{CEN}) obtained with HF-RPA calculations are plotted for different Skyrme interactions having different values of K_{NM}. (a) and (b) compare the calculated and experimental values for the centroid energy in ^{40}Ca and ^{48}Ca, respectively. The dashed lines represent the experimental value and its error. (c) and (d) compare the calculated with the experimental difference in centroid energy. In (d), the RPA calculations are done without the Coulomb and spin-orbit interactions. From Ref. [29].

In contrast, HF-RPA calculations of the centroid energy for different Skyrme interactions were higher than the experimental data for ^{40}Ca and were also higher but closer to agreement with the data for ^{48}Ca (Figure 2) [29]. Because the ratio of $\frac{N-Z}{A}$ is 0.166 in ^{48}Ca, zero in ^{40}Ca and 0.091 in ^{44}Ca, this study also presents a good test for how strongly correlated K_{nm} and symmetry energy are with the centroid energy of the GMR [30].

1.3.2 ^{54}Fe, ^{64}Zn, and ^{68}Zn

One consideration in the choice to look at these particular targets, is that it is difficult to find suitable targets in the mass region 60<A<90. For example, targets of selenium and strontium are hard to maintain because of oxidation. In the case of germanium, it is difficult to get a target of suitable thickness.

The E0 strength distributions have shapes which have been found to vary with A, and further measurements in the mid-mass range 40≤A≤90 are necessary to help explain the observed trends. Measurement of the GMR in ^{64,68}Zn is particularly useful because of the gap in measurements in the region 60≤A≤90. Measurement of ^{54}Fe could be useful to study because it is between ^{48}Ca and ^{58}Ni in mass, and these nuclei have been found to have similarly high values for m_1/m_0 relative to the systematic behavior of the experimental data. In heavy nuclei (A≥110), the strength distribution of the GMR has a symmetric, Gaussian shape [31]. In the A≈90 region, the strength distribution consists of a high and low-energy component separated by 7-9 MeV [28]. The observed high-energy component remains unexplained. In nuclei with A≤28, the GMR becomes fragmented [27]. A number of nuclei have already been studied in the mass range A = 40 to 90 and the m_1/m_0 centroid energies for these nuclei are shown in Figure 3 [27,29,32]. In this mass region, the shape of the strength distribution generally has a tail on the high-excitation side of the GMR [27,29,32]. This tailing has been predicted by microscopic

calculations for ^{58}Ni using a microscopic nuclear structure model that includes known mechanisms of giant resonance damping (such as the spreading width caused by more complex 1p1h couple to phonon configurations and the escape width because of inclusion of the single-particle continuum) [33]. Also, this tailing has been observed in the E0 strength distributions for ^{46,48}Ti, ^{56}Fe, ^{58}Ni, ^{60}Ni, and ^{48}Ca. ^{48}Ca shows large tailing on the high excitation side which extends to 40 MeV, whereas the other nuclei have strength which extends to 35 MeV. Microscopic calculations of the E0 strength distribution by Kamerdzhiev [33,34] were in very good agreement with the experimental distribution for ^{40}Ca and ^{58}Ni but not for ^{48}Ca. A similar calculation by Hamamoto [35]for ^{40}Ca was in poor agreement with the experimental distribution [29].

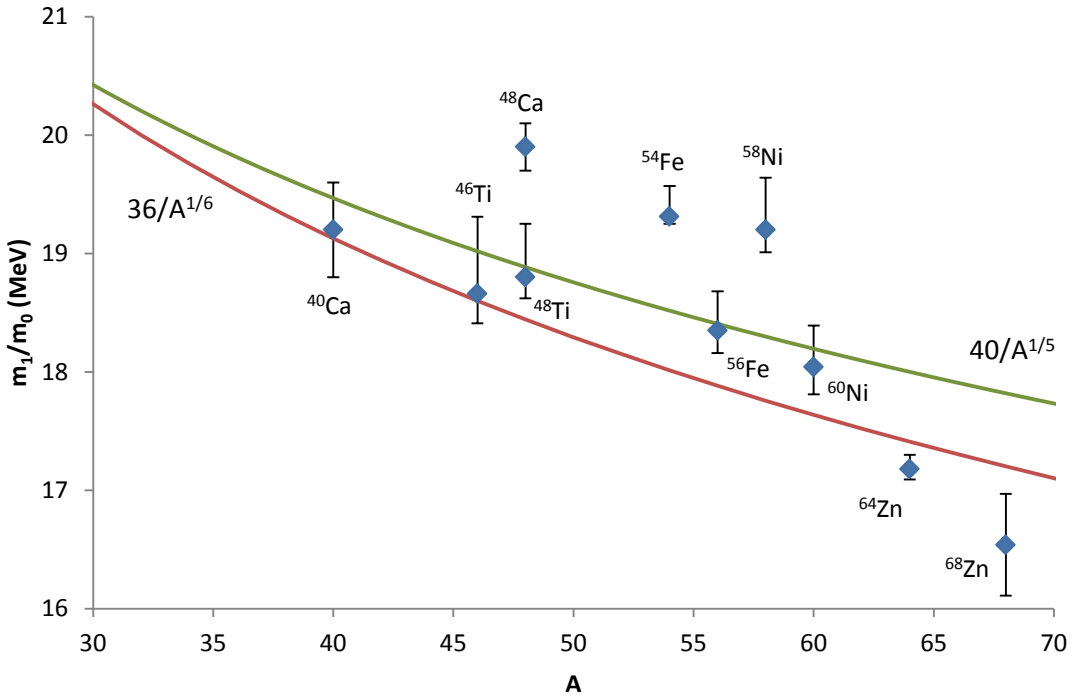

Figure 3. Centroid energies (m_1/m_0) for the ISGMR are plotted as a function of A. Lines representing $36/A^{1/6}$ and $40/A^{1/5}$ show the approximate systematic trend. The nuclei shown are ^{40,48}Ca [29]; ^{46,48}Ti [32]; ^{56}Fe and ^{58,60}Ni [27]. The values from this work for ^{54}Fe and ^{68}Zn are included as well.

1.3.3 ^{94}Mo

For the nuclei $^{90, 92, 94}$Zr and $^{92, 96, 98, 100}$Mo, the monopole strength is separated into two parts (Figure 4) [28].

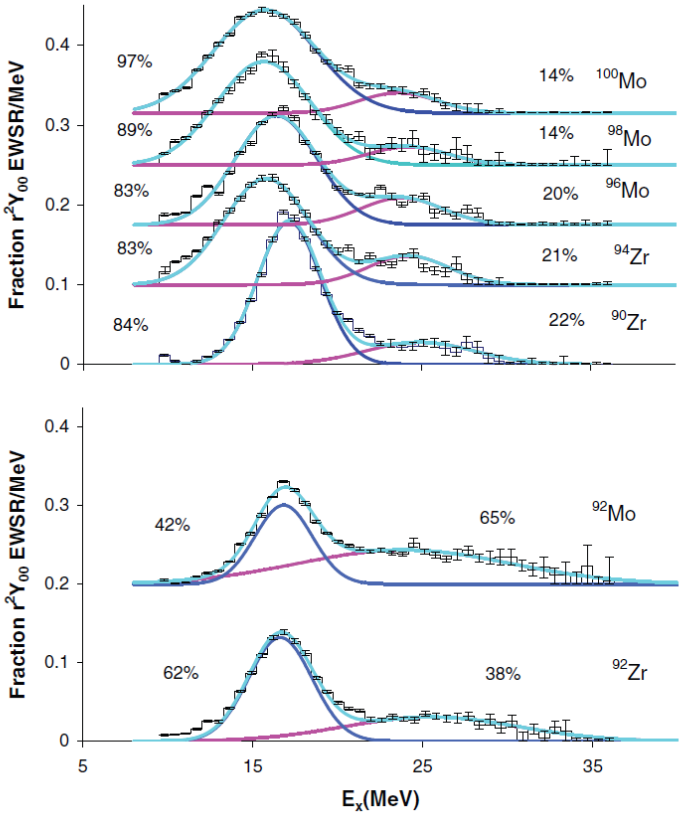

Figure 4. The black histograms show the fraction of the r^2Y_{00} sum rule obtained for Mo and Zr isotopes plotted as a function of excitation energy. Superimposed are Guassian fits to the two components of the distributions as well as the sum of the fits. From Ref. [28].

For the nuclei with A ≠ 92, 80-90% of the strength is in the lower energy peak located at 15.7 to 17.2 MeV. In the A = 92 nuclei, there is considerably more strength in the higher energy peak than in the higher energy peak of the A ≠ 92 nuclei. The higher energy second peak is not predicted by the HF-RPA calculations that reproduce the ISGMR energies in the other isotopes that are generally used to relate K_{NM} to K_A.

In the HF-RPA calculations used to relate ISGMR energies to K_{NM}, it has been widely assumed that the energy of the ISGMR is not affected by the details of the nuclear structure. Scaling model values from K_A are obtained from the $\sqrt{\frac{m_3}{m_1}}$ scaling energies and are compared to HF-RPA calculations in Figure 5. These calculations for K_A fail to predict the stiffness seen at A=92 for both Zr and Mo isotopes. One possibility considered in Ref. [28] is that the higher energy peak is the overtone. The ISGMR corresponds to $2\hbar\omega$ transitions, whereas the overtone of the ISGMR, from a microscopic point of view, corresponds to $4\hbar\omega$ particle-hole transitions. This possibility was investigated for the ^{92}Mo case [28] and produces a reasonable result, assuming that 100% of the overtone strength is located at twice the energy of E0. This approach yields a K_A for ^{92}Mo of 179 MeV, which is still 27 MeV greater than with what is expected from HF-RPA calculation. Yet, there is no obvious reason why the overtone would be present in the A = 92 nuclei only, so this observed stiffness must be to the ISGMR alone. Neither Cd, nor Sn isotopes have the extra peak found in the ISGMR strengths for Mo and Zr. Analysis of the GMR in ^{94}Mo may help to resolve these anomalies.

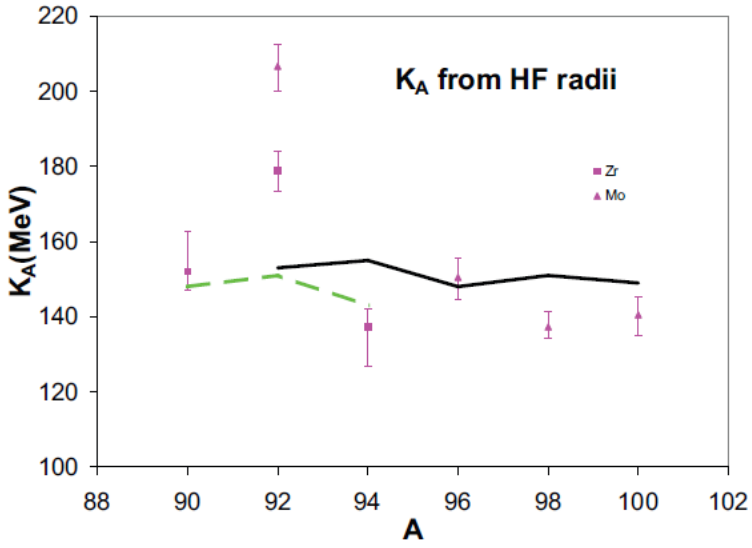

Figure 5. The scaling model K_A values obtained from measured scaling energies $(m_3/m_1)^{1/2}$ are shown for Zr and Mo isotopes by squares and triangles respectively and plotted versus A. The lines indicate the HF-based RPA values of K_A calculated within HF-RPA using the KDE0v1 interaction for Zr (green dashed line) and Mo (black solid line) isotopes. From Ref. [17].

1.4 Dissertation Outline

The dissertation consists of seven sections. Section 1 presents an introduction on Giant Resonances, nuclear compressibility, and nuclear matter compressibility. The motivations for studying the isoscalar giant resonances in ^{44}Ca, ^{54}Fe, ^{64}Zn, ^{68}Zn, and ^{94}Mo are also given in this section. In Section 2, the experimental setup of the multipole-dipole-multipole (MDM) spectrometer, the focal plane detector, and electronics are introduced. The methods for detector calibration and data processing to extract the differential cross-sections are in this section as well. The details of the data analysis, including a description of the Distorted Wave Born Approximation (DWBA) calculation of the inelastic scattering cross-sections are given in Section 3. The results for the

isoscalar resonances in these nuclei are in Sections 4-6 and are presented in three papers that are to be published. A description of the E0, E1, and E2 strengths and energies for ^{44}Ca is in Section 4. The strengths and energies are compared with prior results for ^{40}Ca and ^{48}Ca. They are also compared with the predictions of the strength distributions from HF-RPA calculations with KDE0v1 interaction. In a similar fashion, the results for ^{54}Fe, ^{64}Zn, and ^{68}Zn are in Section 5. These results are compared with prior results from other nuclei in the A=40-90 region and with results from HF-RPA calculations of the strength distributions. Section 6 has the results for ^{94}Mo, which are compared with the results from the other Mo isotopes and with the HF-RPA calculations. A summary of the results from the nuclei studied and conclusions are in Section 7.

2 EXPERIMENTAL PROCEDURE

2.1 Overview

Giant Resonances are studied using 240 MeV α particle inelastic scattering, which has been shown to provide a very good ratio of peak-to-continuum suitable for the identification of the isoscalar E0-E4 resonances [36,37]. Figure 6 shows the layout of the beam line components used for providing the 240 MeV α particle beam for Giant Resonance experiments. The Electron Cyclotron Resonance (ECR) source makes an ionized plasma of He^{2+} gas for injection into the Texas A&M K500 superconducting cyclotron which then accelerates α particles to 240 MeV. The beam is extracted and passed through the Beam Analysis System (BAS) [38] which improves beam energy resolution and reduces beam halo by dispersing the beam with a magnetic bend in an 88° segment and then by selecting a part of the beam with slits. In an intermediate segment, the beam is focused. A second magnetic bend, in an 87° segment in the opposite direction as the first, is used to remove slit scattered particles so that a clean beam can be transported to the Multipole-Dipole-Multipole (MDM) spectrometer for 0° inelastic scattering measurements.

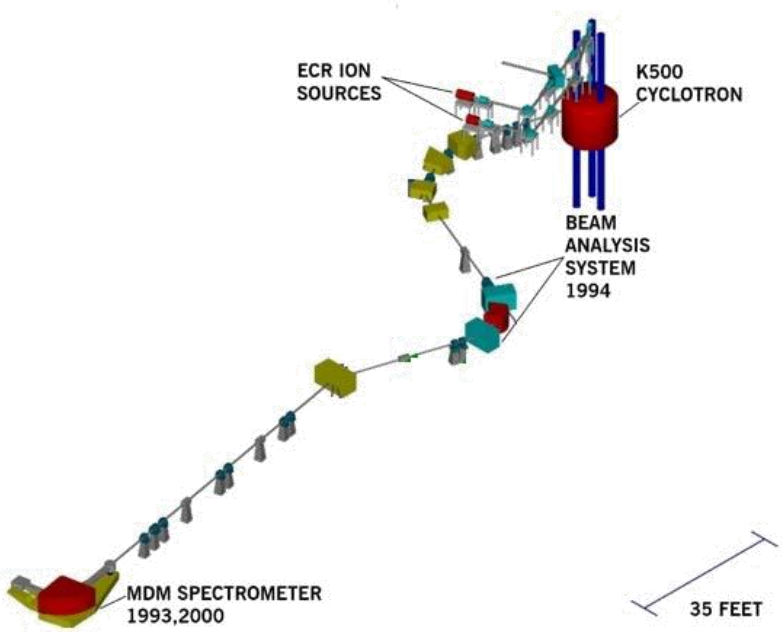

Figure 6. Diagram of the beam line for the MDM experiments is illustrated. The α particle beam begins at the ECR ion sources, is injected into the K500 Cyclotron for acceleration to 240 MeV, is passed through the Beam Analysis System, and then is transported to the MDM Spectrometer.

Figure 7 shows the layout of the target chamber, MDM spectrometer, and Focal Plane Detector. The beam enters the target chamber and bombards a thin, self-supporting target. The MDM spectrometer is used to separate particles by momentum and is described in Section 2.2. The Focal Plane Detector (described in Section 2.3) is an ionization chamber with 4 proportional counter wires for measuring position and angle. Cathode plates are for measuring energy loss. Mounted to the exit window on the outside of the ionization chamber is a plastic scintillator. It provides a fast timing signal for event trigger and measures the total energy of the analyzed α particle. The energy signals from the scintillator and the ΔE energy loss information from the ionization chamber are

combined to provide particle identification. The Gas System (described in Section 2.3.1) is used to provide a constant flow of a mixture of isobutane and alcohol through the ionization chamber and to maintain a constant pressure in the detector.

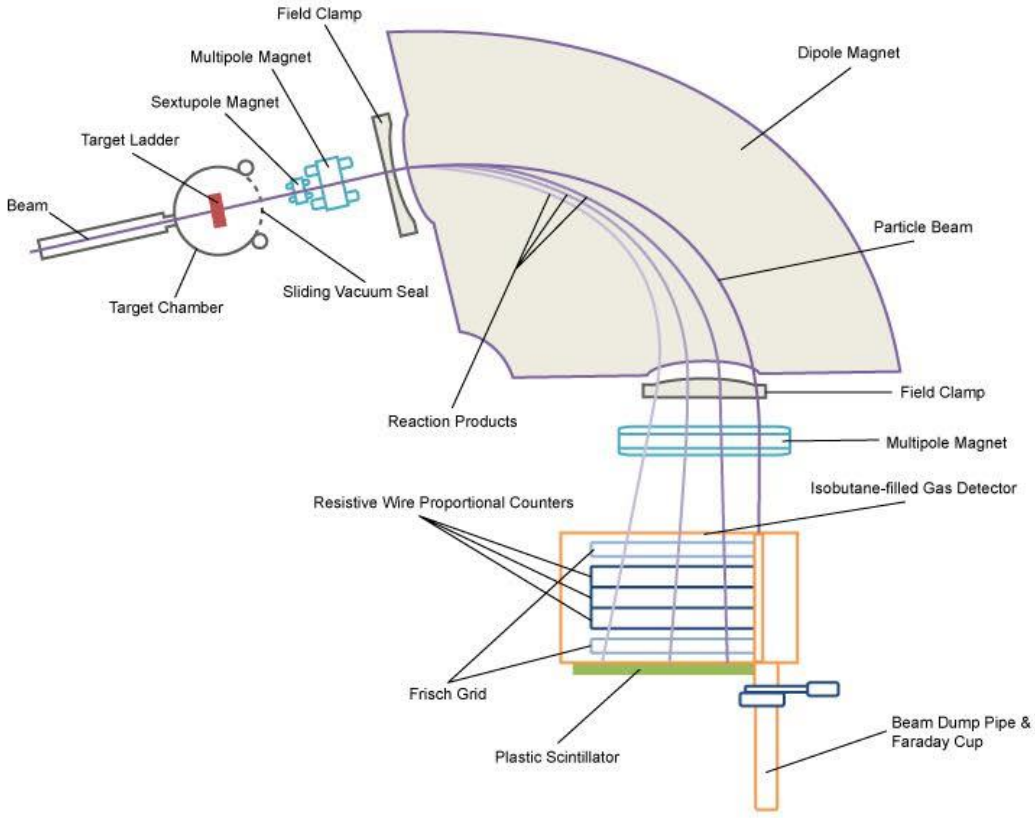

Figure 7. Diagram of the Experiment Layout is illustrated. The α particle beam bombards the target in the target chamber, goes through a 4°x4° slit in the slit box (not pictured, between target chamber and multipole magnet) and the MDM spectrometer, and is analyzed in the Focal Plane Detector.

The electronic components used for signal processing and data collection are described in Section 2.5, and the methods for calibrating the detector and processing data are described in Section 2.6.

2.2 MDM Spectrometer

The MDM spectrometer was constructed at Oxford University [39] in 1982 and moved to Texas A&M Cyclotron Institute to be used with the K500 cyclotron for a variety of experiments including giant resonance studies, nuclear spectroscopy, and mass measurements of exotic nuclei. The details of the MDM spectrometer design and operation can be found in Ref. [39]. It consists of a multipole magnet, a field clamp, a dipole magnet, another field clamp, and another multipole magnet. The dipole magnet has a linear gradient field and 100° of total bend with a 1.5 m central radius. It produces large dispersion with low magnification. The horizontal linear magnification is M_x=0.4, and the vertical linear magnification is M_y=5.0. The focal plane is essentially normal to the incident rays [40].

2.3 Focal Plane Detector

The Focal Plane Detector [41,42] has a length of 60 cm, vertical acceptance of 9 cm, and measures, for our purposes, α particles with an energy range of approximately 185 to 232 MeV ($8 \leq E_x \leq 55$ MeV depending on scattering angle). Its design and operation are detailed in Refs. [42,43]. The internal components are illustrated in a cross-section view of the Focal Plane Detector in Figure 8. It is comprised of a gas ionization chamber with cathode and anode plates, 4 resistive wire proportional counters, and a plastic scintillator detector that is coupled to a photomultiplier tube. A 25.4 μm thick Poly-Aramid foil is

used for the front window separating the detector from the spectrometer, and a 0.25 mm thick Mylar foil is used for the back window, separating the detector from the plastic scintillator.

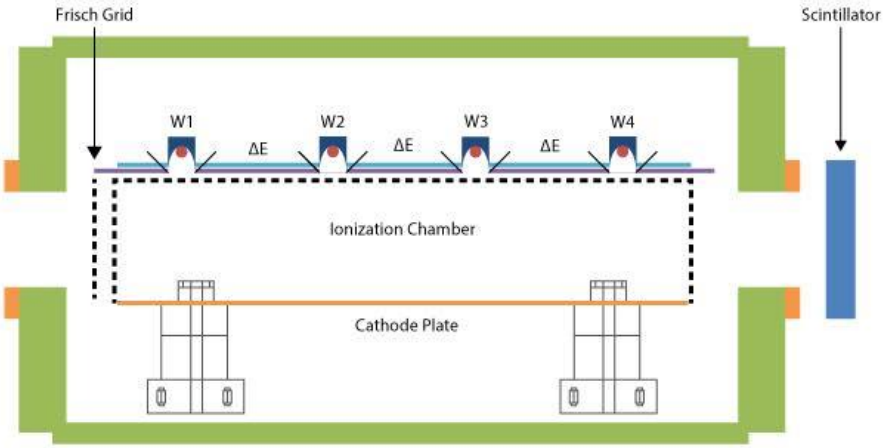

Figure 8. A cross-section view of the focal plane detector is shown. The beam enters the front window from the left and loses energy to the isobutane gas. Electrons from the beam path are measured by the position sensitive wires (W1-W4), and energy loss by the beam particle in the gas is measured by the 3 ΔE plates. The beam goes through the exit window on the right side and is stopped in the plastic scintillator.

2.3.1 Gas Ionization Chamber

The most basic design of a gas ionization chamber [44] consists of 2 plane parallel electrodes in a gaseous medium with an electrostatic field between the electrodes. Electrons freed by ionization are collected on the positive plate. In this simple design, the signal from the anode will have a nonlinear response to energy loss in the gas chamber because the positive ions, which have a mobility which is 1000 times slower

than electrons, induce a charge on the anode. A Frisch grid [45] is used to screen the effects of positive ions from the anode. It is a grid fixed at a lower voltage than the anode and is placed near the anode between it and the cathode.

The ionization chamber is filled with a mixture of 97% isobutane gas and 3% Dimethoxymethane alcohol with a gas pressure at 150 Torr. The alcohol is used to clean the wires. The flow of gas is continuous through the detector in order to avoid contamination from impurities in the gas which are caused by ionization. The control components and lines of gas flow for the system are shown in Figure 9.

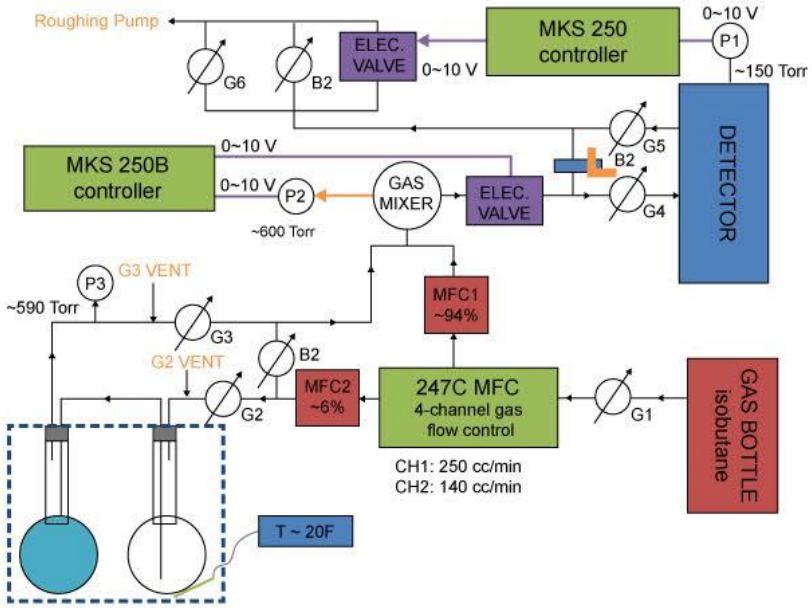

Figure 9. Schematic drawing of the Gas System is shown. Gas flow through the system is indicated by the lines with arrows. Valves are indicated by circles with diagonal arrows. Gas is mixed with alcohol from the refrigerator in the Gas Mixer before flowing through the ionization chamber (detector). The constant gas flow is maintained by 2 MKS controllers. Gas is pumped from the detector by the Roughing Pump.

The isobutane goes from the gas bottle to the 247C MFC gas flow controller and is split into two flows. Ninety-four percent of the gas goes directly to the gas mixer, and the remainder bubbles through the alcohol bottle before flowing to the gas mixer. The alcohol bottle is kept at a temperature of ≈20°F in a refrigerator (indicated in Figure 9 by the dashed blue line). The isobutane-alcohol mix goes through the electric valve and into the ionization chamber. The pressure in the gas mixer is maintained at 600 Torr by the MKS 250B controller using the electric valve and from measurement of the internal pressure of the detector from the MKS Baratron. The gas flows through the detector and is then pumped out by the roughing pump. The pressure in the detector is maintained by another electric valve and MKS 250B controller.

2.3.2 Resistive Wire Proportional Counters

Resistive wire counters [46] measure position by charge division. The charge is collected at each end of the wire and is proportional to the distance between the point where the charge is injected and the other end. There are four 60 cm long wires spaced at 13.55 cm intervals in the Focal Plane Detector. The wires (California Wire Company STABLOHM 675) have a diameter of 0.0007 in and resistance R=1678 Ω/ft. Horizontal *x* positions measured in coincidence from multiple wires are combined to give the θ angle measurement of the α particle ray. Ray tracing is used to calculate the angle and the position where the particle intercepts the focal plane.

The spectrometer angle is checked by determining the kinematic cross-over from the elastic scattering off hydrogen (in the ^{12}C target) and ^{12}C inelastic-scattering peaks.

2.3.3 Plastic Scintillator

An 81 cm long, 11 cm wide, and 3.7 cm thick BC400 plastic scintillator is mounted outside the exit window of the ionization chamber. A scintillator is a material which has a fluorescent response when exposed to ionizing radiation. Generally, the light response is linearly proportional to the incident ion energy [47]. It gives a fast timing signal and total energy signal of the α particle. A conical, Lucite light guide was glued to the scintillator and coupled to a Hamamatsu H1949 photo-multiplier tube (PMT), where the light response is converted into a current.

2.4 Experiment Details

Cross-sections are obtained from the charge collected, the target thickness, the dead time, and the known solid angle. The energy calibration for Giant Monopole Resonance experiments at 0° is checked by measurement of the 13.85 ± .005 MeV (L=0) state in ^{24}Mg.

When operating the MDM spectrometer at 0°, the beam is passed through a beam pipe on the high ρ (rigidity, $\vec{\boldsymbol{p}}/q$) side of the detector and is stopped in a Faraday cup inside the wall (see Figure 7). Shielding (consisting of lead bricks, plastic blocks, and paraffin

blocks) is placed between the beam pipe and detector to reduce the flux of neutrons and gamma rays to the detector. The beam pipe is inside the Focal Plane Detector and distorts the field in the ionization chamber, and a voltage is applied to the pipe to correct the field. With the MDM spectrometer at 4°, the beam is collected in a Faraday cup located in the slit box behind the target chamber.

2.5 Electronics and Data Acquisition

Two types of power supplies are used. The Tennelec TC 952 is used in applications which require several mA of current. It is used for the monitor detector inside the target chamber and to power the PMT connected to the scintillator of the focal plane detector. The BERTAN 375P(N) is used for applications that draw no or very little current. It is used to provide power to the resistive wire counters, the cathode, the beam pipe correction field, and the shell. The voltages applied to the components of the Focal Plane Detector are listed in Table I.

Table I. The voltages and currents used for a typical giant resonance experiment are listed.

	Wire 1	Wire 2	Wire 3	Wire 4	Cathode
HV (V)	1750	1750	1750	1750	-3000
Typical current	0 μA	0μA	0μA	0μA	16.1 μA
	Beam Pipe	Shell	Monitor	PMT	
HV (V)	-2233	199	-726	-1570	
Typical current	43.1 μA	20 μA	Several mA	Several mA	

The electronic components used for processing the signals from the components of the Focal Plane Detector are illustrated in Figure 10. The PMT dynode provides the energy loss signal, and the PMT anode is used to provide the fast timing trigger. The TENNELEC TC 455 constant-fraction discriminator (CFD) converts the anode signal into a logic signal. The CFD and the logic signal from a random time pulse generator and veto signal from the CBD 8210 (Branch Highway) are added by a coincident logic unit (PHILLIPS SCIENTIFIC 755). The logic signal is sent to the GG8000 to produce the gate signal for the ADC's. The 8 charge signals (consisting of the right and left side from each of the 4 resistive wire counters), the ΔE signal from the 3 collector plates, and the cathode signal are each sent to the CANBERRA 2004 preamplifiers. The output of the preamplifiers is a negative unipolar voltage pulse with a peak amplitude that is linearly proportional to the input charge. The preamp signal goes to the ORTEC 571 or 671 spectroscopy amplifiers to be shaped into a Gaussian pulse. These signals are then

converted into a digital signal by an AD413 or AD811. The PMT dynode signal is sent to the ORTEC 113 preamp, then to the ORTEC 571 spectroscopy amplifier to be shaped into a Gaussian pulse and is then converted into a digital signal by the AD811.

The digitized signals are passed by a branch highway cable from the CAMAC to the VME front end, which consists of a VME crate with CBD8210 module and a Motorola MVME 712/M Ethernet interface. A Dell PowerEdge 1650 computer is used as the front end host server and is connected to the electronics by an optical fiber. The Dell PowerEdge 2950 is used to analyze the data on-line and to store the data on disk for off-line analysis.

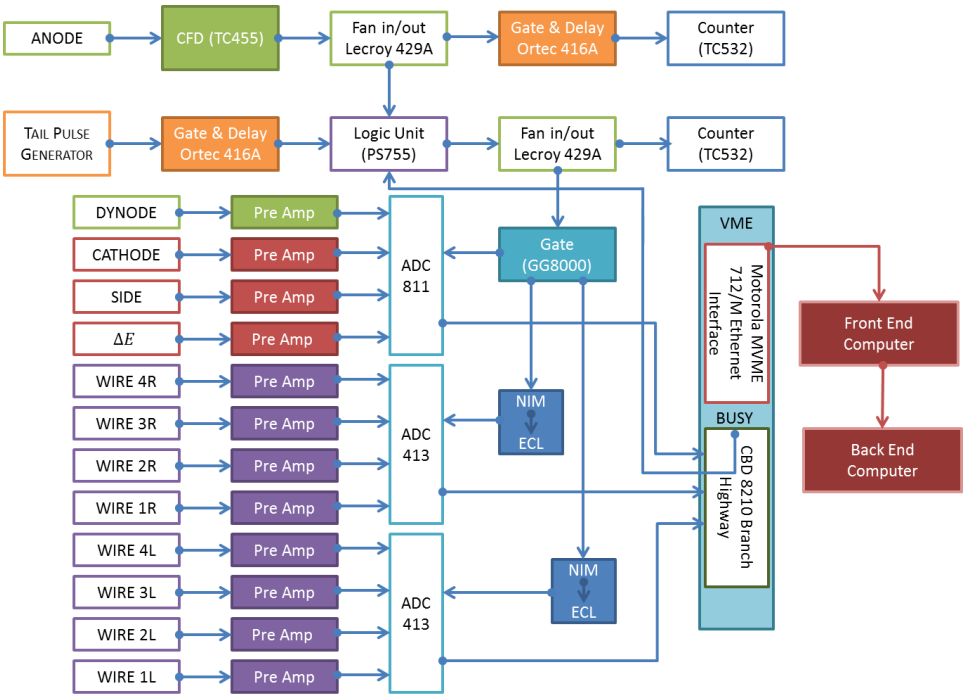

Figure 10. Schematic of the electronic components used for processing signals from the Focal Plane Detector is shown.

2.6 Detector Calibration

2.6.1 Position Calibration

Position calibration of the focal plane is done by doing a sweep over sixteen dipole field settings that span the useful length of the detector measuring the elastic scattering of α particles from ^{12}C. A slit with five 0.1° openings (shown in Figure 11) which correspond to -2°, -1°, 0°, 1°, and 2° relative to the central ray is placed at the entrance of the MDM spectrometer. Centroids of peaks corresponding to the five openings on the angle mask are obtained at each field setting. These positions are then compared to predictions of the horizontal *x* wire position corresponding to the incident α particle ray in centimeters

calculated with RAYTRACE [48] to obtain a relationship between the channel number and position along the focal plane for each of the four position wires.

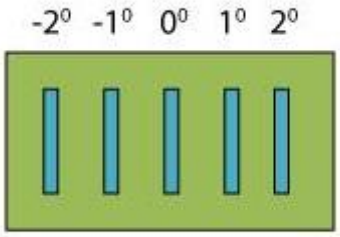

Figure 11. The five narrow opening slit used at the entrance of the spectrometer for position and angle calibration is illustrated.

2.6.2 Angle Calibration

Figure 12 shows the α particle passing through the Focal Plane Detector as a ray (labeled c). The horizontal positions of the ray are measured by Wire 1 (distance from one end labeled as y_{1c}) and Wire 4 (distance from one end labeled as y_{4c}). Wires 1 and 4 typically give the highest resolution angle measurement because of the distance between the wires (x_{14}).

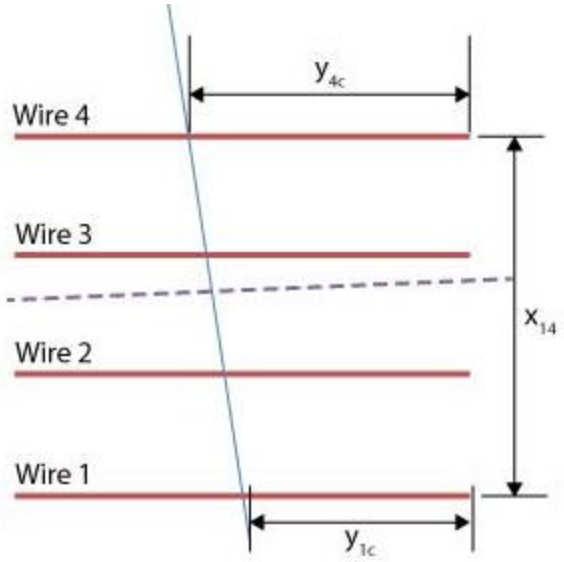

Figure 12. A ray (light blue solid line) in the detector is illustrated. The horizontal positions of the ray are measured from wire 1 and wire 4 in order to calculate the angle of the ray in the detector.

The angle of the ray in the detector (θ_{DC}) is calculated using the relationship $\tan\theta_{DC} = \frac{y_4 - y_1}{x_{14}}$ and can then be related to the angle of the α particle relative to the beam as it leaves the target. The angle calibration is done by measuring α particle inelastic scattering from ^{12}C and using the five narrow opening slit described above. In the spectrum of the angle of the α particle leaving the target relative to the beam direction, the channel numbers for the centroids of the five peaks are obtained and then fit with the linear relationship $\theta_i = a + bN$, where $\theta_i$is the angle corresponding to the slit opening , N_i is the peak position channel number, and a and b are fit parameters. The data set is then divided into ten angle bins with a width of $\Delta\theta = 0.4°$. The average angle of each bin is obtained by integrating over the height of the solid angle defining slit (4° x 4° for Giant Resonance data collection) and the width of the angle bin.

2.6.3 Energy Calibration

RAYTRACE [48] calculations are also used to give the relationship between the momentum of the α particles and their position on the focal plane. After the position calibration, the position spectrum can be converted into a momentum spectrum. Using relativistic kinematics, the momentum spectrum is converted into an energy spectrum. The energy calibration for inelastic scattering to the giant resonance region is done by measuring inelastic scattering from ^{12}C, ^{24}Mg, and ^{28}Si. In ^{12}C, the 3^- states are measured (E_x=9.641±0.005 and 18.35±0.05 MeV). In ^{24}Mg, the 2^+ states are measured (E_x=12.86±0.05 and 17.36±0.05 MeV). And in ^{28}Si, the 2^+ states are measured (Ex=18.67±0.05, 20.43±0.05 MeV).

2.6.4 Data Processing

The raw data files for each run are sorted into 10 position spectra which correspond to the 10 angle bins described in the Angle Calibration section (Section 2.6.2). These spectra are then converted into excitation energy spectra. The experimental differential cross section for a given excitation energy and angle bin is given by

$\frac{d\sigma}{d\Omega} = \frac{N'}{IN_T} = \frac{Y \times DT}{\frac{Q}{Z_P} \times T \times \Delta\Omega}$, where N' is the reaction number per second, I is the incident flux, and N_T is the number of target nuclei per unit area. Y is the number of events in an angle bin and excitation energy range, Q is the total charge collected in the Faraday cup during the run, Z_P is the charge of the incident particle, and $\Delta\Omega$ is the solid angle. The overall

(DT) dead time of the electronics and data acquisition is measured by passing pulses from a random (in time) pulser into the preamplifiers, through the electronics, and into the computer. The number of pulses sent to the computer is compared with the number in the spectra. Target thickness (T) is measured by weighing and is checked by measuring the energy loss of the 240 MeV α beam.

3 DATA ANALYSIS

3.1 Overview

Inelastic α scattering is used to study the isoscalar giant resonances because it is a strong isoscalar (N=Z) selective probe [3]. It has been shown to yield low background at high excitation energy in isoscalar giant resonance scattering experiments with most nuclei [36,43,49,50]. The GR excitations can be described macroscopically via the Collective Model [12] or microscopically using some approach such as Hartree-Fock Random Phase Approximation (HF- RPA) [12,51,52]. In the analysis described here, the method for calculating the isoscalar giant resonances for the different multipoles is a hybrid of macroscopic and microscopic approaches. Due to the angular range of the data taken, it is not possible to distinguish L≥ 4 multipoles so the analysis is limited to L=0-4 multipoles.

Isoscalar giant resonances of all multipoles are excited by the isoscalar nuclear probe. To extract the strength distribution for a particular multipole, the differential cross section $\frac{d\sigma}{d\Omega}$ for inelastic scattering must be calculated. The scattering is calculated in Distorted Wave Born Approximation (DWBA) using an Optical Model Potential as described by Satchler and Khoa [53]. For the Schrodinger Equation (5) written with an Optical Potential U_{OP},

$$(\nabla^2 + k^2)\psi = \frac{2m}{\hbar^2} U_{OP}\psi \tag{5}$$

the DWBA outgoing distorted wave $\psi_k^{(+)}$

$$\psi_{\boldsymbol{k}}^{(+)} \approx N(e^{i\boldsymbol{k}\cdot\boldsymbol{r}} + \frac{e^{ikr}}{r} f_{\boldsymbol{k}}(\boldsymbol{r})) \tag{6}$$

in the asymptotic solution has the form in Eqn. (6). The cross-section

$$\frac{d\sigma}{d\Omega} = |f_k(\hat{\boldsymbol{r}})|^2 \tag{7}$$

can then be related to the form-factor $f_{\boldsymbol{k}}(\boldsymbol{r})$ by using Eqn. (7).

The Optical Potential ($U_{op} = U_F + \Delta U$) is composed of real (U_F) and imaginary (ΔU) components, The real part of the Optical Potential $U_F = \int_0^\infty \rho(r')v(r,r')r'^2 dr'$ is calculated by single-folding of an effective interaction $v(r,r')$ over the density of the target nucleus $\rho(r')$, where r is the distance between the projectile and target nucleus and r' indicates the internal coordinates of the nucleons in the target nucleus. The imaginary part is represented by a Woods-Saxon shape, $\Delta U(r) = -\frac{W}{e^x+1}$, $x = \frac{r-R_W}{a_w}$. The potential parameters are obtained by fits to elastic scattering data. The nucleus studied is assumed to have a ground-state density of a Fermi shape, and the transition densities (Section 3.2) to the different multipoles are obtained by deformation of the ground-state density. The transition potential is dependent on the transition density. The transition potentials (Section 3.3) for the different multipoles are obtained by single-folding of an effective α-nucleon interaction (Section 3.4) over the target nucleus density. The optical potential used to calculate the incoming and outgoing wavefunctions is obtained using the ground-state density, and for the transition potentials, the transition

densities are used. The DWBA approximation is used to calculate the differential cross-section of the transition to each multipole (L=0-4). PTOLEMY [54] is used for obtaining the optical potential parameters and for calculating the differential cross-section of the isoscalar multipole transitions. SDOLFIN and DOLFIN [55] are used for calculating the incoming and outgoing transition potentials respectively.

The Energy Weighted Sum Rule (EWSR) is a sum of the transition possibilities from the ground state to excited states, multiplied by excitation energy [12]:

$$S(Q) \equiv \sum_{n} (E_n - E_0)|\langle n|Q|0\rangle|^2 = \frac{1}{2}\langle 0\big[Q,[H,Q]\big]0\rangle \qquad (8)$$

where n is the complete set of excited states due to operator Q on the ground state $|0\rangle$. Only a small fraction of the strength is found in low-lying excited states, with the bulk of the strength in the high-lying collective excitations (Giant Resonances).

3.2 Transition Densities

The transition densities can be obtained by a deformation of the phenomenological ground-state density which is assumed to have a Fermi shape, with parameters c and a obtained from scattering experiments:

$$\rho(r) = \frac{\rho_0}{1 + e^{\frac{r-c}{a}}} \qquad (9)$$

The Bohr-Mottleson form (10) for the density deformation

$$g_l^{BM}(r) = \frac{\delta_l^m d\rho(r)}{dr} \tag{10}$$

is used in the calculation for the excitation of low-lying vibrational states and has been found to be in agreement with microscopic transition densities when used for GR with $\ell \geq 2$ [56].

For the GMR, the transition density used is:

$$g_0(r) = -\alpha_0^m \left[3 + \rho(r) + r\frac{d\rho(r)}{dr}\right] \tag{11}$$

where α is a deformation parameter. RPA calculations tend to give a result for the GMR transition density which is similar in form to this [53].

The transition density for the isoscalar dipole is less straightforward. When using the above forms with $\ell = 1$, these forms of the transition density correspond to a small displacement of the center of mass without a change of shape, which is a spurious result. The form adopted here is derived by Harakeh and Dieperink [57]:

$$\rho(r) = -\frac{\beta_1}{R}\left[3r^2\frac{d}{dr} + 10r - \frac{5}{3}\langle r^2\rangle\frac{d}{dr} + \epsilon\left(r\frac{d^2}{dr^2} + 4\frac{d}{dr}\right)\right]\rho_0(r) \tag{12}$$

$$\beta_1^2 = \frac{6\pi\hbar^2}{mAE_x} R^2 (11\langle r^4\rangle - \frac{25}{3}\langle r^2\rangle^2 - 10\epsilon\langle r^2\rangle)$$
$$\epsilon = \frac{1}{3mA}\left(\frac{4}{E_2} + \frac{5}{E_0}\right)\hbar^2 \quad (13)$$

where R is the half-density radius of the Fermi mass distribution, and β_1 is the coupling collective parameter. This form of the isoscalar dipole excitation is for one magnetic substate only, and the cross-section should be multiplied by a factor of 3.

3.3 Transition Potentials

The assumption used when calculating scattering is that the elastic part is the main component and the inelastic scattering is a perturbation. The interaction is described as a direct reaction defined by a single event. The relative motion of the nuclei is described by distorted waves, which are the elastic scattering wave functions and would have the form of a plane-plus-scattered wave but are 'distorted' by the Coulomb field.

For incident particles with average momentum $\hbar\mathbf{k}$ on a scatterer represented by an effective interaction V(r), the Schrodinger equation is written as:

$$(\nabla^2 + k^2)\,\psi = \frac{2m}{\hbar^2} V\psi \quad (14)$$

The distorted wave $\psi_{\boldsymbol{k}}^{(+)}$, where (+) is used to designate this as the outgoing wave, in the asymptotic solution of (12) is:

$$\psi_{\boldsymbol{k}}^{(+)} \approx N(e^{i\boldsymbol{k}\cdot\boldsymbol{r}} + \frac{e^{ikr}}{r} f_{\boldsymbol{k}}(\boldsymbol{r})) \tag{15}$$

The differential cross-section is related to the coefficient $f_k(\hat{\boldsymbol{r}})$:

$$\frac{d\sigma}{d\Omega} = |f_k(\hat{\boldsymbol{r}})|^2 \tag{16}$$

Then, the scattering amplitude for elastic scattering in the direction of $\widehat{\boldsymbol{k}'}$ is given by:

$$f_{\boldsymbol{k}}(\widehat{\boldsymbol{k}'}) = -\frac{m}{2\pi\hbar^2 N} \int e^{-i\boldsymbol{k}\cdot\boldsymbol{r}} V(\boldsymbol{r}')\psi_{\boldsymbol{k}}^{(+)}(\boldsymbol{r}')d^3r \tag{17}$$

The first-order Born Approximation is to replace the exact solution for the outgoing wave $\psi_{\boldsymbol{k}}^{(+)}(\boldsymbol{r}')$ with the normalized plane wave term from the Green's Functions solution to the scattering problem:

$$f_{\boldsymbol{k}}(\widehat{\boldsymbol{k}'}) = -\frac{m}{2\pi\hbar^2 N} \int e^{-i\boldsymbol{k}'\cdot\boldsymbol{r}'} V(\boldsymbol{r}')e^{-\boldsymbol{k}'\cdot\boldsymbol{r}'} d^3r' \tag{18}$$

In the Optical Model for elastic and inelastic scattering, for the 2-body scattering of nuclei $\boldsymbol{a} + \boldsymbol{A}$, the interaction is averaged and made into radial form to produce a 1-body Schrodinger equation (19),

$$\left[-\frac{\hbar^2}{2\mu_\alpha}\nabla^2 + U(\boldsymbol{R})\right]\chi(\boldsymbol{R}) = E_\chi(\boldsymbol{R}) \tag{19}$$

with reduced mass μ_α, separation of centers of mass $\boldsymbol{R}$, and center of mass energy of relative motion E.

The wave function $\chi(\boldsymbol{R})$ can be expanded in terms of its internal eigenstates, for example:

$$\Psi_\alpha = \sum_{ij} \psi_{ai}\psi_{Aj}\chi_{ij}(\boldsymbol{R}) \tag{20}$$

where $\chi_{ij}(\boldsymbol{R})$ describes the relative motion of **a** and **A** and χ_{00} would give the elastic scattering.

The Optical Model of nuclear reactions from Feshbach's theory [58,59] uses a complex potential (21)

$$U_{op} = V_{00} + \lim_{\epsilon\to 0}\sum_{\alpha\alpha'} V_{0\alpha}\left(\frac{1}{E - H + i\epsilon}\right)_{\alpha\alpha'} V_{\alpha' 0} = U_F + \Delta U \tag{21}$$

to describe an effective nucleon-nucleon interaction.

V is the real interaction between two nuclei, and the index α refers to pairs of internal states in each nucleus where the prime is used to designate pairs of excited states. The real part is mostly in the V_{00} term and produces elastic scattering.

In the folding approach, the potential V_{00} is obtained by averaging the nucleon-nucleon interaction v_{ij} where i denotes nucleons in one nucleus and j denotes nucleons in other nucleus. This gives the effective interaction, $V = \sum_{i,j} v_{ij}$. The folded potential U_F is used to calculate the real potential V_{00} using Eq. (22).

$$U_F(R) = V_{00} \equiv (\psi_{a0}\psi_{A0}|V|\psi_{a0}\psi_{A0}) \tag{22}$$

In the approach used here, the effective interaction $v(r, r')$ (where r' describes the internal coordinates of the target nucleus) for the inelastic scattering has real and imaginary parts and is folded with the transition densities $\rho(r')$ described above for the different multipoles in order to obtain the transition potentials, U_F.

$$U_F(r) = \int_0^\infty \rho(r')v(r, r')r'^2 dr' \tag{23}$$

The ΔU term in Eq. (21) is complex and arises from couplings to the non-elastic channels α and α' and is used for describing transitions to open non-elastic channels.

3.4 Effective Interaction

Satchler and Khoa described the hybrid potential model and the effective interaction used here in Ref. [53]. Initially, the effective interaction used to represent the nucleon-

nucleon interaction averaged over the density distribution of the α particles was given by a Gaussian (24) with complex strength (G194, with $t = 1.94$ fm).

$$\overline{v_G}(s) = -(v + iw)e^{-\frac{s^2}{t^2}} \tag{24}$$

The strengths (*v* and *w*) are optimized to fit the elastic data. It is an effective interaction used primarily for <100 MeV α particles but has been found to reproduce the measured forward angle scattering at 240 MeV. The imaginary part was found to be too strong though, with too much absorption in the interior. Also, the strength *v* required to fit the diffractive scattering was found to be too large in the interior to reproduce the rainbow at large angles.

A hybrid approach was adopted where the real and complex parts have different radial shapes [53]. The imaginary part of the effective interaction is replaced with a phenomenological Woods-Saxon shape, with parameters R_W and a_w.

$$ImU(r) = -\frac{W}{e^x + 1},\ x = \frac{r - R_W}{a_w} \tag{25}$$

A correction to the strength *v* is made by making the interaction density dependent.

$$\begin{gathered}\overline{v_{DDG}}(s, \rho) = \overline{v_G}(s) f(\rho) \\ f(\rho) = 1 - \alpha\rho(r')^{\beta},\ \beta = \frac{2}{3}\end{gathered} \tag{26}$$

Lastly, a dynamic correction to the density dependence is applied to account for the change to the interaction $(v(\rho) \rightarrow v(\rho + \delta\rho))$ as a result of the density deformation $(\rho \rightarrow \rho + \delta\rho)$

$$v'(\rho) = v(\rho) + \frac{\rho \partial v(\rho)}{\partial \rho}$$
$$\alpha' = \alpha(1 + \beta) = \left(\frac{5}{3}\right)\alpha \tag{27}$$
$$f'(\rho) = 1 - \alpha(1 + \beta)\rho(r')^{\beta}$$

of the multipole transition. This correction reduces the strength in the interior as well.

To prove the validity of this approach, Satchler & Khoa [53] compared the results for elastic and inelastic scattering of 240 MeV α and ^{58}Ni with calculations using a single-folded potential with a density-dependent Gaussian (DDG) effective interaction, a double folded real potential with an M3Y-type N-N interaction, and a deformed potential model with a phenomenological Woods-Saxon potential. They found that the deformed potential approach was unreliable and that the single-folded DDG potential produced results in agreement with the double-folded N-N potential.

3.5 Fit to Experimental Data

A continuum of events consisting of various reactions such as multipole excitation, multistep excitation, pickup-breakup, and knock-out reactions as well as possibly some background from slit scattering is present in the data. In the analysis of the data, this continuum is represented by a straight line at high excitation joined to a Fermi shape at

low-excitation to model the particle decay threshold. The inelastic α spectra obtained at several angles are each divided into a peak and continuum. The peak and continuum cross-sections are then divided into bins by excitation energy in a manner similar to the illustration in Figure 13, which shows a slicing of the GR peak into 300 keV bins for further analysis.

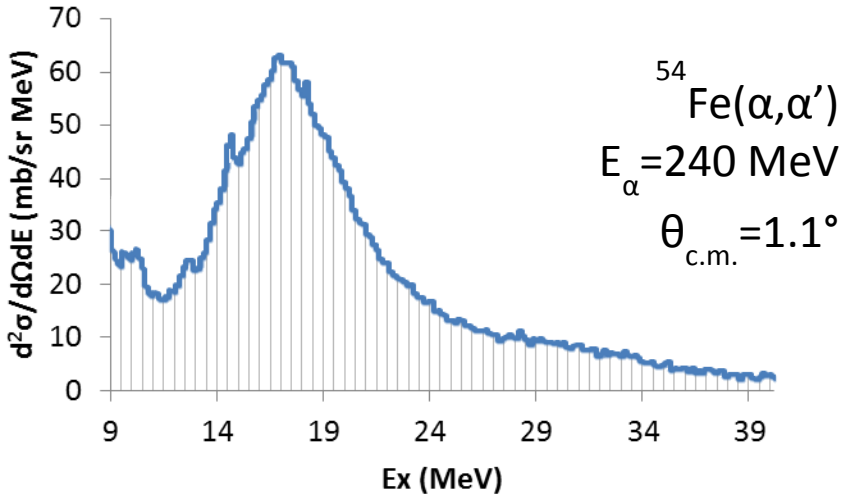

Figure 13. The Giant Resonance peak is "sliced" into 300 keV bins for identifying strength of the multipole excitations by comparison with PTOLEMY DWBA calculation of the multipole cross-sections.

Generally, the E0 (ISGMR) and E2 (ISGQR) strength distributions obtained have been found to be relatively insensitive to the continuum choice whereas the E1 (ISGDR) and E3 (ISGOR) strength distributions are sensitive to the choice of continuum. Thus several analyses are carried out using several different continuum choices. For example, the linear slope at high excitation may not quite match the data, the amplitude of the continua may be lowered so that it is always below the data, the low energy cutoff and

slope may be varied, or the continuum slope and/or amplitude could be altered at selected angles. A typical range of continuum choices is illustrated in Figure 14. The strength distributions obtained from these separate analyses are combined into a weighted average.

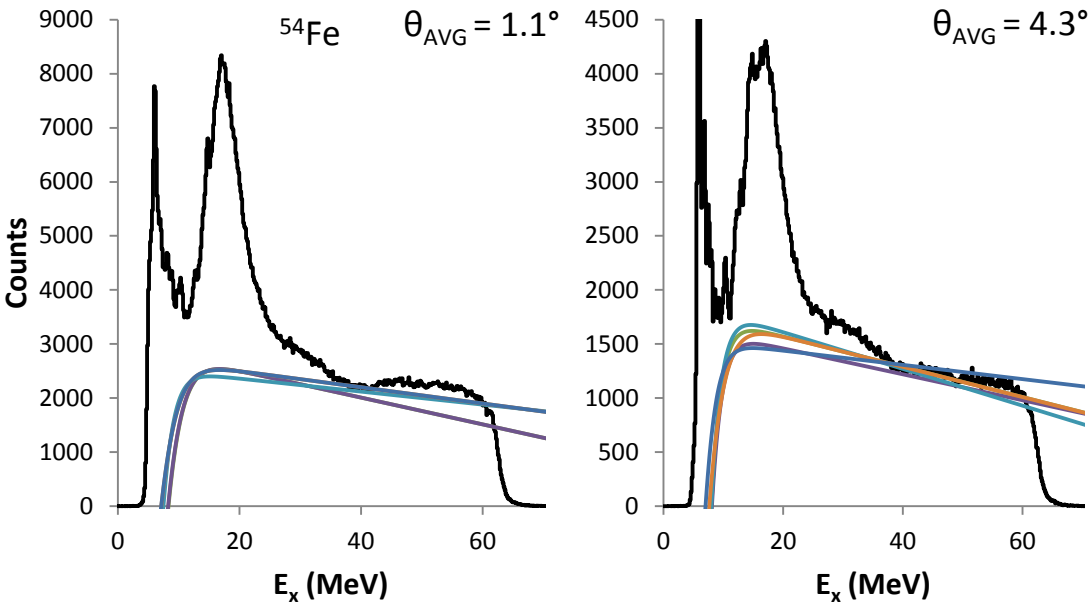

Figure 14. Example inelastic α spectra for ^{54}Fe are shown. The lines are examples of continua chosen for analyses.

The experimental angular distributions are then compared to the DWBA calculations, and the strengths of the isoscalar L=0-4 contributions are varied to minimize χ^2. The IVGDR contributions are calculated from the known distributions obtained from photoabsorption data [60] and held fixed in the fits. Uncertainty in the strength of a multipole is determined for each multipole fit by incrementing or decrementing the strength of that multipole and then adjusting the strengths of the other multipoles by

fitting to the data. This is continued iteratively until the new χ^2 is one unit larger than the original, best-fit total χ^2.

4 ISOSCALAR E0, E1, AND E2 STRENGTH IN ^{44}CA

4.1 Overview

Isoscalar giant resonances in ^{44}Ca have been studied with inelastic scattering of 240 MeV α particles at small angles including 0°. A majority of the Energy Weighted Sum Rule was identified for E0 and E2 (≈70%), and nearly half was identified for E1. The strength distributions are compared with the predictions from HF-RPA calculations with the KDE0v1 interaction.

4.2 Introduction

Giant Resonances (GR) are the broad resonances that occur at excitation energies between 10 and 30 MeV. They correspond to the collective motion of nucleons within the nucleus and have modes classified according to their multipolarity L, spin S, and isospin T quantum numbers. The Isoscalar Giant Monopole Resonance (ISGMR) is interesting because its excitation energy is directly related to the incompressibility of the nucleus K_A (28), where $\langle r^2 \rangle$ is the mean square radius and *m* is the mass of the nucleus [13,14].

$$E_{GMR} = \sqrt{\left(\frac{\hbar^2 K_A}{m\langle r^2 \rangle}\right)} \tag{28}$$

K_A can be used to obtain the incompressibility of nuclear matter K_{NM} by comparison to calculations using mean fields, where the value for K_{NM} is deduced from the interaction that best reproduces the experimental data on the strength functions of the giant resonance. At present, the best value for K_{NM} is 220-240 MeV [24].

The isoscalar E0-E3 giant resonances for ^{48}Ca were investigated by Lui *et al*. [29], and the isoscalar E0-E3 giant resonances in ^{40}Ca were investigated by Youngblood *et al*. [37]. E0 strength for both Ca isotopes were compared with Hartree-Fock Random Phase Approximation (HF-RPA) calculations in Ref. [29]. In the mass region $20 \leq A \leq 65$, the centroid energy (m_1/m_0) follows a systematic trend $\approx 36A^{-1/6}$. ^{40}Ca is in agreement with this systematic trend, and ^{48}Ca has an energy higher than the systematic trend by approximately 1 MeV. By studying ^{44}Ca we may be able to learn more about this issue.

In contrast, HF-RPA calculations of the centroid energy for different Skyrme interactions were higher than the experimental data for ^{40}Ca and were also higher but closer to agreement with the data for ^{48}Ca [29].

In this paper we report E0, E1, and E2 multipole strength distributions obtained for ^{44}Ca and compare the experimental distributions with those obtained for ^{40}Ca and ^{48}Ca and with theoretical predictions from the results of HF-RPA calculations with the KDE0v1 interaction.

4.3 Experimental Procedure

The experimental technique has been described thoroughly in Refs. [37,61] and is summarized briefly below. Beams of 240 MeV α particles from the Texas A&M K500 super-conducting cyclotron bombarded a self-supporting ^{44}Ca foil of 5.0 mg/cm^2 enriched to more than 95% in the desired isotope, located in the target chamber of the multipole-dipole-multipole spectrometer. The horizontal and vertical acceptance of the spectrometer was 4°. Ray tracing was used to reconstruct the scattering angle. The vertical acceptance was ±2°. The focal plane detector measured position and angle in the scattering plane, covering $E_x \approx$ 8 MeV to $E_x >$ 55 MeV (depending on scattering angle). The out-of-plane scattering angle was not measured. Position resolution of approximately 0.9 mm and scattering angle resolution of about 0.09° were obtained. Cross sections were obtained from the charge collected, target thickness, dead time, and known solid angle. The target thicknesses were measured by weighing and checked by measuring the energy loss of the 240 MeV α beam in each target. The cumulative uncertainties in target thickness, solid angle, etc, result in about a ±10% uncertainty in absolute cross sections. ^{24}Mg spectra were taken before and after each run and the 13.85±.02 MeV L=0 state [62] was used as a check on the calibration in the giant resonance region.

Data were taken with the spectrometer at 0.0° (0.0° < θ < 2.0°) and at 4.0° (2.0° < θ < 6.0°). Sample spectra obtained for ^{44}Ca are shown in Figure 15.

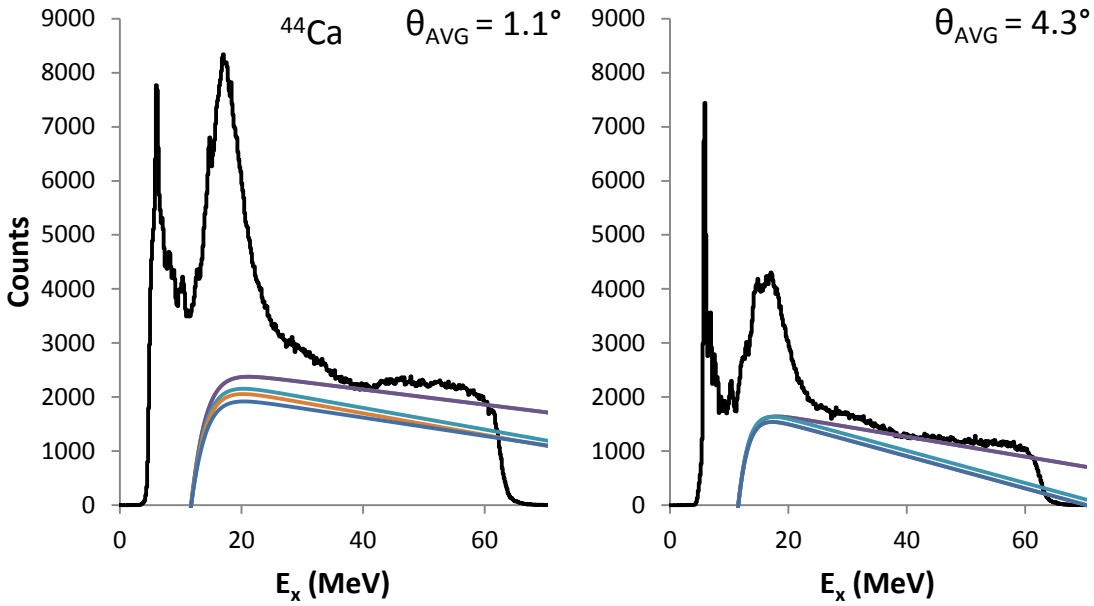

Figure 15. Inelastic α spectra obtained for ^{44}Ca are shown. The lines are examples of continua chosen for analyses.

4.4 Multipole Analysis

Single-folding DWBA calculations with optical model potentials (as described in Refs. [37,53,61]) were carried out with PTOLEMY [54]. Optical model parameters obtained for 240 MeV α scattering on ^{48}Ca [29] were used and are shown in Table II.

Table II. Optical Model and Fermi parameters used in DWBA calculations are listed, r_{c_0} is the Coulomb radius parameter.

V (MeV)	W (MeV)	r_i (fm)	a_i (fm)	r_{c_0}	c	a
47.392	31.495	0.959	0.677	.960	5.0264	.523

Calculations were performed with the Fermi form for the mass distribution, $\rho(r) = \rho_0 \left[1 + e^{\frac{r-c}{a}}\right]^{-1}$, with c and a shown in Table II [63]. This choice for the ground state density was guided by analysis of high-energy proton scattering and the results of Hartree-Fock calculations and shell-model calculations [64,65]. The calculations for the transition densities, sum rules, and DWBA calculations were discussed thoroughly in Refs. [37,53,61,66].

The peak and continuum cross-sections are then divided into bins by excitation energy. To obtain the multipole components for each experimental bin, the experimental angular distributions of the peak and continuum cross-sections are compared to the single-folding DWBA calculations done with PTOLEMY, and then the strengths of the isoscalar L=0-4 contributions are varied in order to minimize χ^2. The IVGDR contributions are calculated and held fixed in the fits. The experimental and calculated angular distributions are illustrated in Figure 16 for selected energy bins in the GR peak. The uncertainty for each multipole is determined by incrementing or decrementing the strength of that multipole, adjusting the strengths of other multipoles by fitting to the data, and continuing until the new χ^2 is 1 unit larger than the χ^2 from the best fit.

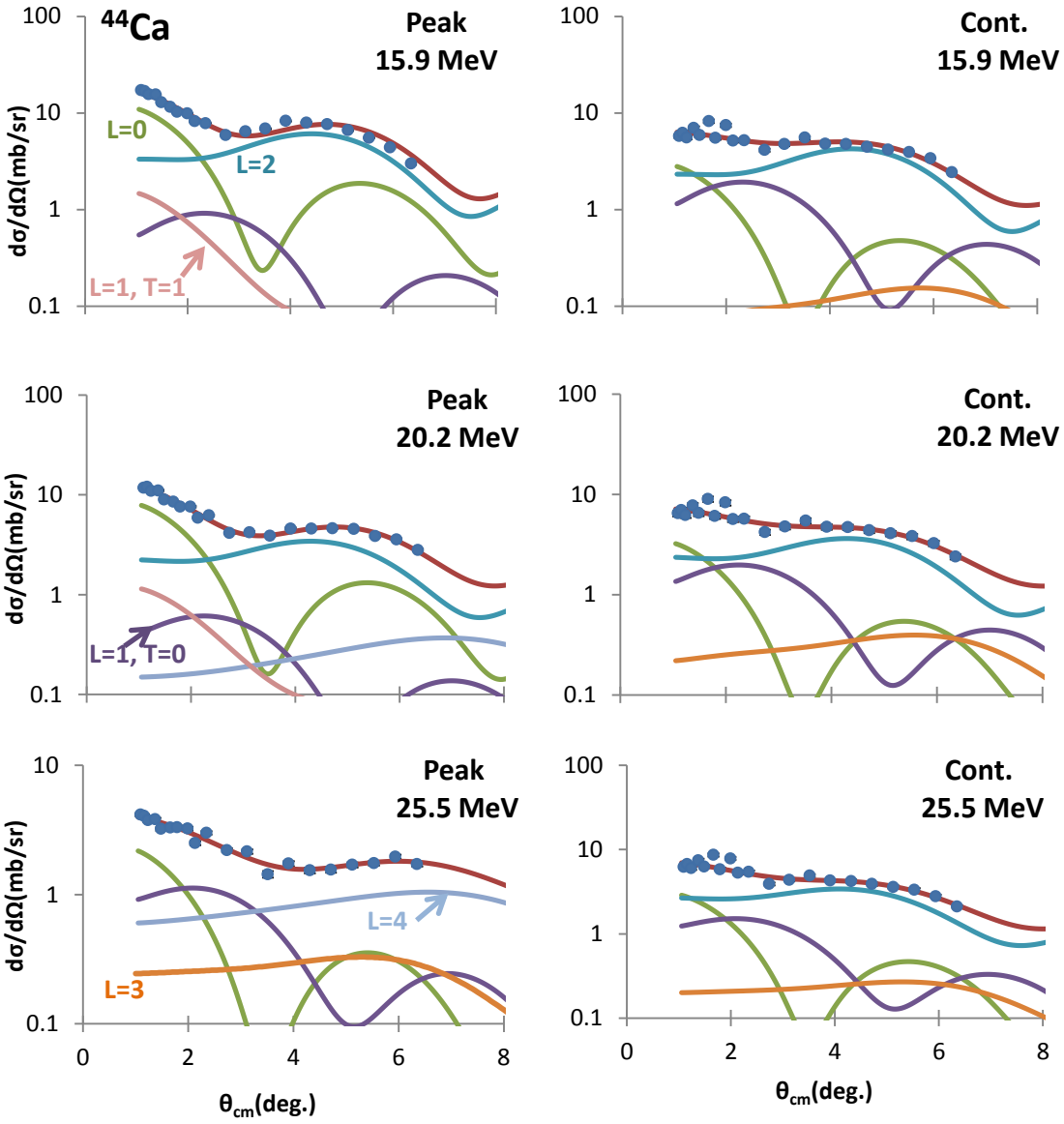

Figure 16. The angular distributions of the ^{44}Ca cross sections for three excitation ranges of the GR peak and the continuum are plotted vs. center-of-mass scattering angle. Each bin is 480 keV wide and the average energies for each bin are shown. The lines through the data points indicate the multipole fits. The contributions of each multipole are shown. The statistical errors are smaller than the data points.

Analyses are done several times using different assumptions about the continuum in order to estimate the uncertainties due to the choice of continuum. Typical choices for

the continuum can be seen in Figure 15. For purposes of estimating the uncertainties, the continuum could have a linear slope at high excitation that does not quite match the experimental data, could be lowered so that it is always below the data, could have a different low energy cutoff and slope, or could have slope and or amplitude which is altered at selected angles.

These separate analyses are then combined into an average distribution. Errors were calculated by adding the errors from the multipole fits in quadrature with the standard deviations between the different fits.

4.5 Description of Microscopic Calculations

Microscopic mean-field based Random Phase Approximation (RPA) theory provides a description of collective states in nuclei [12,24]. A description of the spherical HF-based RPA calculations of the strength functions and centroid energies of the isoscalar (T=0) giant resonances in nuclei can be found in Ref. [67] and is summarized below.

The strength or response function can be obtained from the RPA states $|n\rangle$ with corresponding energy E_n:

$$S(E) = \sum_n |\langle 0|F|n\rangle^2|\delta(E - E_n) \tag{29}$$

where F is the single particle scattering operator $F = \sum f(i)$. The ISGMR energies ($m_k = \int E^k S(E) dE$) are given by:

$$E_{con} = \sqrt{\frac{m_1}{m_{-1}}} \qquad E_{cen} = \frac{m_1}{m_0} \qquad E_{scal} = \sqrt{\frac{m_3}{m_1}} \qquad (30)$$

where, E_{con} is the constrained energy, E_{cen} is the centroid energy, and E_{scal} is the scaling model energy. The Energy Weighted Sum Rule (EWSR), m_1, is calculated using the Hartree-Fock ground state wave function.

The fully self-consistent mean field calculation of the response function uses an effective two-nucleon interaction V which is obtained from a fit to the ground states properties of nuclei. The effective interaction determines the HF mean-field. The RPA calculation includes all of the components of the two-body interaction using a large configuration space and was done using the numerical approach of Refs. [68,69]. The calculations of the strength functions and centroid energies of the isoscalar (T=0) giant resonances in the nuclei were done using an occupation number approximation for the single particle orbits of open shell nuclei. For the single-particle scattering operator $F = \sum_i f(r_i)Y_{L0}$ we used $f(r) = r^2$ for the monopole (L=0) and $f(r) = r^3 - \frac{5}{3}\langle r^2 \rangle r$ was used for the dipole (L=1). The form of the dipole scattering operator takes into account the contribution from spurious states [70,71]. The KDE0v1 Skyrme-type effective interaction was used. The appropriate experimental excitation energy ranges were used: 9-40 MeV for the ISGMR and ISGQR, 9-20 MeV for the low-component of the ISGDR, 20-36 MeV for the high-component of the ISGDR. The calculated distributions are shown superimposed on the experimental results in Figure 17 . The smearing widths for the calculated distributions for the E0-E2 multipoles are shown in Table III. The energy moments are

included in Tables IV and VI. The theoretical strengths are calculated over a range of 0 to 100 MeV and contain 100% of the EWSR for E0, E1, and E2.

Table III. Smearing widths for the calculated distributions are shown.

	E0	E1	E2
Γ (MeV)	6.5	13.0	10.0

4.6 Discussion

The E0-E2 multipole distributions obtained for ^{44}Ca are shown in Figure 17. Two peak fits are shown for the E1 distribution, and a single Gaussian fit is shown for E2. The strength distributions obtained with the HF-RPA calculations described in the section above are superimposed on the E0, E1, and E2 experimental distributions. The parameters for the experimental distributions are shown in Table IV. The parameters for the Gaussian fits and for the moments of the calculated distributions are shown in Table V and Table VI respectively. Due to the limited angular range of the data, E3 and E4 strength could not be distinguished unambiguously. The highest multipole included in the fits is E4, and the E3 distribution shown in Figure 17 is the sum of all the multipoles $L \geq 3$. The theoretical energy moments and strengths in Table IV and Table VI are for the experimental energy ranges (E0: $9 \leq Ex \leq 40$ MeV , E1 low range: $9 \leq Ex \leq 20$ MeV, E1 high range: $20 \leq Ex \leq 40$ MeV, and E2: $9 \leq Ex \leq 40$ MeV)

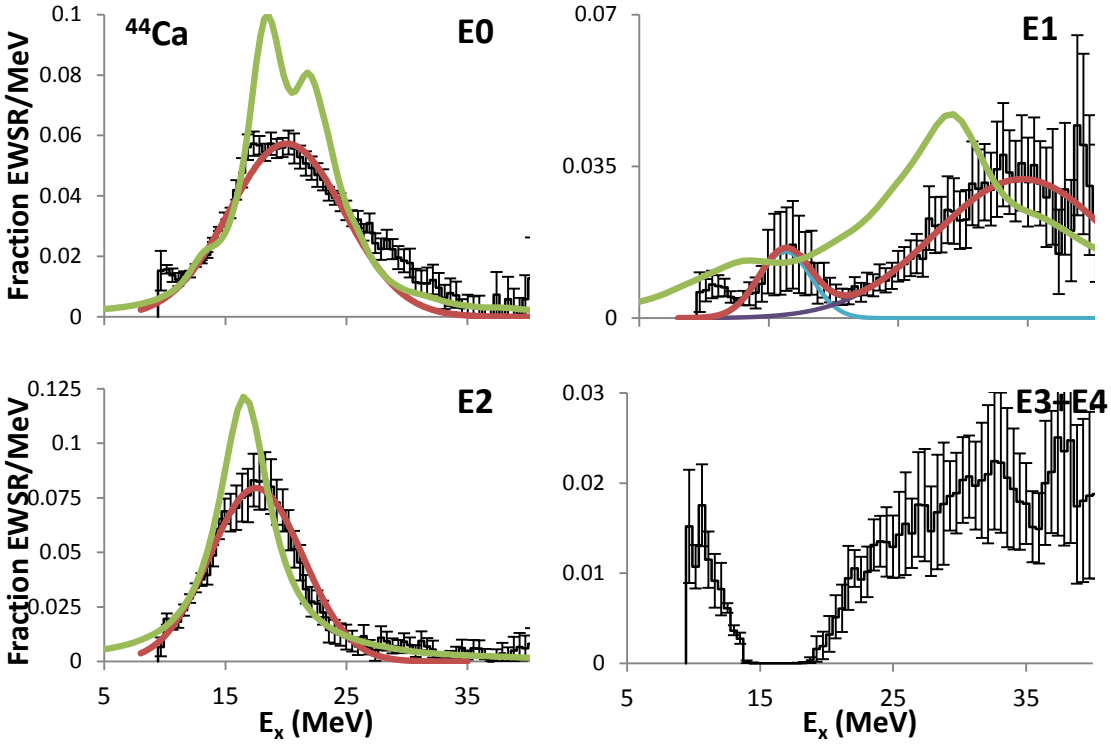

Figure 17. Strength distributions obtained for ^{44}Ca are shown by the histograms. Error bars represent the uncertainty based on the fitting of the angular distributions and different choices for the continuum, as described in the text. Gaussian fits to the E1 distributions for the individual peaks (blue and purple) and their sum (red) are shown. The green lines are the strength distributions obtained with the HF-RPA calculations using the KDE0v1 interaction, smeared to more closely represent the data as discussed in the text.

Table IV. Parameters for energy moments obtained for isoscalar multipoles in ^{44}Ca are listed. The moments from the KDE0v1 calculation results are over the experimental energy range 9≤Ex≤40 MeV.

	Moments			
	$E0$		$E1$	$E2$
	Exp.	KDE0v1		
m_1 (Frac. EWSR)	$0.75 \pm .11$	0.94	$0.48 \pm .19/.18$	$0.77 \pm .14$
m_1/m_0(MeV)	$19.50 \pm .35/.33$	19.55	$25.97 \pm 1.71/1.59$	$17.21 \pm .48$
rms width (MeV)	$5.84 \pm .86/.73$	5.01	$8.55 \pm 1.03/.84$	$5.06 \pm 1.28/1.15$
$\sqrt{m_3/m_1}$ (MeV)	$21.78 \pm .84/.72$	21.28	$30.11 \pm 2.09/1.84$	$19.01 \pm 1.02/.95$
$\sqrt{m_1/m_{-1}}$ (MeV)	$18.73 \pm .29$	18.97	$24.05 \pm 1.49/1.45$	$16.71 \pm .41$

Table V. Parameters obtained for Gaussian fits for isoscalar multipoles in ^{44}Ca are listed.

	Gaussian fits		
	$E1$ peak 1	$E1$ peak 2	$E2$
Centroids (MeV)	$16.46 \pm 1.39/1.55$	$34.92 \pm 1.57/1.34$	17.13±.11
FWHM (MeV)	$4.86 \pm 2.12/2.39$	$16.34 \pm 2.26/2.31$	9.40±.14
Frac. EWSR	0.07	0.53	0.68

Table VI. Parameters obtained for energy moments from the KDE0v1 calculation are listed. The results are over the experimental energy ranges (E1 low range: 9≤Ex≤20 MeV, E1 high range: 20≤Ex≤40 MeV, and E2: 9≤Ex≤40 MeV)

	KDE0v1		
	$E1$ low range	$E1$ high range	E2
m_1/m_0 (MeV)	14.37	29.16	16.71
rms width (MeV)	3.42	5.01	4.89
m_1 (Frac. EWSR)	0.15	0.58	0.92

4.6.1 E0 Strength

In ^{44}Ca, 75% of the E0 EWSR was identified. The strength distribution is similar to those observed in the other nuclei of this mass region (40≤A≤90) [27,32]. The shape is asymmetric with a large tailing on the high energy side which extends to 35 MeV. The shape is similar to the E0 strength in ^{48}Ca. The tailing in other nuclei of this region typically extends to 30 MeV. The theoretical prediction for the strength distribution

appears to fit the rise of the peak on the low-energy side of the experimental distribution well and has two narrow components separated by about 4 MeV. There is some tailing to the higher energy theoretical component, and it is similar to the tailing seen in the experimental peak. The observed mass dependence and the theoretical predictions from the fully self-consistent calculations with KDE0v1 are shown in Figure 18. The theoretical predictions for the scaling energy $\left(\sqrt{\frac{m_3}{m_1}}\right)$, centroid energy $\left(\frac{m_1}{m_0}\right)$, and constrained energy $\left(\sqrt{\frac{m_1}{m_{-1}}}\right)$ are all in good agreement with the experimental energies for ^{44}Ca.

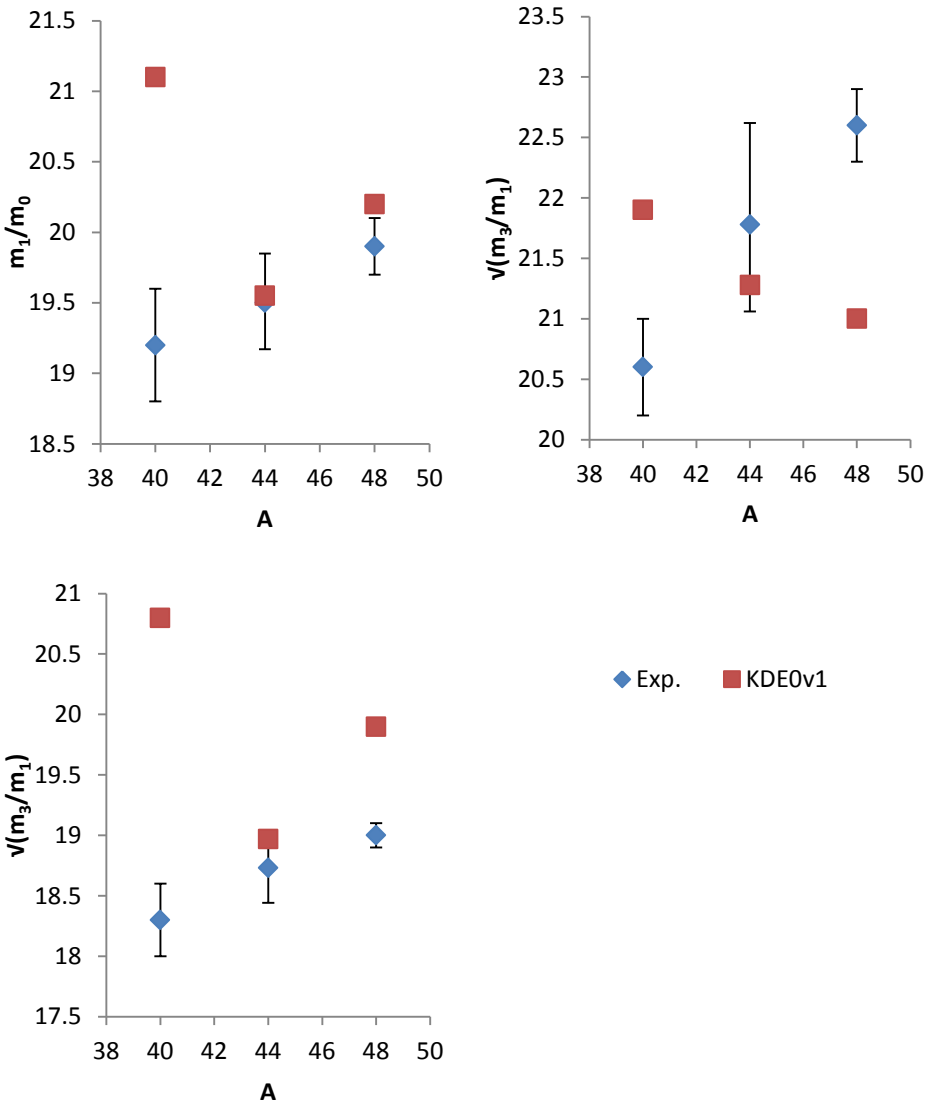

Figure 18. Experimental results for ISGMR energies in ^{40}Ca [37], ^{44}Ca (present work), and ^{48}Ca [29] (blue diamonds) are compared with theoretical predictions. The results of fully self-consistent HF-RPA calculations [30] with KDE0v1 [72] are shown using the experimental excitation energy range (E=9.5-40 MeV) (red squares).

4.6.2 E1 Strength

In ^{44}Ca $48\pm^{19}_{18}$% of the E1 strength was identified. This is much less than the E1 strength ($137 \pm 20\%$) identified for ^{48}Ca [29] but is similar to the amount identified in ^{40}Ca ($62\pm^{10}_{20}$%) [37]. The strength is distributed in low and high energy components. The E1 strength is particularly sensitive to the choice of continuum because of the low ratio of peak-to-continuum at the higher end of the energy range where the majority of the E1 strength is found. This sensitivity has been observed in ^{48}Ca, ^{40}Ca and in other nuclei. [27,32]. For ^{40}Ca, changes in the continuum choice resulted in shifts of m_1/m_0 of up to 2.5 MeV and sum-rule variation from 28-94%. The centroid energy m_1/m_0 for ^{40}Ca is 23.36±0.70 MeV, which is about 3 MeV less than the energy observed in ^{44}Ca. The low peak component observed in ^{44}Ca is narrow and is fit with a Gaussian with centroid energy of $16.51\pm^{.78}_{.74}$ MeV. It contains about 6% of the E1 strength. The high peak is much broader, has a centroid energy of $35.37\pm^{.67}_{.56}$ MeV, and contains 53% of the strength. Much more strength was identified in ^{48}Ca, but it has a similar ≈1:8 ratio in the strength found in the low peak to that found in the high peak. The energy of the low component is in agreement with that found for ^{48}Ca ($16.69\pm^{.39}_{.33}$ MeV). The energy of the high components of the E1 strength in both nuclei ($37.28\pm^{.71}_{1.98}$ MeV for ^{48}Ca) are also in agreement within experimental error. The E1 strength that results from the HF-RPA calculation with KDE0v1 interaction does not fit the experimental distribution well, and it has several components. The majority of the strength is in a peak located at 29.16 MeV, which is lower than the experimental high energy component by ≈7 MeV. The

majority of the strength in the low energy range ($9 \leq E_x \leq 20$ MeV) appears in a broad peak located at ≈13 MeV, and the centroid was calculated to be a bit higher in energy at 14.37 MeV which is ≈2 MeV less than the experimental centroid.

4.6.3 E2 Strength

A majority of the E2 strength ($71 \pm 4\%$) was identified in the experimental data. The theoretical prediction of the E2 strength over the range 9 to 40 MeV shows approximately 20% more strength than the experimental distribution. The predicted strength is in a single peak with a centroid of 16.71 MeV, which is in near agreement of the experimental centroid ($17.21 \pm .48$ MeV). The E2 strength in ^{48}Ca was roughly Gaussian with the exception of some strength found in a tail extending to 35 MeV. The ^{44}Ca centroid is also nearly in agreement with that for ^{40}Ca (17.84±0.43 MeV).

4.7 Summary

Close to 70% of the E0 and E2 strength was identified, and nearly half of the E1 strength have been located between 9 and 40 MeV in ^{44}Ca. The E1 strength distribution obtained for the GR peak was sensitive to the continuum choice. The E0 distribution is asymmetric with a tail at higher excitation that is similar to that found in ^{48}Ca. Yet, the centroid energy (m_1/m_0) in ^{44}Ca was found to be in agreement with the $36/A^{1/6}$ trend observed for most nuclei between ^{24}Mg and ^{60}Ni. The microscopic calculation with

KDE0v1 interaction does not reproduce the experimental strength distributions, but predicts energies for E0 that are in good agreement with the experimental values. It may be interesting to extend the calculations beyond RPA to include coupling to more complex configurations. The analysis done with collective-model based transition densities in the DWBA calculation may result in overestimation of the EWSR and shifts of the centroid energy [73], so it may be interesting to do the analysis with microscopic transition densities instead.

5 ISOSCALAR GIANT RESONANCES IN ^{54}FE, ^{64}ZN, AND ^{68}ZN

5.1 Overview

The giant resonance region from 10 MeV < E_x < 62 MeV in ^{54}Fe, ^{64}Zn, and ^{68}Zn has been studied with inelastic scattering of 240 MeV α particles at small angles, including 0°. Between 70 and 105% of the expected isoscalar E0 strength has been identified below E_x = 40 MeV for each of the nuclei. Between 70 and 104% of the E1 strength has been identified while 60% of E2 strength in ^{54}Fe and ^{68}Zn and 120% of the strength in ^{64}Zn have been identified. The strength distributions for ^{54}Fe and ^{68}Zn are compared with the predictions from HF-RPA calculations with the KDE0v1 interaction.

5.2 Introduction

Giant Resonances (GR) are the broad resonances that occur at excitation energies between 10 and 30 MeV. They correspond to the collective motion of nucleons within the nucleus and have modes classified according to their multipolarity L, spin S, and isospin T quantum numbers. The Isoscalar Giant Monopole Resonance (ISGMR) is interesting because its excitation energy is directly related to the incompressibility of the nucleus K_A (28), where $\langle r^2 \rangle$ is the mean square radius and *m* is the mass of the nucleon [13,14].

$$E_{GMR} = \sqrt{(\frac{\hbar^2 K_A}{m\langle r^2 \rangle})} \quad (31)$$

The value of K_{NM}, the incompressibility of nuclear matter, is deduced from the interaction used in mean field calculations which best reproduces the experimental values of E_{GMR} or K_A or best reproduces the E0 strength functions. At present, the best value for K_{NM} is 220-240 MeV [24].

The E0 strength distributions have shapes which have been found to vary with A, and further measurements in the mid-mass range $40 \leq A \leq 90$ are necessary to help explain the observed trends. Measurement of the GMR in ^{64,68}Zn is particularly useful because of the gap in measurements in the region $60 \leq A \leq 90$. Measurement of ^{54}Fe could be useful to study because it is between ^{48}Ca and ^{58}Ni in mass, and these nuclei have been found to have values for m_1/m_0 above the systematic trend ($36/A^{1/6}$) of the experimental data. In heavy nuclei ($A \geq 110$), the strength distribution of the GMR has a symmetric, Gaussian shape [31]. In the $A \approx 90$ region, the strength distribution consists of a high and low-energy component separated by 7-9 MeV [28]. The observed high-energy component remains unexplained. In nuclei with $A \leq 28$, the GMR becomes fragmented [27]. A number of nuclei have already been studied in the mass range A = 40 to 90, and the m_1/m_0 centroid energies for these nuclei are shown in Figure 19 [27,29,32]. In this mass region, the shape of the strength distribution changes to mostly Gaussian on the low-excitation side with a tail on the high-excitation side of the GMR [27,29,32,74]. This tailing has been predicted by microscopic calculations for ^{58}Ni [33,34], and has been

observed in the E0 strength distributions shown in Figure 20 for ^{46,48}Ti [32], ^{56}Fe, ^{58}Ni, ^{60}Ni [27], and ^{48}Ca [29]. ^{48}Ca shows large tailing on the high excitation side which extends to 40 MeV, whereas the other nuclei in Figure 20 have strength which extends to 35 MeV. Microscopic calculations of the E0 strength distribution by Kamerdzhiev [33,34] were in very good agreement with the experimental distribution for ^{40}Ca but not for ^{48}Ca. A similar calculation by Hamamoto [35] for ^{40}Ca was in poor agreement with the experimental distribution [29].

Measurement of the isoscalar E0, E1, and E2 strength distributions and moments for ^{54}Fe, ^{64}Zn, and ^{68}Zn were obtained. The E0, E1, and E2 distributions and moments for ^{54}Fe and ^{68}Zn were compared with results calculated by Hartree-Fock Random Phase Approximation (HF-RPA) with KDE0v1 interaction. The experimentally obtained moments for ^{54}Fe, ^{64}Zn, and ^{68}Zn were compared to calculations of the monopole energy based on Leptodermous expansion parameterizations by Chossy and Stocker [75] and by Nayak [15] of the results from HF-RPA and RMF calculations using Skyrme and Skyrme-like interactions.

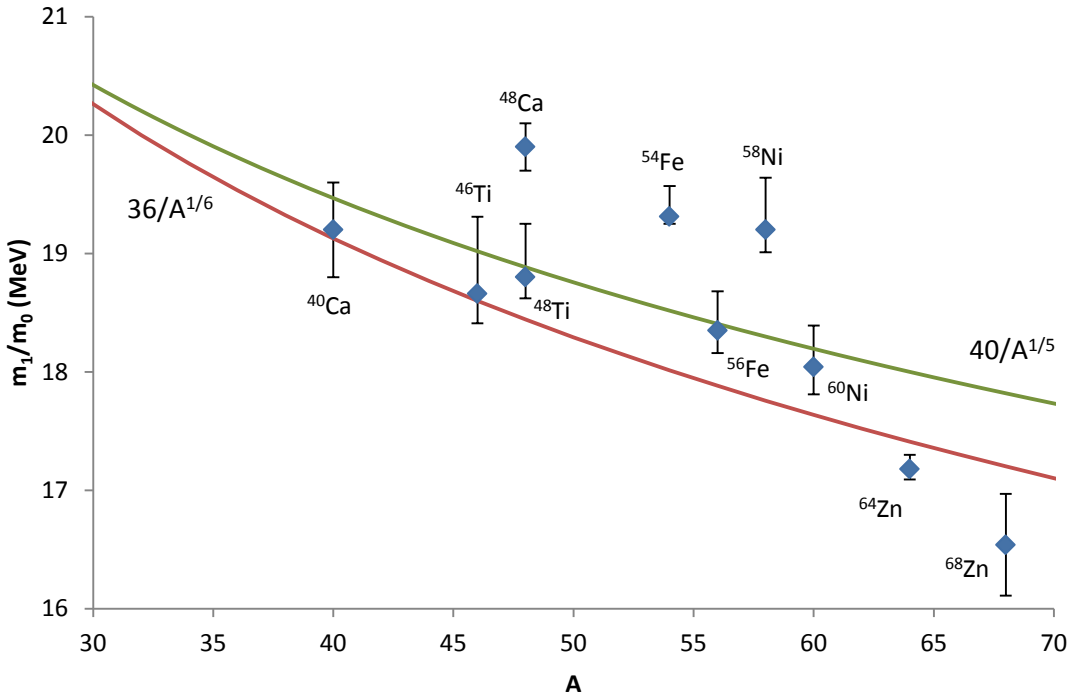

Figure 19. Centroid energies (m_1/m_0) for the ISGMR are plotted as a function of A. Lines representing $36/A^{1/6}$ and $40/A^{1/5}$ show the approximate systematic trend. The nuclei studied are ^{40,48}Ca [29]; ^{46,48}Ti [32]; ^{56}Fe and ^{58,60}Ni [27].

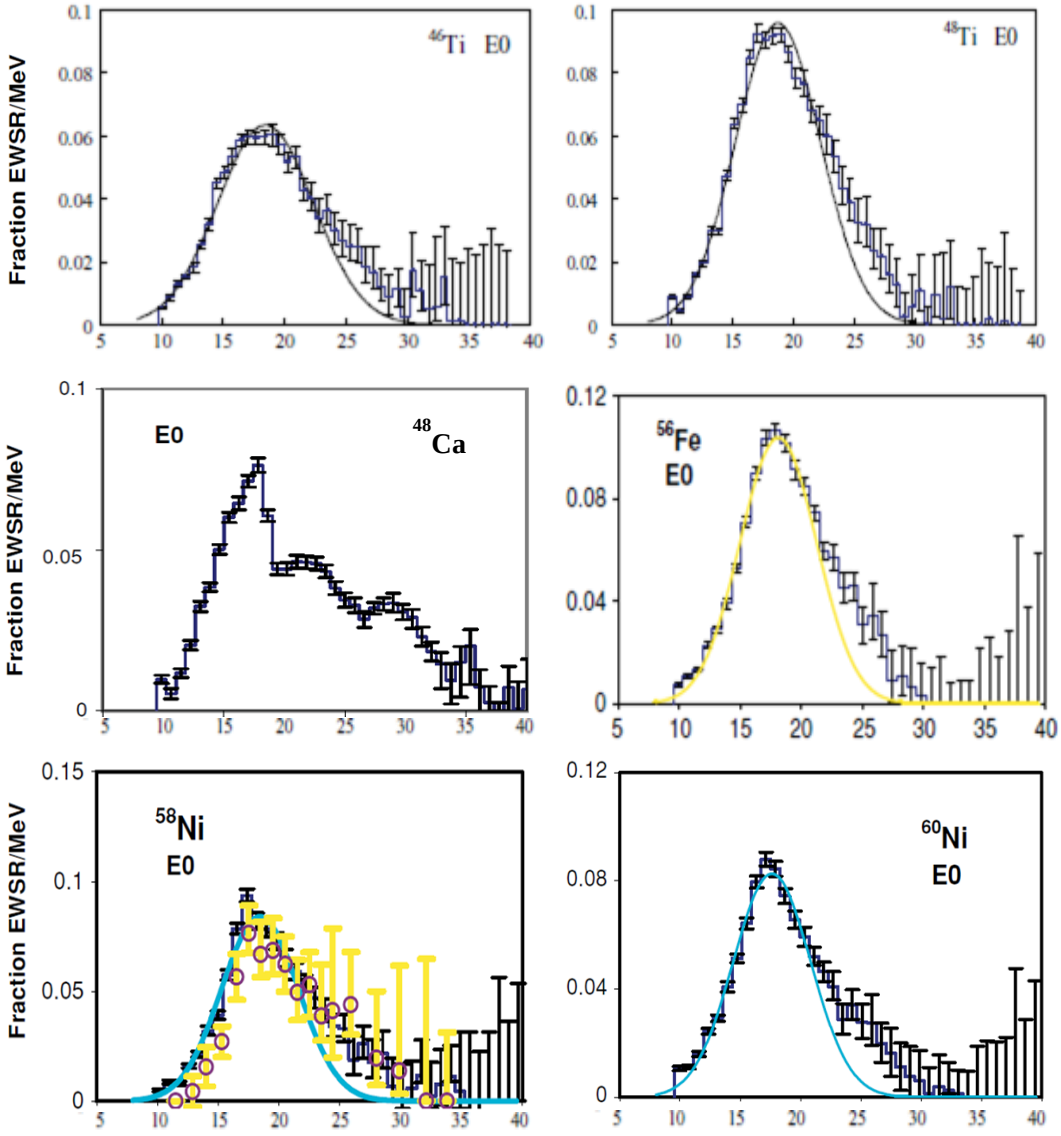

Figure 20. GMR strength distributions for ^{46,48}Ti, ^{48}Ca, ^{56}Fe, ^{58}Ni, and ^{60}Ni are shown by the histograms. Each shows an asymmetric distribution, with a tail on the high side of the excitation energy, compared to a Gaussian shape (smooth, solid line in each except for the case of ^{48}Ca) [29]. In the ^{58}Ni E0 strength distribution, the open circles indicate the strength distribution from Ref. [76] and dark blue histogram indicates the strength distribution from Ref. [27]

5.3 Experimental Procedure

The experimental technique has been described thoroughly in Refs. [37,61] and is summarized briefly below. Beams of 240 MeV α particles from the Texas A&M K500 super-conducting cyclotron bombarded self-supporting foils of ^{54}Fe (5.0 mg/cm^2), ^{64}Zn (6.4 mg/cm^2), and ^{68}Zn (4.9 mg/cm^2), enriched to more than 95% in the desired isotope, located in the target chamber of the multipole-dipole-multipole spectrometer. The horizontal and vertical acceptance of the spectrometer was 4°. Ray tracing was used to reconstruct the scattering angle. The focal plane detector measured position and angle in the scattering plane, covering $E_x \approx$ 8 MeV to E_x > 55 MeV (depending on scattering angle). The out-of-plane scattering angle was not measured. Position resolution of approximately 0.9 mm and scattering angle resolution of about 0.09° were obtained. Cross sections were obtained from the charge collected, target thickness, dead time, and known solid angle. The target thicknesses were measured by weighing and checked by measuring the energy loss of the 240 MeV α beam in each target. The cumulative uncertainties in target thickness, solid angle, etc, result in about a ±10% uncertainty in absolute cross sections. ^{24}Mg spectra were taken before and after each run with each target and the 13.85±.02 MeV L=0 state [62] was used as a check on the calibration in the giant resonance region.

Data were taken with the spectrometer at 0.0° (0.0° < θ < 2.0°) and at 4.0° (2.0° < θ < 6.0°). Sample spectra obtained for ^{54}Fe, ^{64}Zn, and ^{68}Zn are shown in Figures 21-23. The

cross-section is divided into peak and continuum, where the continuum is modeled as a straight line at high excitation joined to a Fermi shape at low-excitation (a representation of particle threshold) (Figure 23).

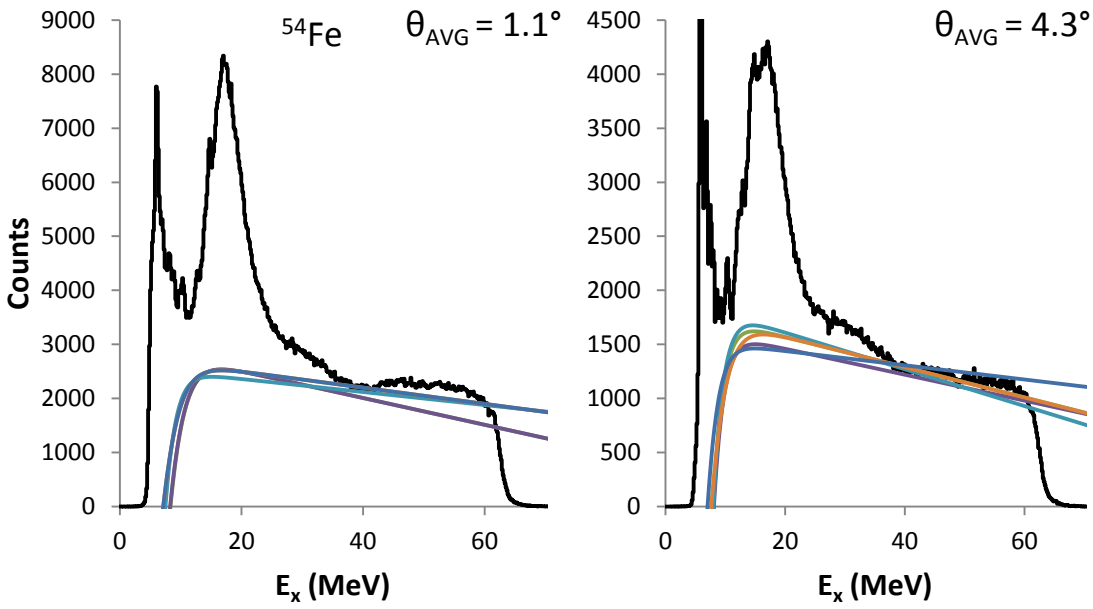

Figure 21. Inelastic α spectra obtained for ^{54}Fe are plotted vs. excitation energy. The lines are examples of continua chosen for analyses.

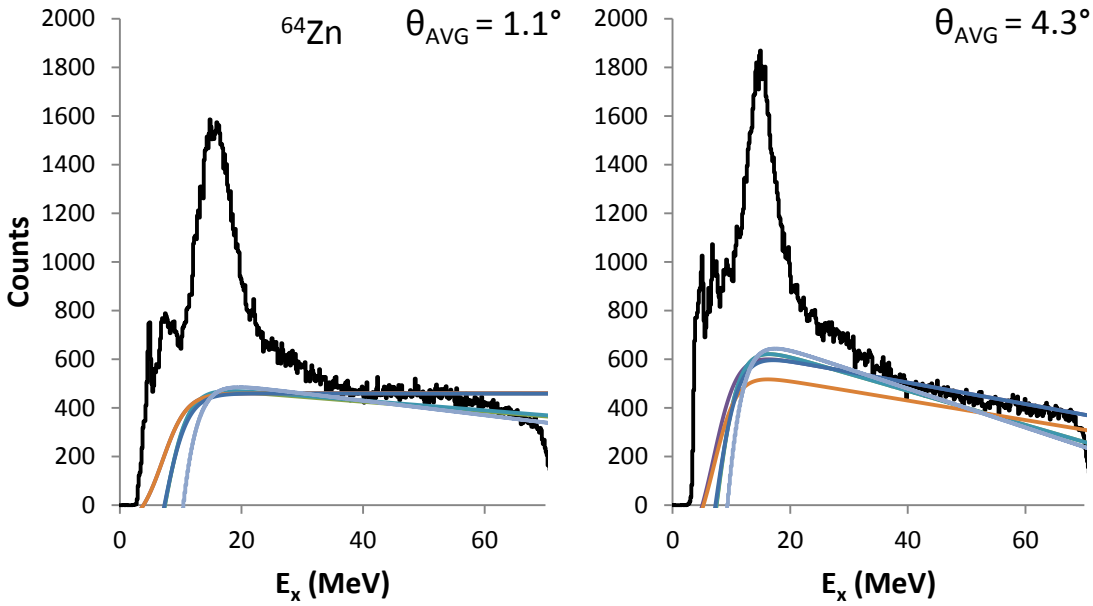

Figure 22. Inelastic α spectra obtained for ^{64}Zn are plotted vs. excitation energy. The lines are examples of continua chosen for analyses.

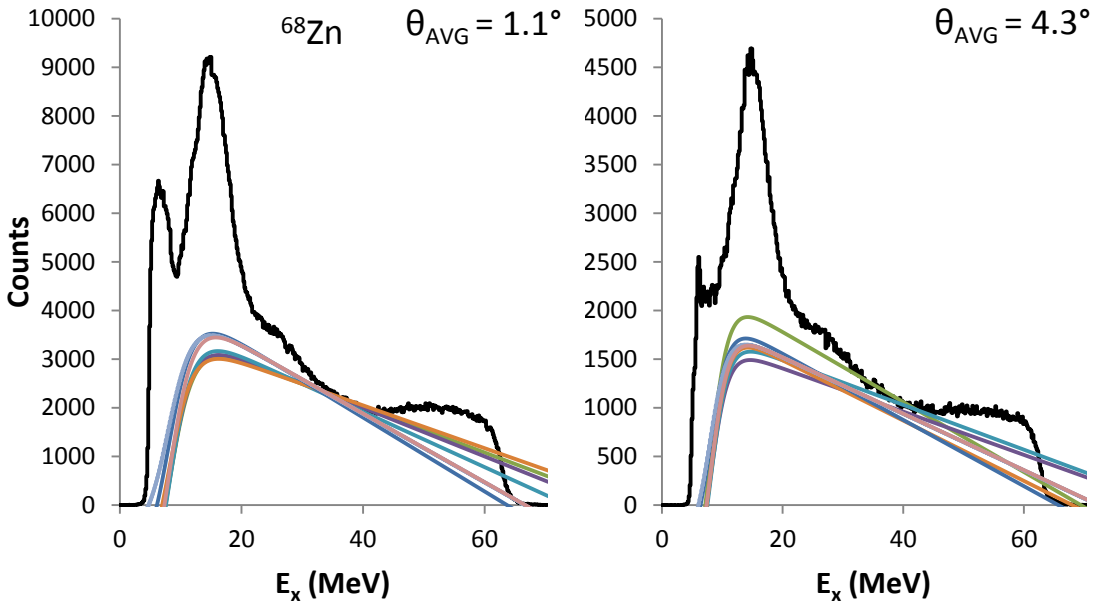

Figure 23. Inelastic α spectra obtained for ^{68}Zn are plotted vs. excitation energies. The lines are examples of continua chosen for analyses.

5.4 Multipole Analysis

Single-folding DWBA calculations (as described in Refs. [37,53,61]) are carried out with PTOLEMY [54]. Generally the Optical Model Potential parameters are obtained by PTOLEMY fits to elastic scattering data. Elastic scattering data were not taken for the nuclei studied here, and instead the parameters obtained for ^{58}Ni were used (Table VII) [27].

Table VII. Optical parameters used in the DWBA calculations are shown. r_p and r_t are the Coulomb radius parameters for the projectile and target, respectively.

V (MeV)	W (MeV)	r_i (fm)	a_i (fm)	r_p	r_t
41.19	40.39	0.821	0.974	1.336	1.256

Calculations were performed with Fermi mass distributions, $\rho(r) = \rho_0 \left[1 + e^{\frac{r-c}{a}}\right]^{-1}$, with c = 4.0546 fm for ^{54}Fe, c = 4.405 fm for ^{64}Zn, and c = 4.4597 fm for ^{68}Zn and with a = .523 fm for all three nuclei [63]. The calculations for the transition densities, sum rules, and DWBA calculations were discussed thoroughly in Refs. [37,53,61,66].

The peak and continuum cross-sections are then divided into bins by excitation energy in a manner similar to the illustration in Figure 24. To obtain the multipole components for each experimental bin, the experimental angular distributions of the peak and continuum cross-sections are compared to the single-folding DWBA calculations done with

PTOLEMY, and then the strengths of the isoscalar L=0-4 contributions are varied in order to minimize χ^2. The IVGDR contributions are calculated and held fixed in the fits. This procedure is illustrated in Figures 25 and 26 for the ^{54}Fe and ^{68}Zn nuclei respectively for selected energy bins in the GR peak. The uncertainty for each multipole is determined by incrementing or decrementing the strength of that multipole, adjusting the strengths of other multipoles by fitting to the data, and continuing until the new χ^2 is 1 unit larger than the χ^2 from the best fit.

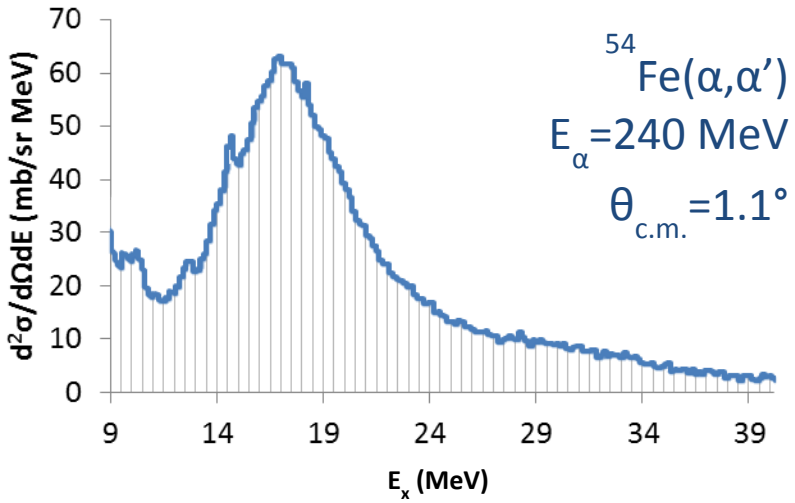

Figure 24. The Giant Resonance peak is "sliced" into 300 keV bins for multipole decomposition analysis.

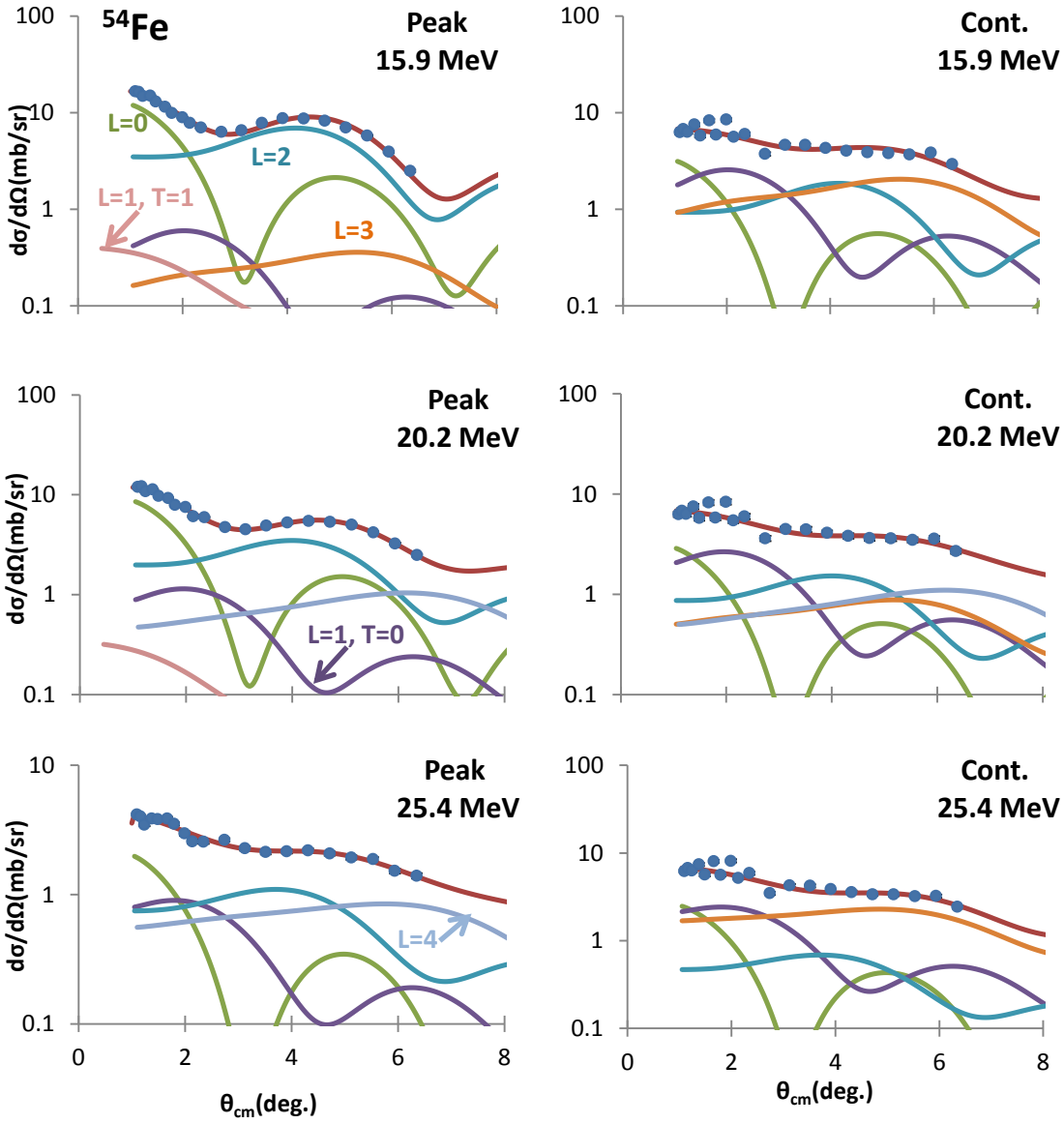

Figure 25. The angular distributions of the ^{54}Fe cross sections for three excitation ranges of the GR peak and the continuum are plotted vs. center-of-mass scattering angle. Each bin is 472 keV wide and the average energies for each bin are shown. The lines through the data points indicate the multipole fits. The contributions of each multipole are shown. The statistical errors are smaller than the data points.

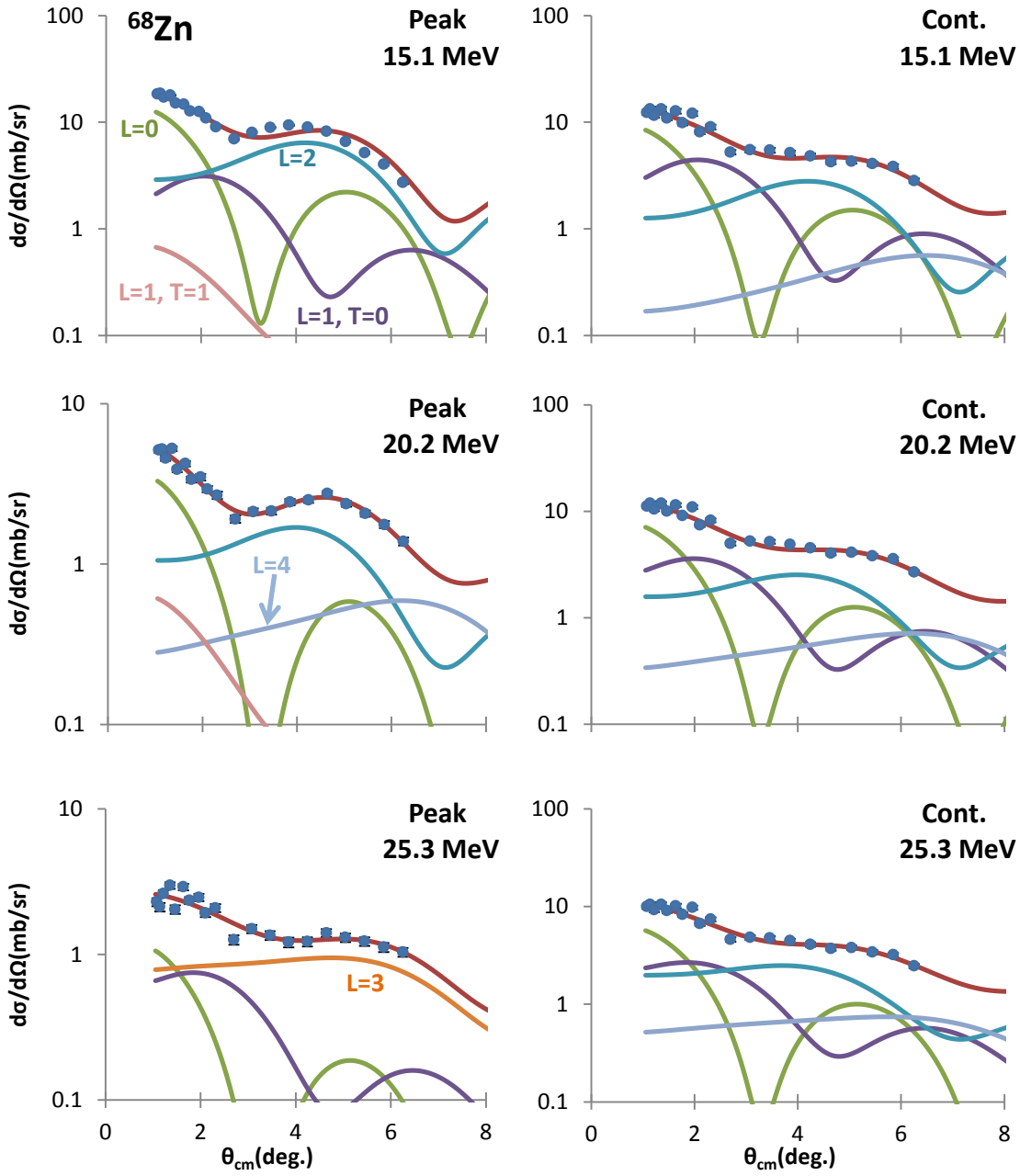

Figure 26. The angular distributions of the ^{68}Zn cross sections for three excitation ranges of the GR peak and the continuum are plotted vs. center-of-mass scattering angle. Each bin is 316 keV wide and the average energies for each bin are shown. The lines through the data points indicate the multipole fits. The contributions of each multipole are shown. The statistical errors are smaller than the data points.

Analyses are done several times using different assumptions about the continuum in order to estimate the uncertainties due to the choice of continuum. Typical choices for the continuum can be seen in Figure 23. For purposes of estimating the uncertainties, the continuum could have a linear slope at high excitation that does not quite match the experimental data, could be lowered so that it is always below the data, could have a different low energy cutoff and slope, or can have slope and or amplitude which is altered at selected angles. These separate analyses are then combined into an average distribution. Errors were calculated by adding the errors from the multipole fits in quadrature with the standard deviations between the different fits.

5.5 Description of Microscopic Calculations

Microscopic mean-field based Random Phase Approximation (RPA) theory provides a description of collective states in nuclei [12,24]. A description of the spherical HF-based RPA calculations of the strength functions and centroid energies of the isoscalar (T=0) giant resonances in nuclei can be found in Ref. [67] and is summarized below.

The strength or response function can be obtained from the RPA states $|n\rangle$ with corresponding energy E_n:

$$S(E) = \sum_n |\langle 0|F|n\rangle^2|\delta(E - E_n) \tag{32}$$

where F is the single particle scattering operator $F = \sum f(i)$. The ISGMR energies ($m_k = \int E^k S(E) dE$) are given by:

$$E_{con} = \sqrt{\frac{m_1}{m_{-1}}} \qquad E_{cen} = \frac{m_1}{m_0} \qquad E_{scal} = \sqrt{\frac{m_3}{m_1}} \qquad (33)$$

where, E_{con} is the constrained energy, E_{cen} is the centroid energy, and E_{scal} is the scaling model energy. The Energy Weighted Sum Rule (EWSR), m_1, is calculated using the Hartree-Fock ground state wave function.

The fully self-consistent mean field calculation of the response function uses an effective two-nucleon interaction V which is obtained from a fit to the ground states properties of nuclei. The effective interaction determines the HF mean-field. The RPA calculation includes all of the components of the two-body interaction using a large configuration space and was done using the numerical approach of Refs. [68,69]. The calculations of the strength functions and centroid energies of the isoscalar (T=0) giant resonances in the nuclei were done using an occupation number approximation for the single particle orbits of open shell nuclei. For the single-particle scattering operator $F = \sum_i f(r_i)Y_{L0}$ we used $f(r) = r^2$ for the monopole (L=0) and $f(r) = r^3 - \frac{5}{3}\langle r^2 \rangle r$ was used for the dipole (L=1). The form of the dipole scattering operator takes into account the contribution from spurious states [70,71]. The KDE0v1 Skyrme-type effective interaction was used. The appropriate experimental excitation energy ranges were used: 9-40 MeV for the ISGMR and ISGQR, 9-20 MeV for the low-component of the ISGDR, 20-40 MeV for the high-component of the ISGDR. The calculated distributions are shown superimposed on the experimental results in the Figures 27-29 for ^{54}Fe, ^{64}Zn, and ^{68}Zn respectively. The smearing widths Γ for the calculated distributions for the E0-E2 multipoles are

shown in Table VIII. The energy moments are included in Tables IX and XI for ^{54}Fe, in Tables XII and XIV for ^{64}Zn, and in Tables XV and XVII for ^{68}Zn. The theoretical strengths are calculated over a range of 0 to 100 MeV and contain 100% of the EWSR for E0, E1, and E2.

Table VIII. Smearing widths for the calculated distributions are shown for ^{54}Fe, ^{64}Zn, and ^{68}Zn.

	E0	E1	E2
^{54}Fe, ^{68}Zn: Γ (MeV)	6.5	5.0	10.0
^{64}Zn: Γ (MeV)	6.5	13.0	10.0

5.6 Discussion

The E0-E2 multipole distributions obtained for ^{54}Fe, ^{64}Zn, and ^{68}Zn are shown in Figures 27, 28, and 29 respectively. Two peak fits are shown for the E1 distributions, and a single Gaussian fit is shown for E0 and E2. The parameters for these fits and the moments are shown in Tables X, XIII, and XVI for ^{54}Fe, ^{64}Zn, and ^{68}Zn respectively. E3 strength could not be reliably separated from E4 and higher because of the limited angular range of the data. The highest multipole included in the fits is E4, and the E3 distributions shown in Figures 27 - 29 are the sum of all the multipoles $L \geq 3$.

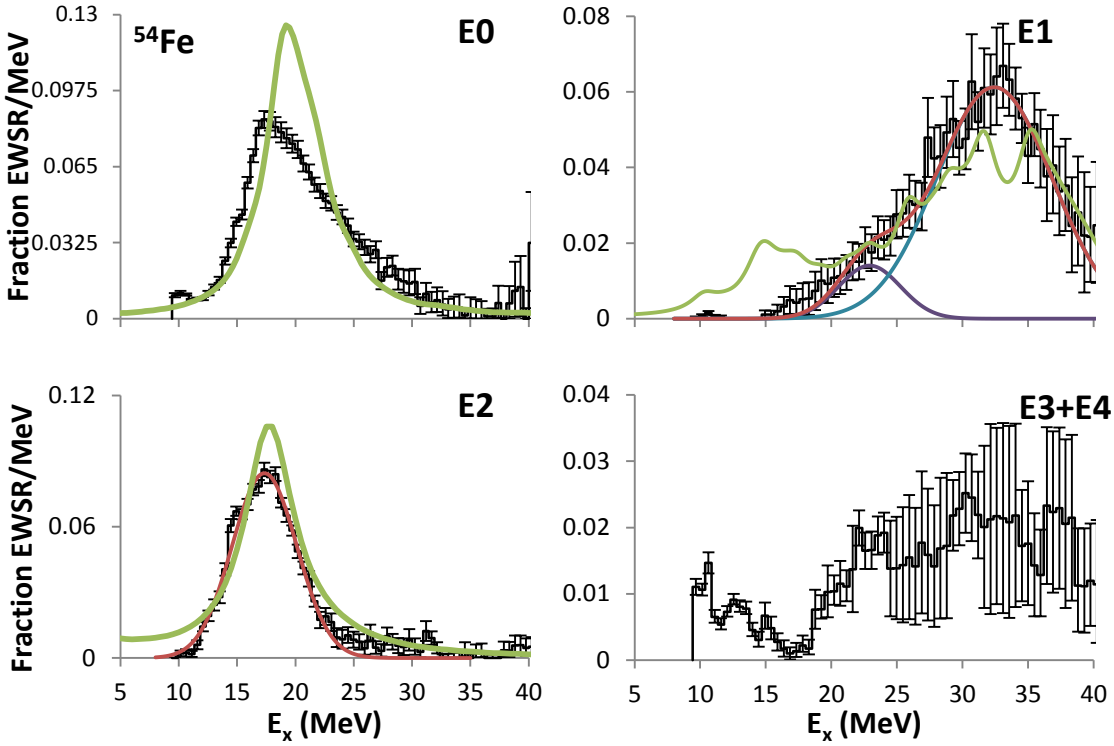

Figure 27. Strength distributions obtained for ^{54}Fe are shown by the histograms. Error bars represent the uncertainty based on the fitting of the angular distributions and different choices for the continuum, as described in the text. Parameters for moments of the strength distributions are in Table IX. For E1, two Gaussian fits for the low component (purple, smooth line) and high component (blue line) are shown as a sum (red line). A single Gaussian fit is shown for E2. The green lines are the strength distributions obtained with the HF-RPA calculations using the KDE0v1 interaction, smeared to more closely represent the data as discussed in the text. The Gaussian fit parameters and moments obtained from the calculations are shown in Table X.

Table IX. Parameters obtained for the moments of isoscalar multipoles in ^{54}Fe are shown. The KDE0v1 results are over the experimental energy range (9≤Ex≤40 MeV).

	Moments			
	$E0$		$E1$	$E2$
	Exp.	KDE0v1		
m_1 (Frac. EWSR)	$0.91\pm.11$	0.95	$0.78\pm.13$	$0.69\pm.14$
m_1/m_0(MeV)	$19.64\pm^{.39}_{.35}$	19.70	$29.39\pm^{.84}_{.82}$	$18.05\pm.87$
rms width (MeV)	$5.48\pm^{.89}_{.73}$	4.73	$5.47\pm^{.54}_{.49}$	$4.81\pm^{1.80}_{1.76}$
$\sqrt{m_3/m_1}$(MeV)	$21.60\pm^{.79}_{.68}$	21.16	$30.98\pm^{.80}_{.75}$	$19.69\pm^{1.78}_{1.76}$
$\sqrt{m_1/m_{-1}}$ (MeV)	$19.02\pm^{.31}_{.29}$	19.22	$28.69\pm^{.86}_{.85}$	$17.63\pm.68$

Table X. Parameters obtained for Gaussian fits for isoscalar multipoles in ^{54}Fe are shown.

	Gaussian fits		
	E1 peak 1	E1 peak 2	E2
Centroids (MeV)	$22.35\pm^{1.69}_{1.57}$	$32.22\pm^{1.00}_{.97}$	$17.31\pm.13$
FWHM (MeV)	$5.42\pm^{.80}_{1.12}$	$10.73\pm^{1.17}_{1.25}$	$6.70\pm.40$
Frac. EWSR	0.08	0.69	0.60

Table XI. Parameters obtained for energy moments of ^{54}Fe from the KDE0v1 calculation are shown. The results are over the experimental energy ranges (E1 low range: 9≤Ex≤20 MeV, E1 high range: 20≤Ex≤40 MeV, and E2: 9≤Ex≤40 MeV).

	KDE0v1		
	E1 peak 1	E1 peak 2	E2
m_1/m_0(MeV)	14.87	30.27	17.78
rms width (MeV)	2.87	5.21	5.10
m_1 (Frac. EWSR)	0.14	0.66	.87

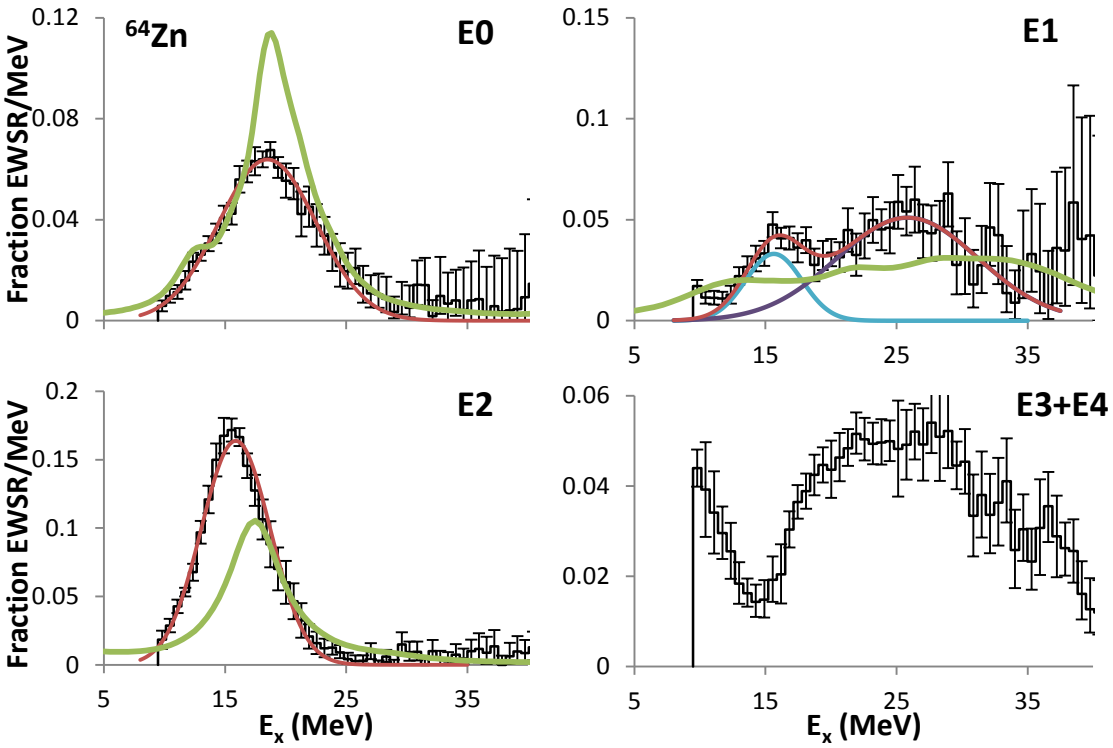

Figure 28. Strength distributions obtained for ^{64}Zn are shown by the histograms. Error bars represent the uncertainty based on the fitting of the angular distributions and different choices for the continuum, as described in the text. The green lines are the strength distributions obtained with the HF-RPA calculations using the KDE0v1 interaction, smeared to more closely represent the data as discussed in the text. The smooth red lines show Gaussian fits, the parameters of which are in Table XIII

Table XII. Parameters obtained for the moments of the isoscalar multipoles in ^{64}Zn are shown. The KDE0v1 results are over the experimental energy range ($9 \leq E_x \leq 40$ MeV)

	Moments			
	$E0$		$E1$	$E2$
	Exp.	KDE0v1		
m_1 (Frac. EWSR)	$0.70 \pm^{.14}_{.11}$	0.93	$1.08 \pm^{.27}_{.20}$	$1.20 \pm .13$
m_1/m_0(MeV)	$18.51 \pm^{1.16}_{.42}$	18.43	$23.28 \pm^{1.74}_{1.04}$	$15.81 \pm^{.35}_{.27}$
rms width (MeV)	$5.79 \pm^{2.54}_{1.12}$	5.21	$8.72 \pm^{2.94}_{1.89}$	$4.66 \pm^{2.20}_{1.74}$
$\sqrt{m_3/m_1}$(MeV)	$20.69 \pm^{1.88}_{1.01}$	20.27	$27.34 \pm^{2.58}_{1.61}$	$17.40 \pm^{1.26}_{.98}$
$\sqrt{m_1/m_{-1}}$ (MeV)	$17.90 \pm^{.84}_{.32}$	17.84	$21.68 \pm^{1.32}_{.75}$	$15.45 \pm^{.26}_{.23}$

Table XIII. Parameters obtained for Gaussian fits for isoscalar multipoles in ^{64}Zn are shown.

	Gaussian fits			
	$E0$	$E1$ peak 1	$E1$ peak 2	$E2$
Centroids (MeV)	$18.34 \pm .70$	$15.42 \pm^{.97}_{.90}$	$25.64 \pm^{1.23}_{1.19}$	$15.71 \pm .45$
FWHM (MeV)	9.21 ± 1.14	$4.59 \pm^{1.63}_{1.45}$	$12.58 \pm^{3.17}_{3.16}$	$6.43 \pm .65$
Frac. EWSR	0.64	0.19	0.68	1.13

Table XIV. Parameters obtained for energy moments of ^{64}Zn from the KDE0v1 calculation are shown. The results are over the experimental energy ranges (E1 low range: $9 \leq E_x \leq 20$ MeV, E1 high range: $20 \leq E_x \leq 40$ MeV, and E2: $9 \leq E_x \leq 40$ MeV).

	KDE0v1		
	E1 peak 1	E1 peak 2	E2
m_1/m_0(MeV)	14.24	28.83	17.55
rms width (MeV)	3.36	5.55	5.29
m_1 (Frac. EWSR)	0.23	0.57	.88

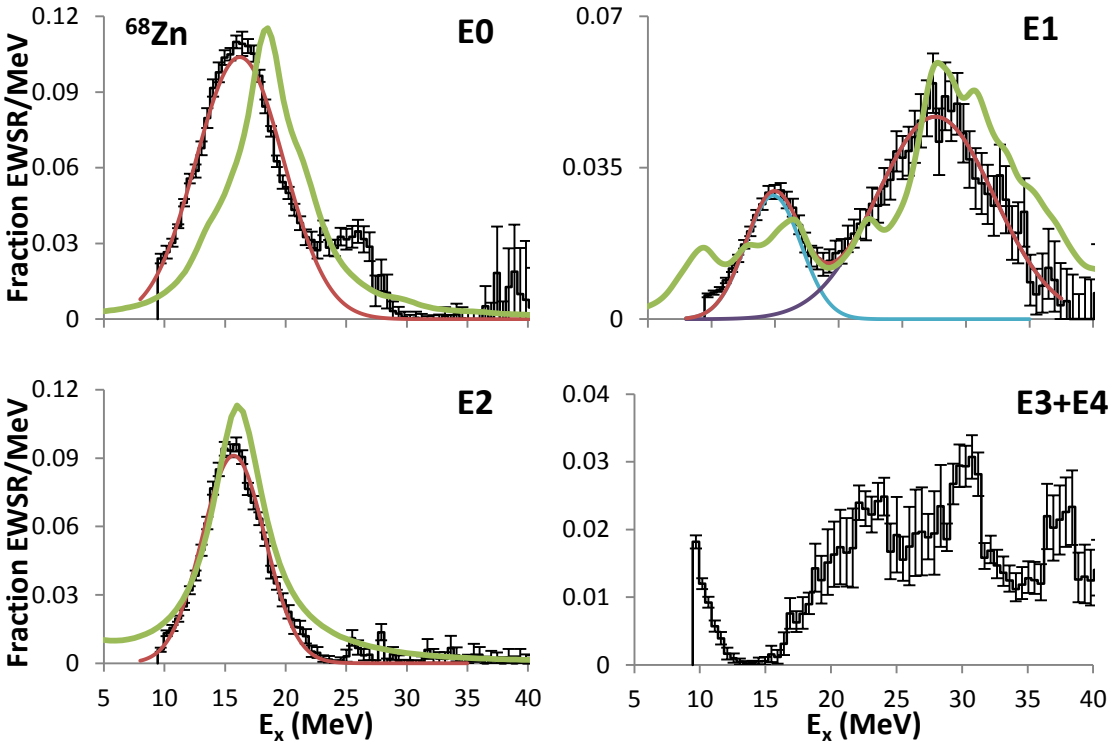

Figure 29. Strength distributions obtained for ^{68}Zn are shown by the histograms. Error bars represent the uncertainty based on the fitting of the angular distributions and different choices for the continuum, as described in the text. The smooth lines show Gaussian fits, the parameters of which are in Table XV. The green lines are the strength distributions obtained with the HF-RPA calculations using the KDE0v1 interaction, smeared to more closely represent the data as discussed in the text.

Table XV. Parameters obtained for isoscalar multipoles in ^{68}Zn are shown. The KDE0v1 results are over the experimental energy range (9≤Ex≤40 MeV).

	Moments			
	$E0$		$E1$	$E2$
	Exp.	KDE0v1		
m_1 (Frac. EWSR)	$1.05\pm^{.11}_{.10}$	0.95	0.71±.12	0.60±.10
m_1/m_0(MeV)	$16.57\pm^{.20}_{.14}$	18.19	$22.38\pm^{.42}_{.33}$	15.54±.32
rms width (MeV)	$4.81\pm^{1.08}_{.74}$	5.02	$7.18\pm^{.50}_{.30}$	3.16±1.13
$\sqrt{m_3/m_1}$(MeV)	$18.30\pm^{.69}_{.46}$	19.91	$25.60\pm^{.60}_{.38}$	$16.42\pm^{.84}_{.80}$
$\sqrt{m_1/m_{-1}}$ (MeV)	$16.06\pm^{.14}_{.11}$	17.65	$21.09\pm^{.36}_{.30}$	15.28±.25

Table XVI. Parameters obtained for Gaussian fits for isoscalar multipoles in ^{68}Zn are shown.

	Gaussian fits			
	$E0$	E1 peak 1	E1 peak 2	$E2$
Centroids (MeV)	16.23±.12	14.85±.19	27.65±.39	15.71±.10
FWHM (MeV)	8.61±.20	$5.12\pm^{.45}_{.42}$	$10.92\pm^{.61}_{.64}$	6.10±.12
Frac. EWSR	0.93	0.15	0.54	0.59

Table XVII. Parameters obtained for energy moments of ^{68}Zn from the KDE0v1 calculation are shown. The results are over the experimental energy ranges (E1 low range: 9≤Ex≤20 MeV, E1 high range: 20≤Ex≤40 MeV, and E2: 9≤Ex≤40 MeV)

	KDE0v1		
	E1 peak 1	E1 peak 2	E2
m_1/m_0(MeV)	14.24	29.84	16.32
rms width (MeV)	3.06	4.61	5.02
m_1 (Frac. EWSR)	0.19	0.67	0.89

5.6.1 E0 Strength

Most of the E0 strength was identified in the excitation energy range of 10-35 MeV for ^{54}Fe (91±11%), ^{64}Zn (70^{+14}_{-11}%), and ^{68}Zn (105^{+11}_{-10}%). The shape of the strength distribution in ^{54}Fe is typical of the mass region. It is fit well by a Gaussian on the low-excitation side, but the strength distribution has a tail on the high-excitation side (Figure 27). This tailing causes the calculated moments for ^{54}Fe to have much larger positive errors than negative errors. The strength distribution obtained with the HF-RPA calculation is symmetric, does not show the tailing seen in the experimental distribution, and is apparently at a higher energy. Despite these differences in the shape, the calculated and experimental peaks have centroid, scaling, and constrained energy

moments which are in good agreement. The calculated strength seen over the energy range (9-40 MeV) is in agreement with the experimental strength identified (≈90%).

The distributions for ^{64}Zn and ^{68}Zn do not show the tailing seen in ^{54}Fe and in the nuclei shown in Figure 20. The ^{64}Zn E0 strength distribution (Figure 28) is fit very well by the Gaussian. The distribution obtained with the HF-RPA calculation for ^{64}Zn shows a component at low excitation but is otherwise in good agreement with the experimental distribution. Only $70\pm^{14}_{11}$% of the EWSR was identified in the experiment, whereas the calculation shows 93% of the E0 EWSR in this region. The energy moments of the experimental and theoretical distributions are in very good agreement. The E0 strength distribution for ^{68}Zn (Figure 29) has two components similar to that seen in the E0 strength distributions for the nuclei in the A≈90 region [28]. The distribution obtained with the HF-RPA calculation does not show a second component. The calculated peak is shifted to the right of the experimental one by ≈1.5 MeV. The amount of strength predicted by the calculation is in agreement with the experimental strength.

Nayak *et al.* did HF-RPA calculations for a number of nuclei using Skyrme or Skyrme-like interactions, then fit these results with the Leptodermous expansion to obtain Leptodermous parameters that could be used to predict K_A for other nuclei [15].

$$K(A,I) = \langle r^2 \rangle \frac{M}{\hbar^2} E_{BR}^2$$

$$K(A,I) = K_V + K_{SF}A^{-\frac{1}{3}} + K_{VS}I^2 + K_{Coul}Z^2A^{-\frac{4}{3}} + K_4I^4 + K_{SS}I^2A^{-\frac{1}{3}} + K_{CV}A^{-\frac{2}{3}}$$

K(A,I) is the incompressibility of the finite nucleus with mass A and asymmetry term $I = \frac{N-Z}{A}$. The mean squared radius $\langle r^2 \rangle$ of the nucleus is taken from experimental data. In the Leptodermous expansion, K_v, is the incompressibility of infinite nuclear matter (or K_{NM}). K_{VS} and K_4 are volume symmetry terms. K_{Coul} is the Coulomb term. K_{SF} is the surface term, and K_{SS} is the surface-symmetry term. Chossy and Stocker did a similar parameterization using Relativistic Mean-Field (RMF) parameter sets [75]. This approach starts with a microscopic Lagrangian with parameter sets that give a good reproduction of nuclear ground state properties.

A comparison of the experimental values of the scaling model energy for $E_{GMR}\left(\sqrt{\frac{m_3}{m_1}}\right)$ with the values calculated from Nayak's [15] calculation based on the SkM*(K_{NM}=216.6 MeV), and Chossy and Stocker's [75] calculations based on NLC (K_{NM}=224.5 MeV) and NL1 (K_{NM}=211.1 MeV) non-relativistic and relativistic parameter sets are included in Figure 30. The ^{54}Fe and ^{64}Zn experimental values agree within the uncertainty with the NLC and NL1 values. The experimental value for ^{68}Zn agrees within uncertainty with the SkM* value and is ~ 1.5 MeV below those calculated with the NLC and NL1 parameter sets. Interestingly, the energies of the GMR in four nuclei (^{40}Ca, ^{56}Fe, ^{60}Ni,

and ^{68}Zn) agree with the SkM* value, while those in four other nuclei (^{54}Fe, ^{58}Ni, ^{64}Zn, and ^{90}Zr) agree with the NLC and NL1 values.

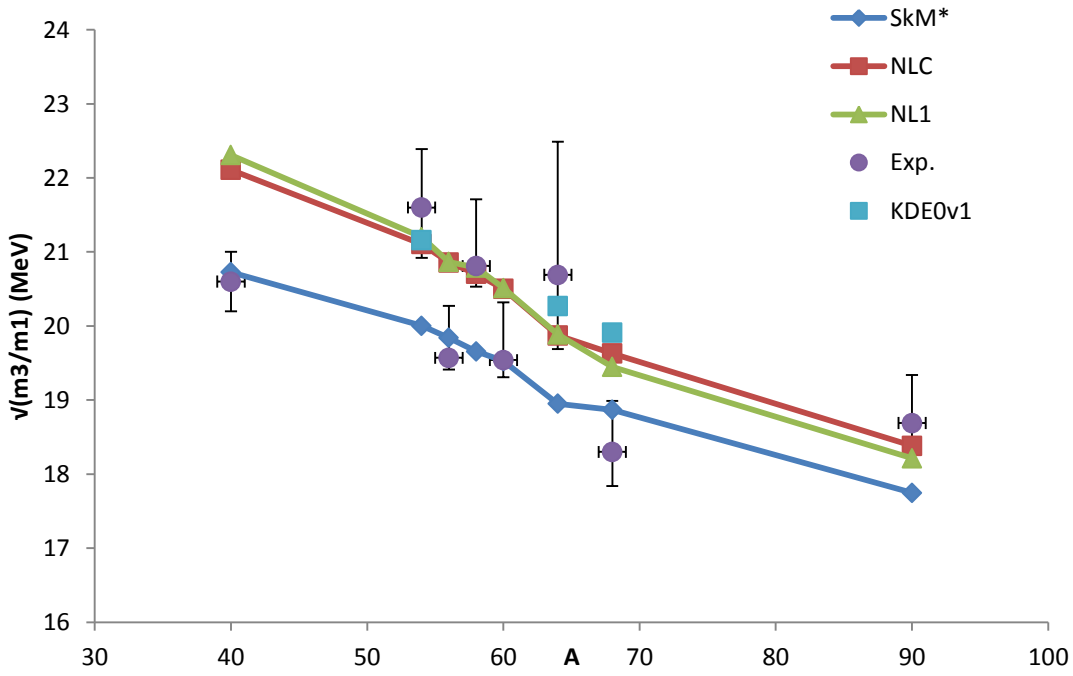

Figure 30. Experimental GMR energies (represented by solid circles) are compared with values calculated by RMF parameterizations [75] (red squares and green triangles) and Skyrme non-relativistic parameterization [15] (blue diamonds). The error bars on the data include systematic errors. The light blue squares are the values obtained from the KDE0v1 interaction. The experimental energies for ^{40}Ca from Ref. [49]; ^{56}Fe, ^{58}Ni, and ^{60}Ni from Ref. [27]; and ^{90}Zr from Ref. [74] are included.

5.6.2 E1 Strength

The E1 strength distributions for ^{54}Fe, ^{64}Zn, and ^{68}Zn are separated into two components, which is a characteristic consistent with the measured and calculated E1 strength distributions in heavier nuclei [77--79]. The observed E1 strength is quite sensitive to the continuum because the high excitation component dominates in the distribution with strength extended to and maybe above 40 MeV. Above 30 MeV, the ISGDR cross sections and the peak-to-continuum ratio are small. The larger uncertainty seen in the E1 strength distributions compared to those of E0 and E2 in Figures 27-29 are due to this dependence on continuum choice.

A majority of the E1 strength in ^{54}Fe was identified (78±13%) (Table IX). The observed components in the strength distribution for ^{54}Fe are fit by two Gaussians with centroids of $22.35\pm^{1.69}_{1.57}$ MeV and $32.22\pm^{1.00}_{.97}$ MeV. The higher energy component appears to extend beyond the measured 45 MeV range, which possibly accounts for the missing E1 strength. The experimental energies of the high and low components are compared in Figure 31 with the energies obtained from the HF-RPA calculations. In the theoretical distribution, the low energy component (measured in the range $9\leq E_x\leq 20$ MeV) is lower in energy than the experimental one by ≈ 7 MeV. The energy of the high component ($20\leq E_x\leq 45$ MeV) is in agreement within uncertainty with experiment. The energies of both components are higher than the energies observed in the Zn isotopes by ≈4-6 MeV.

In the case of ^{64}Zn, the observed E1 strength is $108\pm^{27}_{20}$% of the EWSR. The strength distribution has two components which are fit very well by two Gaussians with centroids of $15.42\pm^{.97}_{.90}$ MeV and $25.64\pm^{1.23}_{1.19}$ MeV. More strength appears (17%) in the lower energy component than has been typical in the other mid-mass nuclei studied. In ^{56}Fe, ^{58}Ni, and ^{60}Ni, the amount of E1 strength identified in the lower energy component was less than 10% in each case [27].

A majority of the E1 strength (71±12%) for ^{68}Zn is observed in the region below 40 MeV. The two components are fit very well with Gaussians separated by about 12 MeV. The centroid for the low component is 14.84±.17 MeV and for the high component is 27.63±.33 MeV. As in ^{64}Zn, the low energy component has more strength (15%) than has been found in the other mid-mass nuclei. Generally, the distribution from the HF-RPA calculation is in good agreement with the data, with the exception of extra strength seen below the low component peak and above the high component peak. In the low energy range ($9\leq E_x\leq 20$ MeV), the calculated and experimental centroids are in near agreement. In the high energy range ($20\leq E_x\leq 36$ MeV) the calculated centroid is greater than the experimental one by ≈1 MeV. Similar amounts of the calculated and experimental strength were identified in the respective energy ranges.

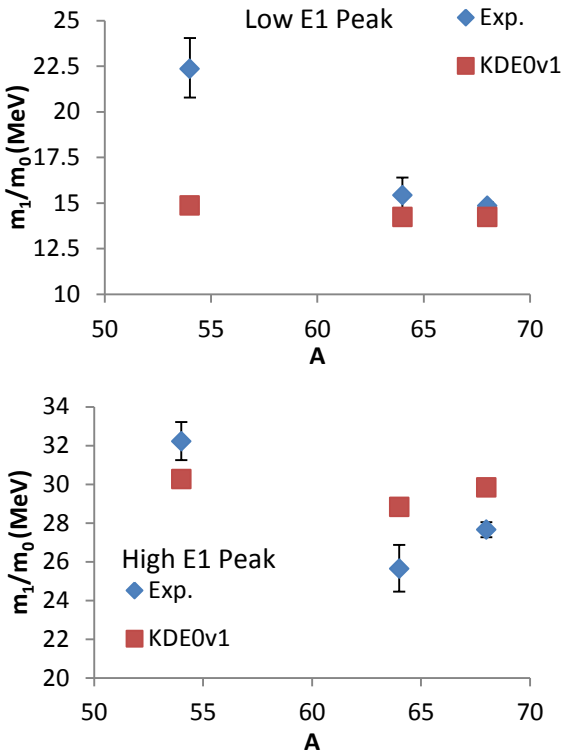

Figure 31. The centroid of the Gaussian fit (blue diamonds) to the low and high energy peak in the ISGDR distributions for ^{54}Fe, ^{64}Zn, and ^{68}Zn are plotted vs. A. The error bars indicate the uncertainty obtained using the errors shown in Tables X, XIII, and XVI. The red squares show m_1/m_0 in the range $9 \leq E_x \leq 20$ MeV for the low peak and the range $20 \leq E_x \leq 36$ MeV for the high peak calculated with HF-RPA using the KDE0v1 interaction.

5.6.3 E2 Strength

Two-thirds of the E2 strength (~65%) was identified in ^{54}Fe and ^{68}Zn, while 120± 13% of the strength was identified for ^{64}Zn. In the other nuclei studied in this region, typically between 60-80% of the EWSR was identified. In Ref. [76], 113 ± 15% of the strength for ^{58}Ni was identified, but in that work, the authors concluded that the E2 strength was sensitive to the choice of continuum but were unable to assign an uncertainty associated

with the continuum choice. The development of the multipole analysis program allowed for a more precise determination of the multipole strength distributions and for the comparison of the strength distributions obtained from many analyses using different continuum choices. In Ref. [27], a re- analysis of the ^{58}Ni data using this improved technique located 82 ± 10% of the strength. The strength lies between 10 and 25 MeV for ^{54}Fe, ^{64}Zn, and ^{68}Zn and is well fit in each case by a Gaussian shape. This characteristic is common among all the other nuclei that have been studied in the A=40-68 region. The theoretical (m_1/m_0) centroid energies for the 9-40 MeV range for ^{54}Fe and ^{68}Zn are in agreement within the uncertainty with the experimental values. The predicted peak for ^{64}Zn is located 2 MeV higher in energy than the experimental one.

5.7 Summary

We have obtained distributions for isoscalar E0, E1, and E2 strength in ^{54}Fe, ^{64}Fe, and ^{68}Zn and compared these to spherical Hartree-Fock-RPA calculations using the KDE0v1 Skyrme type interaction. In ^{54}Fe, the shape of the calculated strength distribution did not agree with the experimental one, but the energy moments were in agreement. In ^{64}Zn, the calculated strength distribution was in good agreement with the experimental one, but in ^{68}Zn it was not. The GMR scaling energies ($\sqrt{(m_3/m_1)}$) for these nuclei were compared with the energies of nuclei in the A=40-90 region and with calculated energies obtained from Leptodermous expansion parameterizations of HF-RPA and RMF calculations. The

predicted energies associated with the RMF calculations were in agreement with the experimental E0 energies obtained for ^{54}Fe and ^{64}Zn. The experimental E0 energy for ^{68}Zn was in agreement with the value predicted from the parameterization of the HF-RPA calculations. As in other nuclei in the mass region, the E0 strength for ^{54}Fe is asymmetric with tailing on the high energy side. This tailing is not seen in ^{64}Zn, and in ^{68}Zn, the shape may be in two components similar to the E0 distributions in the A≈90 region [28,67].

6 ISOSCALAR E0, E1, E2, AND E3 STRENGTH IN ^{94}MO

6.1 Overview

Isoscalar giant resonances in ^{94}Mo have been studied with inelastic scattering of 240 MeV α particles at small angles including 0°. All of the expected EWSR for the isoscalar E0 resonance was found (104%). A significant portion of the EWSR was found for the isoscalar E1 (75%), E2 (61%), and the high energy octupole E3 (46%) resonances. The strength distributions are compared with the predictions from HF-RPA calculations with the KDE0v1 interaction.

6.2 Introduction

Giant Resonances (GR) are the broad resonances that occur at excitation energies between 10 and 30 MeV. They correspond to the collective motion of nucleons within the nucleus and have modes classified according to their multipolarity L, spin S, and isospin T quantum numbers. The Isoscalar Giant Monopole Resonance (ISGMR) is interesting because its excitation energy is directly related to the incompressibility of the nucleus K_A (28), where $\langle r^2 \rangle$ is the mean square radius and *m* is the mass of the nucleus [13,14].

$$E_{GMR} = \sqrt{\left(\frac{\hbar^2 K_A}{m\langle r^2 \rangle}\right)} \tag{34}$$

K_A can be used to obtain the incompressibility of nuclear matter K_{NM} by comparison to calculations using mean fields, where the value for K_{NM} is deduced from the interaction that best reproduces the experimental data on the strength functions of the giant resonance. At present, the best value for K_{NM} is 220-240 MeV [24].

Isoscalar giant resonances in the Mo isotopes were first observed by Moalem *et al*. who identified the Giant Quadrupole Resonance (GQR) in all stable Mo isotopes using inelastic scattering of 110 MeV ^{3}He [80]. Duhamel *et al.* [81] investigated the GQR and GMR in ^{92}Mo using inelastic scattering of 152 MeV α particles. Youngblood *et al.* studied the isoscalar giant resonances in ^{90,92,94}Zr and ^{92,96,98,100}Mo [28,67,82] using inelastic scattering of 240 MeV α particles at small angles including 0°. Ref. [28] focused on the E0 strength distribution, which showed high and low-energy components separated by 7-9 MeV in these Zr and Mo isotopes. The higher energy second peak is not predicted by the HF-RPA calculations that reproduce the ISGMR energies in the other nuclei. For the nuclei with $A \neq 92$, 80-90% of the strength is in the lower energy peak located at 15.7 to 17.2 MeV. In the A = 92 nuclei, there is considerably more strength in the higher energy peak than in the higher energy peak of the $A \neq 92$ nuclei. This enhancement of the strength in the higher energy region for ^{92}Zr and ^{92}Mo results in K_A values for these two nuclei that are 8σ and 4σ above those obtained with interactions that predict K_A values in agreement with those for the other Zr and Mo isotopes [28]. The excellent peak-to-continuum ratio [37,43,50,61] of data obtained with 240 MeV α

particles allows identification of the GDR, GQR, and HEOR strength distributions in the range $9 \leq E_x \leq 36$ MeV. The strength distributions for these resonances in the Zr [82] and Mo [67] isotopes were investigated and compared to the results of spherical Hartree-Fock – based random-phase-approximation (HF-RPA) calculations [68] with KDE0v1 Skyrme-type effective interaction [72].

In this paper we report E0, E1, E2, and E3 multipole strength distributions obtained for ^{94}Mo and compared them to HF-RPA calculations with the KDE0v1 interaction.

6.3 Experimental Procedure

The experimental technique has been described thoroughly in Refs. [37,61] and is summarized briefly below. Beams of 240 MeV α particles from the Texas A&M K500 super-conducting cyclotron bombarded a self-supporting ^{94}Mo foil of 4.8 mg/cm^2 enriched to more than 95% in the desired isotope, located in the target chamber of the multipole-dipole-multipole spectrometer. The horizontal and vertical acceptance of the spectrometer was 4°. Ray tracing was used to reconstruct the scattering angle. The vertical acceptance was ±2°. The focal plane detector measured position and angle in the scattering plane, covering $E_x \approx 8$ MeV to $E_x > 55$ MeV (depending on scattering angle). The out-of-plane scattering angle was not measured. Position resolution of approximately 0.9 mm and scattering angle resolution of about 0.09° were obtained. Cross sections were obtained from the charge collected, target thickness, dead time, and

known solid angle. The target thicknesses were measured by weighing and checked by measuring the energy loss of the 240 MeV α beam in each target. The cumulative uncertainties in target thickness, solid angle, etc., result in about a ±10% uncertainty in absolute cross sections. ^{24}Mg spectra were taken before and after each run, and the 13.85±.02 MeV L=0 state [62] was used as a check on the calibration in the giant resonance region.

Data were taken with the spectrometer at 0.0° (0.0° < θ < 2.0°) and at 4.0° (2.0° < θ < 6.0°). Sample spectra obtained for ^{94}Mo are shown in Figure 32.

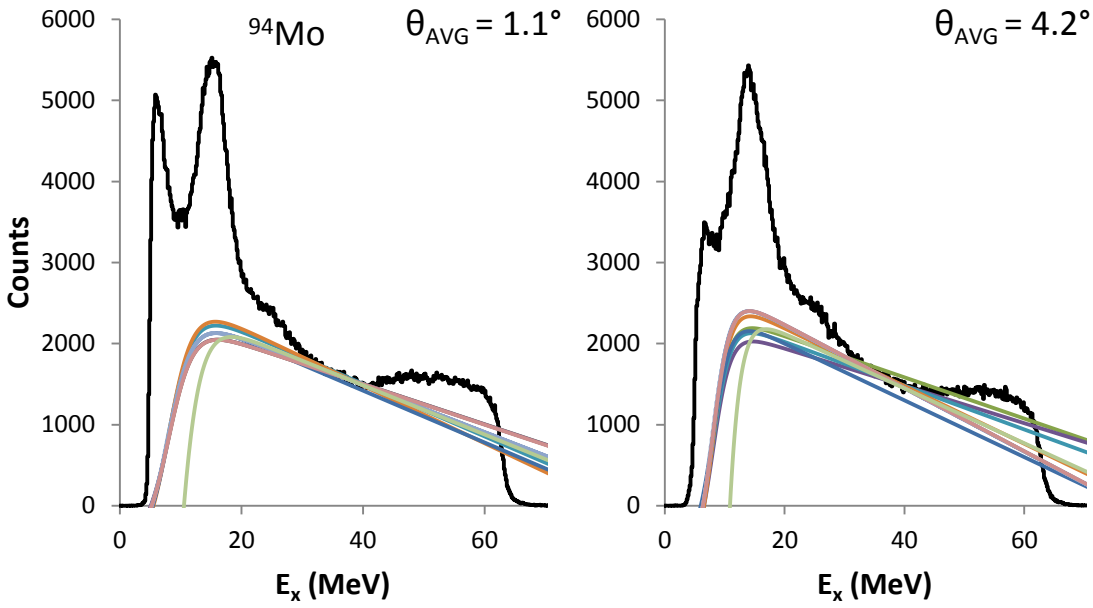

Figure 32. Inelastic α spectra obtained for ^{94}Mo are plotted vs. excitation energy. The lines are examples of continua chosen for analyses.

6.4 Multipole Analysis

Single-folding DWBA calculations (as described in Refs. [37,53,61]) were carried out with PTOLEMY [54]. Optical model parameters obtained for 240 MeV α scattering on ^{90}Zr [18] were used and are shown in Table XVIII.

Table XVIII. Optical Model and Fermi parameters used in DWBA calculations for ^{94}Mo are shown, r_{c0} is the Coulomb radius parameter.

V (MeV)	W (MeV)	r_i (fm)	a_i (fm)	r_{c0}	c	a
40.2	40.9	0.786	1.242	.960	5.0264	.515

Calculations were performed with a Fermi mass distribution, $\rho(r) = \rho_0 \left[1 + e^{\frac{r-c}{a}}\right]^{-1}$, with c and a shown in Table XVIII [63]. The calculations for the transition densities, sum rules, and DWBA calculations were discussed thoroughly in Refs. [37,53,61,66].

The peak and continuum cross-sections are then divided into bins by excitation energy. To obtain the multipole components for each experimental bin, the experimental angular distributions of the peak and continuum cross-sections are compared to the single-

folding DWBA calculations done with PTOLEMY, and then the strengths of the isoscalar L=0-4 contributions are varied in order to minimize χ^2. The IVGDR contributions are calculated and held fixed in the fits. The experimental and calculated angular distributions are illustrated in Figure 33 for selected energy bins in the GR peak. The uncertainty for each multipole is determined by incrementing or decrementing the strength of that multipole, adjusting the strengths of other multipoles by fitting to the data, and continuing until the new χ^2 is 1 unit larger than the χ^2 from the best fit.

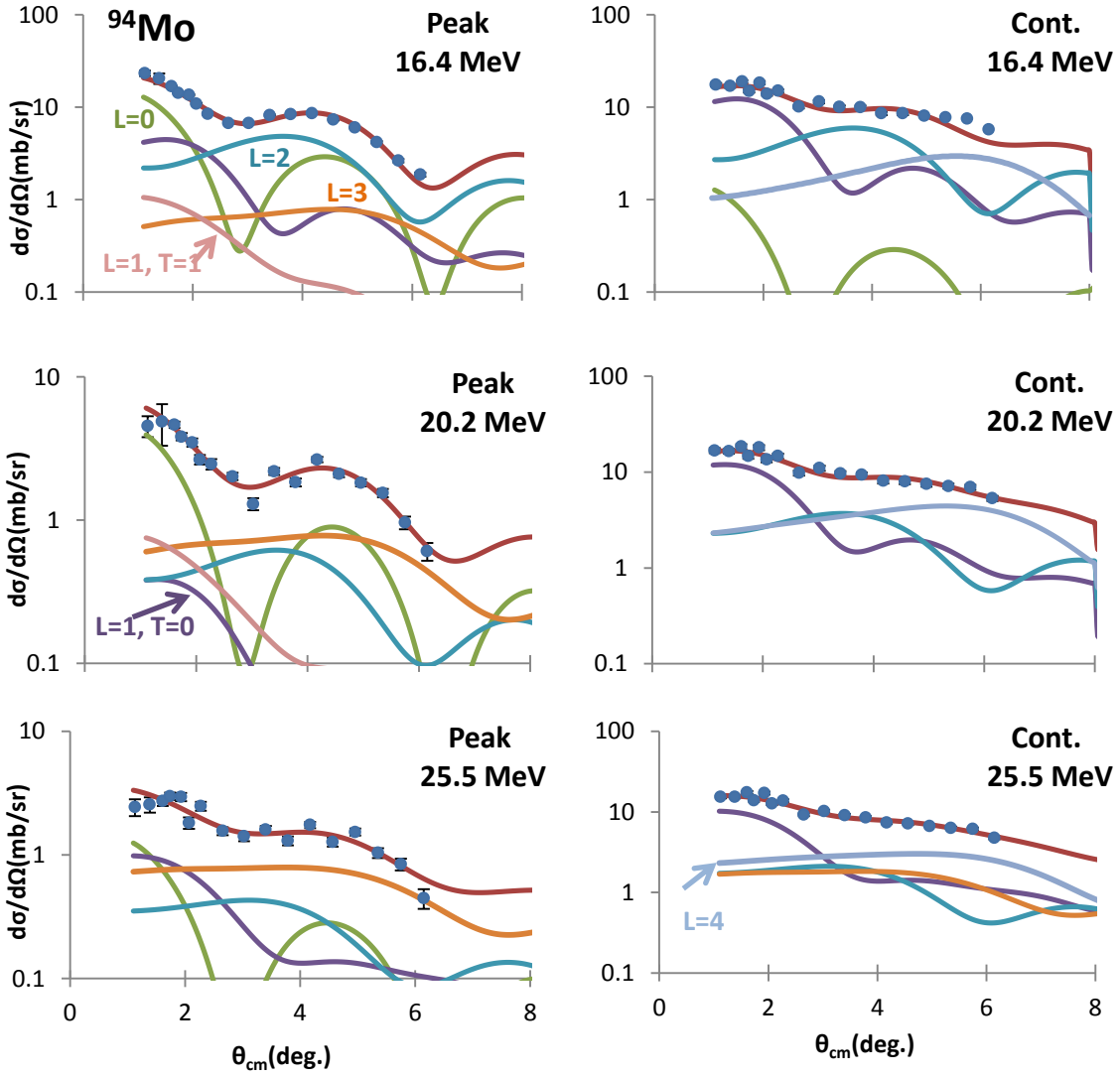

Figure 33. The angular distributions of the ^{94}Mo cross sections for three excitation ranges of the GR peak and the continuum are plotted vs. center-of-mass scattering angle. Each bin is 480 keV wide and the average energies for each bin are shown. The lines through the data points indicate the multipole fits. The contributions of each multipole are shown. The statistical errors are smaller than the data points.

Analyses are done several times using different assumptions about the continuum in order to estimate the uncertainties due to the choice of continuum. Typical choices for the continuum can be seen in Figure 32. For purposes of estimating the uncertainties, the

continuum could have a linear slope at high excitation that does not quite match the experimental data, could be lowered so that it is always below the data, could have a different low energy cutoff and slope, or can have slope and or amplitude which is altered at selected angles.

These separate analyses are then combined into an average distribution. Errors were calculated by adding the errors from the multipole fits in quadrature with the standard deviations between the different fits.

6.5 Description of Microscopic Calculations

Microscopic mean-field based Random Phase Approximation (RPA) theory provides a description of collective states in nuclei [12,24]. A description of the spherical HF-based RPA calculations of the strength functions and centroid energies of the isoscalar (T=0) giant resonances in nuclei can be found in Ref. [67] and is summarized below.

The strength or response function can be obtained from the RPA states $|n\rangle$ with corresponding energy E_n:

$$S(E) = \sum_n |\langle 0|F|n\rangle^2|\delta(E - E_n) \tag{35}$$

where F is the single particle scattering operator $F = \sum f(i)$. The ISGMR energies ($m_k = \int E^k S(E) dE$) are given by:

$$E_{con} = \sqrt{\frac{m_1}{m_{-1}}} \qquad E_{cen} = \frac{m_1}{m_0} \qquad E_{scal} = \sqrt{\frac{m_3}{m_1}} \qquad (36)$$

where, E_{con} is the constrained energy, E_{cen} is the centroid energy, and E_{scal} is the scaling model energy. The Energy Weighted Sum Rule (EWSR), m_1, is calculated using the Hartree-Fock ground state wave function.

The fully self-consistent mean field calculation of the response function uses an effective two-nucleon interaction V which is obtained from a fit to the ground states properties of nuclei. The effective interaction determines the HF mean-field. The RPA calculation includes all of the components of the two-body interaction using a large configuration space and was done using the numerical approach of Refs. [68,69]. The calculations of the strength functions and centroid energies of the isoscalar (T=0) giant resonances in the nuclei were done using an occupation number approximation for the single particle orbits of open shell nuclei. For the single-particle scattering operator $F = \sum_i f(r_i)Y_{L0}$ we used $f(r) = r^2$ for the monopole (L=0) and $f(r) = r^3 - \frac{5}{3}\langle r^2 \rangle r$ was used for the dipole (L=1). The form of the dipole scattering operator takes into account the contribution from spurious states [70,71]. The KDE0v1 Skyrme-type effective interaction was used. The appropriate experimental excitation energy ranges were used: 9-40 MeV for the ISGMR and ISGQR, 9-20 MeV for the low-component of the ISGDR, 20-36 MeV for the high-component of the ISGDR, and 14-40 MeV for the HEOR. The calculated distributions are shown superimposed on the experimental results in Figure 34. The smearing widths for the calculated distributions for the E0-E3 multipoles are shown in

Table XIX. The energy moments are included in Tables XX and XXII. The theoretical strengths are calculated over a range of 0 to 100 MeV and contain 100% of the EWSR for E0-E3.

Table XIX. Smearing widths for the calculated distributions are shown.

	E0	E1	E2	E3
Γ (MeV)	6.5	5.0	10.0	13.0

6.6 Discussion

The E0-E3 multipole distributions obtained for ^{94}Mo are shown in Figure 34. Two peak fits are shown for the E0 and E1 distributions, and a single Gaussian fit is shown for E2 and E3. The parameters for these fits and for the moment ratios (m_1/m_0 and $\sqrt{(m_3/m_1)}$) are shown in Table XX.

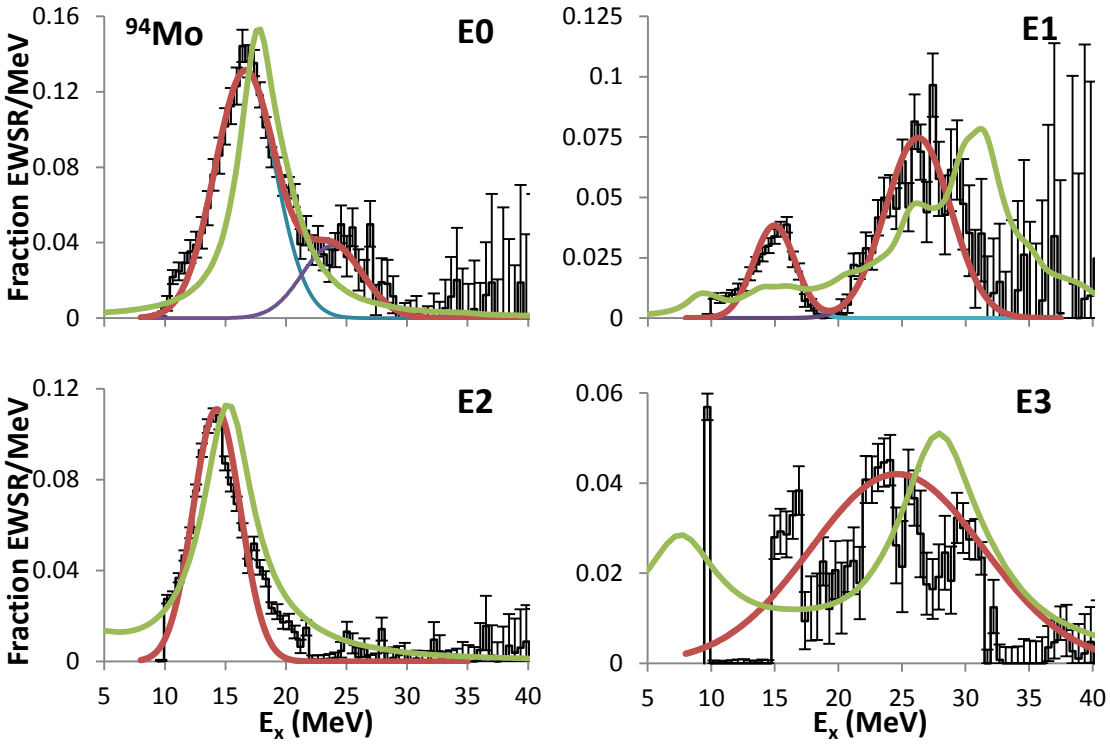

Figure 34. Strength distributions obtained for ^{94}Mo are shown by the histograms. Error bars represent the uncertainty based on the fitting of the angular distributions and different choices for the continuum, as described in the text. Gaussian fits to the E0 and E1 distributions for the individual peaks (blue and purple) and their sum (red) are shown. The green lines are the strength distributions obtained with the HF-RPA calculations using the KDE0v1 interaction, smeared to more closely represent the data as discussed in the text.

Table XX. Parameters for energy moments obtained for isoscalar multipoles in ^{94}Mo are shown. The moments from the KDE0v1 calculation results are over the experimental energy range $9 \leq E_x \leq 40$ MeV.

	Moments				
	$E0$		$E1$	$E2$	E3
	Exp.	KDE0v1			
m_1 (Frac. EWSR)	$1.12 \pm^{.19}_{.12}$	.95	$0.83 \pm^{.35}_{.20}$	$0.77 \pm^{.11}_{.10}$	$.45 \pm .10$
m_1/m_0(MeV)	$17.57 \pm^{1.14}_{.30}$	18.06	$24.57 \pm^{3.41}_{1.59}$	$16.12 \pm^{.66}_{.39}$	$21.10 \pm^{.31}_{.17}$
rms width (MeV)	$5.68 \pm^{5.53}_{1.93}$	4.40	$8.02 \pm^{3.89}_{1.81}$	$7.61 \pm^{1.74}_{1.04}$	$6.64 \pm^{.53}_{.30}$
$\sqrt{m_3/m_1}$ (MeV)	$19.62 \pm^{3.54}_{1.15}$	19.39	$28.20 \pm^{4.61}_{2.11}$	$19.56 \pm^{1.92}_{1.12}$	$24.03 \pm^{.73}_{.28}$
$\sqrt{m_1/m_{-1}}$ (MeV)	$17.06 \pm^{.75}_{.19}$	17.67	$23.09 \pm^{2.84}_{1.31}$	$15.48 \pm^{.44}_{.26}$	$19.84 \pm^{.23}_{.17}$

Table XXI. Parameters obtained for Gaussian fits for isoscalar multipoles in ^{94}Mo are shown.

	Gaussian fits		
	$E0$ peak 1	E0 peak 2	$E2$
Centroids (MeV)	$16.51 \pm^{.19}_{.21}$	$23.59 \pm^{.78}_{.76}$	$14.55 \pm .13$
FWHM (MeV)	$5.73 \pm^{.39}_{.36}$	$5.87 \pm^{1.06}_{1.14}$	$5.28 \pm .17$
Frac. EWSR	0.82	0.21	0.59
	Gaussian fits		
	$E1$ Low Peak	$E1$ High Peak	E3
Centroids (MeV)	$15.07 \pm^{.22}_{.19}$	$26.50 \pm^{.44}_{.42}$	24.60±.46
FWHM (MeV)	$3.19 \pm^{.36}_{.22}$	$5.99 \pm^{.45}_{.49}$	$9.24 \pm^{.53}_{.50}$
Frac. EWSR	0.12	0.45	0.39

Table XXII. Parameters obtained for energy moments from the KDE0v1 calculation are shown. The results are over the experimental energy ranges (E1 low range: 9≤Ex≤20 MeV, E1 high range: 20≤Ex≤40 MeV, E2: 9≤Ex≤40 MeV, and E3: 14≤Ex≤40 MeV)

	KDE0v1			
	$E1$ Low Range	$E1$ High Range	E2	E3
m_1/m_0 (MeV)	14.29	29.05	16.54	25.98
rms width (MeV)	3.31	4.49	5.05	5.63
m_1 (Frac. EWSR)	0.13	0.77	0.86	0.64

6.6.1 E0 Strength

In the E0 strength distribution, $112\pm^{19}_{12}$% of the sum rule was identified in the energy range analyzed, $9 \leq E_x \leq 40$ MeV. As in other A≈90 nuclei [28,67,82], the strength is separated into high and low energy components. The low-energy component is fit well with a Gaussian centered at 16.51 MeV. This peak contains about 82% of the EWSR. The high-energy component is at 23.59 MeV and contains approximately 21% of the EWSR. The energies and strengths of the components follow the general trend seen for the other Mo isotopes studied in Refs. [28,67]. The energies obtained for the 4 Mo isotopes from Refs. [28,67] and for ^{94}Mo from the two peak fits are plotted versus A in Figure 35. Lines representing $74/A^{\frac{1}{3}}$ and $109/A^{\frac{1}{3}}$ are shown as a reference on the low

and high plots. The low energy peak is possibly moving faster than $A^{-1/3}$, while the high energy peak shows no systematic change in energy. As was observed in the other Mo isotopes [28,67], the results of the HF-RPA calculation for the E0 strength calculation show a single, slightly asymmetrical peak concentrated in a narrow band just above the narrow peak in the data. Although the distributions are not in agreement, the centroid, scaled, and constrained energy moments are in agreement within the errors.

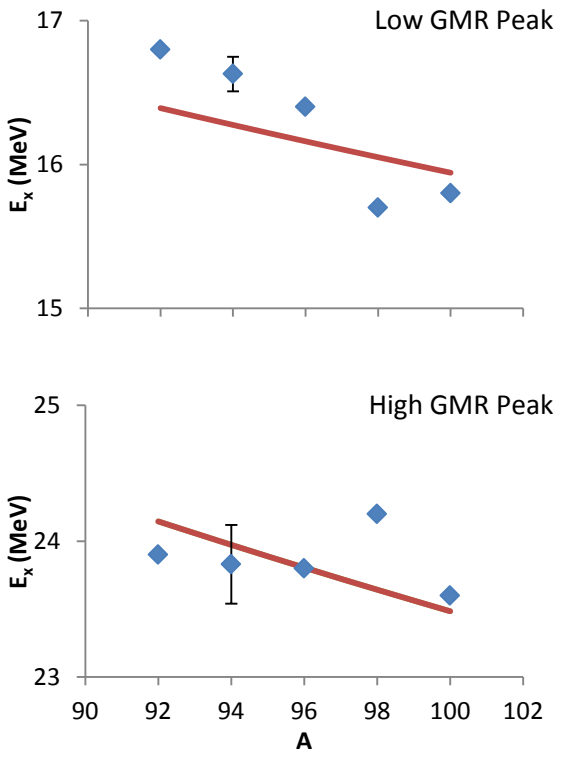

Figure 35. The centroids of the Gaussians obtained from the fits to the E0 distributions for the Mo isotopes are plotted vs. A. The (red) lines show $74A^{-1/3}$ and $109A^{-1/3}$ in the upper and lower plots respectively. The error bars represent the uncertainty in energy for ^{94}Mo, but Ref. [67] did not report the uncertainties for the other isotopes.

6.6.2 E1 Strength

Much of the expected E1 EWSR ($83\pm^{35}_{20}$%) was identified in the range 9-40 MeV. The strength is divided into $1\hbar\omega$ and $3\hbar\omega$ [77--79] components. The high energy component is the compression mode, and its energy is related to K_A. The low energy component is mostly in the range $9\leq E_x\leq 20$ MeV, and the high energy component is mostly in the range $20\leq E_x\leq 36$ MeV [67]. The high and low peaks are fit well with Gaussians. The low energy component is at $15.07\pm^{.22}_{.19}$ MeV and contains 12% of the EWSR, and the high energy component is at $26.50\pm^{.44}_{.42}$ MeV and contains 45% of the EWSR. The results of the HF-RPA calculations for the E1 strength (broadened with a Lorentzian shape with ≈ 10 MeV width) are shown superimposed on the data in Figure 34. The calculated strength is in a broad peak with some strength at low excitation and indications of several components and structure at ≈27 and 32 MeV. The strength rises to a maximum near 30 MeV, roughly 4 MeV greater than the high peak from the experimental strength; and then tails past 40 MeV. In the low energy range ($9\leq E_x\leq 20$ MeV) there is a weak peak near the experimental one and also another one below it. The calculation and the

data do not agree, but the amount of strength predicted in the low energy range is nearly the same as the experimental value obtained from the Gaussian fit of the low peak. In the high energy range ($20 \leq E_x \leq 40$ MeV), the calculation for the peak position is greater than the experimental one by ≈2 MeV and predicts more strength than identified in the experimental data. In Figure 36, the centroids of the Gaussian fit to the low and high energy peaks and the strength in the low and high peaks for the isotopes from Ref. [67] and for ^{94}Mo is plotted vs A. For the Mo isotopes, the calculated positions of the low and high energy peaks tend to not be in agreement with the experimental position.

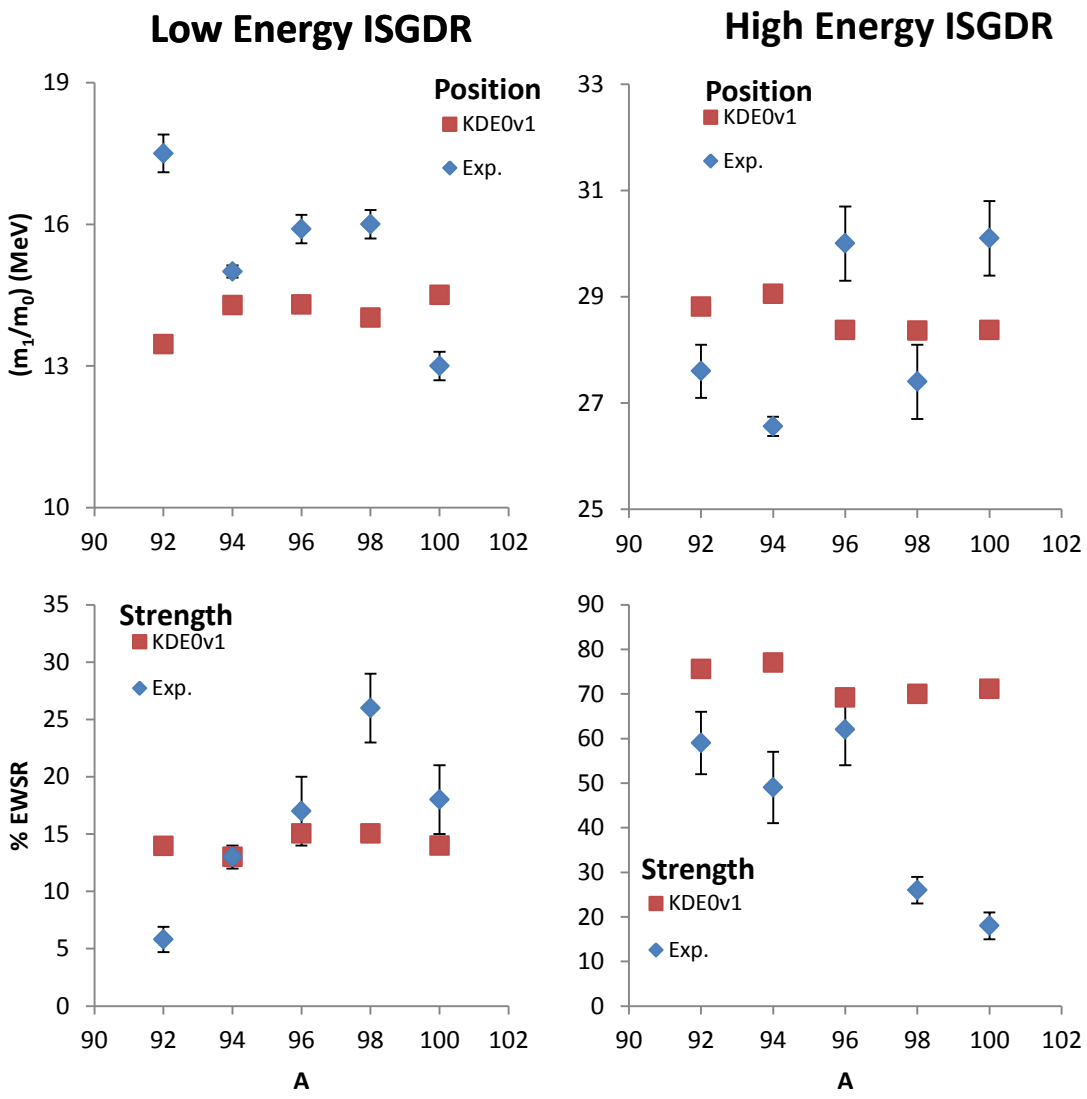

Figure 36. The centroids of the Gaussian fits to the low and high energy peaks in the ISGDR distributions for each of the Mo isotopes from Ref. [67] and ^{94}Mo from this work are plotted vs. A in the top panels. The strength in the low and high peak is plotted in the lower panels. The error bars indicate the uncertainty obtained using the errors shown in Table XX. The squares (red) show m_1/m_0 and the strength in the range $9 \leq E_x \leq 20$ MeV for the low peak and the range $20 \leq E_x \leq 36$ MeV for the high peak calculated with HF-RPA using the KDE0v1 interaction.

6.6.3 E2 Strength

The E2 peak is located at (m_1/m_0) 14.56±.09 MeV and 61±9% of the E2 EWSR was identified. The peak was fitted with a Gaussian and m_1/m_0, RMS width, and the Gaussian parameters are given in Table XXI. The Gaussian energy is approximately 1.5 MeV less than m_1/m_0 because of the inclusion of the apparently random strength at high excitation in the calculation of the energy moments. In the Mo isotopes studied in Ref. [67], the E2 strength distribution was slightly asymmetric on the low energy side. Moalem *et al.* [80] measured the GQR in ^{94}Mo with inelastic scattering of 110 MeV ^{3}He. Our result for %EWSR, energy, and width agree within the errors with their work. Figure 37 compares the Gaussian centroid energy of the GQR in the Mo isotopes obtained from the four experiments [67,80,81], the GQR measurement of ^{92}Mo with inelastic scattering of 120 MeV α particles by Duhamel *et al.* [81], and the m_1/m_0 obtained from the calculation with the KDE0v1 interaction. The calculated distribution shows a peak that is located at a higher energy by approximately 1 MeV, but it does show a similar amount of tailing on the high excitation side.

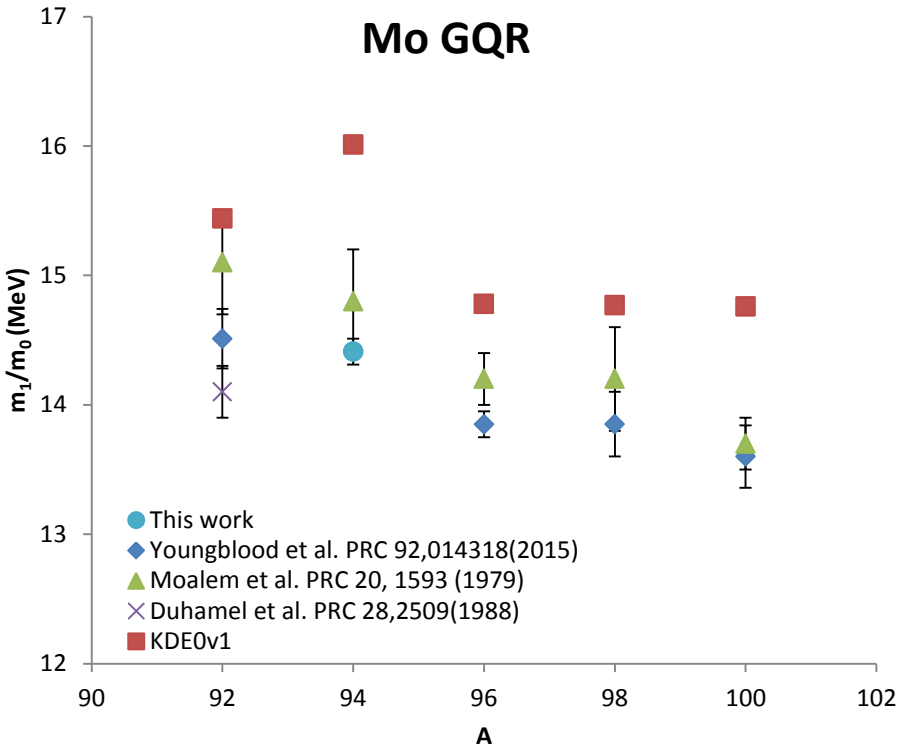

Figure 37. The m_1/m_0 energy of the E2 strength in each of the Mo isotopes from Ref. [67] (blue diamonds) and ^{94}Mo from this work (light blue circle) is plotted vs. A. The error bars indicate the uncertainty obtained using the errors shown in Table XX. Also shown with error bars are centroids reported in Ref. [80] (green triangles) and a measurement for ^{92}Mo [81] (purple X). The red squares show the centroid of the E2 strength obtained from HF-RPA calculations with the KDE0v1 interaction.

6.6.4 E3 Strength

In the Harmonic Oscillator Shell Model description of the Giant Resonances, the E3 resonance is split into a $1\hbar\omega$ low energy octupole (LEOR) containing 25% of the E3 EWSR and $3\hbar\omega$ high energy octupole (HEOR) containing 75% of the EWSR [83]. Coupling these modes with the octupole/octupole residual reaction gives an LEOR with

approximately 35% of the EWSR and HEOR with 65% EWSR [83]. The low-energy cutoff for the measured data lies in the middle of the higher region of the LEOR. The HF-RPA calculation with KDE0v1 interaction puts the LEOR at about 8 MeV, which is below the 9 MeV cutoff. The HEOR is predicted to be located at about 29 MeV. The experimental strength for the HEOR is in a broad peak centered at 24.6 MeV and contains 39% of the E3 EWSR. The calculated energy is 25.98 MeV. As was noted in Ref [67] , the calculated energies for the HEOR are sensitive to the effective mass. Using a larger effective mass would lower the predicted energy.

6.7 Summary

We have obtained distributions for isoscalar E0, E1, E2, and E3 strength in ^{94}Mo and compared these to spherical Hartree-Fock-RPA calculations using the KDE0v1 Skyrme type interaction. The E0 strength has a high energy tail similar to that in the A≠92 Mo nuclei which is not present in heavier nuclei. The source of this tail is not understood. The position of the high energy part of the isoscalar dipole does not agree with HF-RPA calculation. Position, strength and width of the E2 distributions agree within errors with those obtained by Moalem *et al.*, but are ≈1 MeV below those obtained with the HF-RPA calculations. The HEOR strength lies in a broad peak centered at 24.6 MeV, approximately 2 MeV below that obtained with the HF-RPA calculations.

7 CONCLUSIONS

The energies and strengths of the E0, E1, and E2 giant resonances have been measured in ^{44}Ca, ^{54}Fe, ^{64}Zn, ^{68}Zn, and ^{94}Mo. Additionally, the High Energy Octupole Resonance was measured in ^{94}Mo. The energies and strength distributions were compared with the results from HF-RPA calculations with the KDE0v1 interaction. The theoretical predictions agreed fairly well with the experimental results in a number of cases. However, in ^{94}Mo the theoretical predictions for E0-E3 did not agree with the experimental results. The predicted strength for E0 disagreed with the experimental strength in ^{68}Zn. In ^{44}Ca, ^{54}Fe, and ^{68}Zn the predicted strengths for E1 did not agree with the experimental ones. Theoretical and experimental E2 strengths were not in agreement in ^{44}Ca and ^{64}Zn. Microscopic calculations which include nuclear structure effects may be necessary to obtain the correct energies and strength distributions. Additionally, inlcuding microscopic transition dnesities in analyses of the experimental data may improve agreement between experiment and theory.

Kamerdzhiev, *et al.* [34] calculated double-differential cross sections at $\theta = 1.08°$ and 4.08° and strength distributions for the isoscalar E0-E3 resonances for ^{58}Ni and E0 and E2 for ^{40}Ca using a microscopic many-body theory which includes configurations beyond the 1p-1h level. The calculated E0 strength distribution for ^{58}Ni was in good agreement with the experimental data, but the calculated results for E1, E2, and E3 were not. For both nuclei, the calculated cross sections were able to reproduce the

experimental data reasonably well but with differences at low and high energies. The strength distributions calculated for ^{40}Ca were very successful at reproducing the E0 and E2 experimental data, though the predicted E2 strength is distributed more broadly than the experimental result.

There have been a number of attemtps to deduce K_τ, the symmetry term from the Leptodermous expansion (4), from calculation of K_A from the measured monopole energy in different nuclei within an isotopic chain, such as Cd (K_τ = -555±75 MeV) [84] and Sn (K_τ = -550±100 MeV) [85,86]. In Ref. [RW.ERROR - Unable to find reference:161], analysis of GMR data for Sn and Sm nuclei from 120 MeV inelastic α-scattering, along with data for ^{208}Pb and ^{24}Mg, resulted in a value for the symmetry term, K_τ = -320±184 MeV. Within an isotopic chain, the nuclear charge is fixed, and therefore the neutron-proton asymmetry (N-Z)/A increases when A increases. Although the surface and Coulomb contributions become a little less negative with increasing A, the negative increase of the symmetry contribution dominates. This is in general agreement with results from theory. The variations of K_τ from Skyrme interactions are K_τ = -400±100 MeV and effective relativistic mean field Lagrangians are K_τ = -620±180 MeV [87]. The result for the E0 energy in ^{44}Ca from this work was shown with the results for ^{40}Ca and ^{48}Ca and plotted against A in Figure 18, and this showed a monopole energy, and by extension K_A, that was rising instead of falling with A. This behavior is shown in Figure 38 with a calculation of K_A from Leptodermous expansion requiring K_{NM} = 200 MeV and K_τ = 582 MeV. This suggests that in the Ca isotopes it is unlikely that

calculations with common effective interactions will reproduce the mass dependence of the GMR energies without the addition of nuclear structure effects.

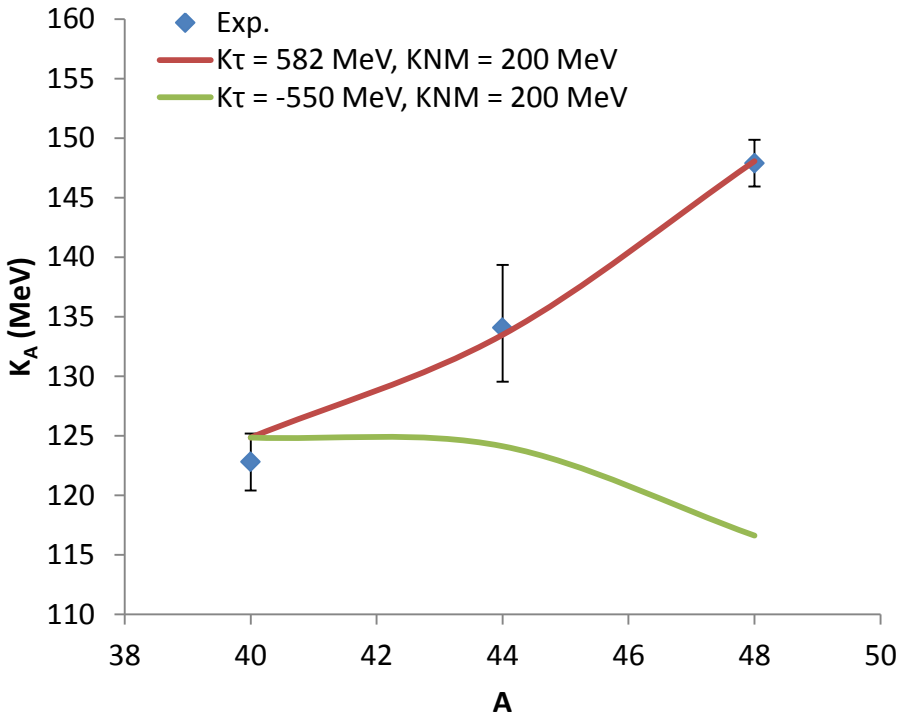

Figure 38. Values of K_A from the scaling energy $\sqrt{(m_3/m_1)}$ for the Ca isotopes are plotted against A. A fit to the data (red line) using the Leptodermous expansion with the parameters indicated is shown. The green line is shown as a reference and is also from the Leptodermous expansion but with a large, negative value for K_τ.

REFERENCES

[1] G. C. Baldwin and G. S. Klaiber, Phys. Rev. **71**, 3 (1947).

[2] M. Goldhaber and E. Teller, Phys. Rev. **74**, 1046 (1948).

[3] J. Speth, *Electric and Magnetic Giant Resonance in Nuclei* (World Scientific, 1991), 1.

[4] F. R. Buskirk, H. - D. Gräf, R. Pitthan, H. Theissen, O. Titze, and T. Walcher, Phys. Lett. B **42**, 194 (1972).

[5] M. B. Lewis and F. E. Bertrand, Nucl. Phys. A **196**, 337 (1972).

[6] J. M. Moss, C. M. Rozsa, J. D. Bronson, and D. H. Youngblood, Phys. Lett. B **53**, 51 (1974).

[7] J. M. Moss, C. M. Rozsa, D. H. Youngblood, J. D. Bronson, and A. D. Bacher, Phys. Rev. Lett. **34**, 748 (1975).

[8] D. H. Youngblood, J. M. Moss, C. M. Rozsa, J. D. Bronson, A. D. Bacher, and D. R. Brown, Phys. Rev. C **13**, 994 (1976).

[9] K. T. Knöpfle, G. J. Wagner, H. Breuer, M. Rogge, and C. Mayer-Böricke, Phys. Rev. Lett. **35**, 779 (1975).

[10] D. H. Youngblood, C. M. Rozsa, J. M. Moss, D. R. Brown, and J. D. Bronson, Phys. Rev. Lett. **39**, 1188 (1977).

[11] H. P. Morsch and P. Decowski, Phys. Lett. B **95**, 160 (1980).

[12] A. Bohr and B. R. Mottelson, *Nuclear Structure* (W.A. Benjamin, New York, 1975), Vol. 2.

[13] J. P. Blaizot, Phys. Rep. **64**, 171 (1980).

[14] J. Treiner, H. Krivine, O. Bohigas, and J. Martorell, Nucl. Phys. A **371**, 253 (1981).

[15] R. C. Nayak, J. M. Pearson, M. Farine, P. Gleissl, and M. Brack, Nucl. Phys. A **516**, 62 (1990).

[16] S. Shlomo and D. H. Youngblood, Phys. Rev. C **47**, 529 (1993).

[17] J. M. Pearson, Phys. Lett. B **271**, 12 (1991).

[18] V. M. Kolomietz and S. Shlomo, Phys. Rev. C **61**, 064302 (2000).

[19] G. Colo, N. Van Giai, J. Meyer, K. Bennaceur, and P. Bonche, Phys. Rev. C **70**, 024307 (2004).

[20] J. Kvasil, N. L. Iudice, C. Stoyanov, and P. Alexa, J. Phys. G. **29**, 753 (2003).

[21] D. Lacroix, S. Ayik, and P. Chomaz, Phys. Rev. C **63**, 064305 (2001).

[22] S. Yildirim, T. Gaitanos, M. Di Toro, and V. Greco, Phys. Rev. C **72**, 064317 (2005).

[23] D. Vretenar, T. Nikšić, and P. Ring, Phys. Rev. C **68**, 024310 (2003).

[24] S. Shlomo, V. M. Kolomietz, and G. Colò, Eur. Phys. J. A **30**, 23 (2006).

[25] S. Stringari, Phys. Lett. B **108**, 232 (1982).

[26] Krishichayan (private communication).

[27] Y. -W. Lui, D. H. Youngblood, H. L. Clark, Y. Tokimoto, and B. John, Phys. Rev. C **73**, 014314 (2006).

[28] D. H. Youngblood, Y. -W. Lui, J. Button, M. R. Anders, M. L. Gorelik, M. H. Urin, and S. Shlomo, Phys. Rev. C **88**, 021301 (2013).

[29] Y. -W. Lui, D. H. Youngblood, S. Shlomo, X. Chen, Y. Tokimoto, M. Anders, and J. Button, Phys. Rev. C **83**, 044327 (2011).

[30] M. R. Anders, S. Shlomo, T. Sil, D. H. Youngblood, and Y. -W. Lui, Phys. Rev. C **87**, 024303 (2013).

[31] Y. -W. Lui, D. H. Youngblood, Y. Tokimoto, H. L. Clark, and B. John, Phys. Rev. C **69**, 034611 (2004).

[32] Y. Tokimoto, Y. -W. Lui, H. L. Clark, B. John, X. Chen, and D. H. Youngblood, Phys. Rev. C **74**, 044308 (2006).

[33] S. Kamerdzhiev, J. Speth, and G. Tertychny, Eur. Phys. J. A **7**, 483 (2000).

[34] S. Kamerdzhiev, J. Speth, and G. Tertychny, Phys. Rep. **393**, 1 (2004).

[35] I. Hamamoto, H. Sagawa, and X. Z. Zhang, Phys. Rev. C **56**, 3121 (1997).

[36] D. H. Youngblood, Y. -W. Lui, and H. L. Clark, Phys. Rev. C **65**, 034302 (2002).

[37] D. H. Youngblood, Y. -W. Lui, and H. L. Clark, Phys. Rev. C **63**, 067301 (2001).

[38] D. H. Youngblood and J. D. Bronson, Nucl. Instrum. Methods A **361**, 37 (1995).

[39] D. M. Pringle, W. N. Catford, J. S. Winfield, D. G. Lewis, N. A. Jelley, K. W. Allen, and J. H. Coupland, Nucl. Instrum. Methods A **245**, 230 (1986).

[40] H. L. Clark, Y. -W. Lui, and D. H. Youngblood, Nucl. Phys. A **589**, 416 (1995).

[41] J. S. Winfield, D. M. Pringle, W. N. Catford, D. G. Lewis, N. A. Jelley, and K. W. Allen, Nucl. Instrum. Methods A **251**, 297 (1986).

[42] D. H. Youngblood, Y. -W. Lui, H. L. Clark, P. Oliver, and G. Simler, Nucl. Instrum. Methods A **361**, 539 (1995).

[43] D. H. Youngblood, Y. -W. Lui, and H. L. Clark, Phys. Rev. C **60**, 014304 (1999).

[44] O. Bunemann, T. E. Cranshaw, and J. A. Harvey, Can. J. Res. **27**, 191 (1949).

[45] O. Frisch, BR-46 (unpublished) (1949).

[46] G. Charpak and F. Sauli, Nucl. Instrum. Methods **162**, 405 (1979).

[47] J. B. Birks, Phys. Rev. **86** (1952).

[48] S. Kowalski and H. A. Enge, RAYTRACE, (unpublished).

[49] D. H. Youngblood, Y. W. Lui, and H. L. Clark, Phys. Rev. C **63**, 067307 (2001).

[50] D. H. Youngblood, Y. -W. Lui, and H. L. Clark, Phys. Rev. C **61**, 067307 (2000).

[51] K. F. Liu and N. Van Giai, Phys. Lett. B **65**, 23 (1976).

[52] S. Shlomo and G. Bertsch, Nucl. Phys. A **243**, 507 (1975).

[53] G. R. Satchler and D. T. Khoa, Phys. Rev. C **55**, 285 (1997).

[54] M. Rhoades-Brown, S. Pieper, and M. Macfarlane, *in Argonne National Laboratory Report* (Argonne National Laboratory, Argonne, 1978).

[55] L. D. Rickertsen, DOLFIN, unpublished, 1976.

[56] D. J. Horen, G. R. Satchler, S. A. Fayans, and E. L. Trykov, Nuclear Physics A **600**, 193 (1996).

[57] M. N. Harakeh and A. E. L. Dieperink, Phys. Rev. C **23**, 2329 (1981).

[58] H. Feshbach, *Theoretical Nuclear Physics* (Wiley, New York, 1992).

[59] M. E. Brandan and G. R. Satchler, Phys. Rep. **285**, 143 (1997).

[60] S. S. Dietrich and B. L. Berman, At. Data Nucl. Data Tables **38**, 199 (1988).

[61] D. H. Youngblood, Y. -W. Lui, and H. L. Clark, Phys. Rev. C **65**, 034302 (2002).

[62] K. van der Borg, M. N. Harakeh, and A. van der Woude, Nucl. Phys. A. **265**, 243 (1981).

[63] G. Fricke, C. Bernhardt, K. Heilig, L. A. Schaller, L. Schellenberg, E. B. Shera, and C. W. De Jager, At. Data Nucl. Data Tables **60**, 177 (1995).

[64] L. Ray, W. Rory Coker, and G. W. Hoffmann, Phys. Rev. C **18**, 2641 (1978).

[65] G. R. Satchler, Nucl. Phys. A **472**, 215 (1987).

[66] H. L. Clark, Y. -W. Lui, and D. H. Youngblood, Phys. Rev. C **57**, 2887 (1998).

[67] D. H. Youngblood, Y. -W. Lui, J. Button, G. Bonasera, and S. Shlomo, Phys. Rev. C **92**, 014318 (2015).

[68] P. - G. Reinhardt, Ann. Phys. (Leipzig) **1**, 632 (1992).

[69] T. Sil, S. Shlomo, B. Agrawal, and P. Reinhard, Phys. Rev. C **73**, 034316 (2006).

[70] S. Shlomo and A. Sanzhur, Phys. Rev. C **65**, 044310 (2002).

[71] B. K. Agrawal, S. Shlomo, and A. Sanzhur, Phys. Rev. C **67**, 034314 (2003).

[72] B. K. Agrawal, S. Shlomo, and V. K. Au, Phys. Rev. C **72**, 014310 (2005).

[73] A. Kolomiets, O. Pochivalov, and S. Shlomo, Phys. Rev. C **61**, 034312 (2000).

[74] D. H. Youngblood, H. L. Clark, and Y. -W. Lui, Phys. Rev. Lett. **82**, 691 (1999).

[75] T. v. Chossy and W. Stocker, Phys. Rev. C **56**, 2518 (1997).

[76] Y. -W. Lui, H. L. Clark, and D. H. Youngblood, Phys. Rev. C **61**, 067307 (2000).

[77] H. L. Clark, Y. -W. Lui, and D. H. Youngblood, Phys. Rev. C **63**, 031301(R) (2001).

[78] G. Colo, N. van Giai, P. F. Bortingon, and M. R. Quaglia, Phys. Lett. B **485**, 362 (2000).

[79] D. Vretenar, A. Wandelt, and P. Ring, Phys. Lett. B **487**, 334 (2000).

[80] A. Moalem, Y. Gaillard, A. Bemolle, M. Buenerd, J. Chauvin, G. Duhamel, D. Lebrun, P. Martin, G. Perrin, and P. De Saintignon, Phys. Rev. C **20**, 1593 (1979).

[81] G. Duhamel, M. Buenerd, P. De Saintignon, J. Chauvin, D. Lebrun, P. Martin, and G. Perrin, Phys. Rev. C **38**, 2509 (1988).

[82] Krishichayan, Y. -W. Lui, J. Button, D. H. Youngblood, G. Bonasera, and S. Shlomo, Phys. Rev. C **92**, 044323 (2015).

[83] J. M. Moss, D. H. Youngblood, C. M. Rozsa, D. R. Brown, and J. D. Bronson, Phys. Rev. Lett. **37**, 816 (1976).

[84] D. Patel, U. Garg, M. Fujiwara, H. Akimune, G. Berg, M. Harakeh, M. Itoh, T. Kawabata, K. Kawase, and B. Nayak, Phys. Lett. B **718**, 447 (2012).

[85] T. Li, U. Garg, Y. Liu, R. Marks, B. Nayak, P. M. Rao, M. Fujiwara, H. Hashimoto, K. Kawase, and K. Nakanishi, Phys. Rev. Lett. **99**, 162503 (2007).

[86] T. Li, U. Garg, Y. Liu, R. Marks, B. Nayak, P. M. Rao, M. Fujiwara, H. Hashimoto, K. Nakanishi, and S. Okumura, Phys. Rev. C **81**, 034309 (2010).

[87] G. Colò, U. Garg, and H. Sagawa, Eur. Phys. J. A **50**, 1 (2014).